The Chiral and $U(1)_A$ Symmetries of the QCD Phase Transition using Chiral Lattice Fermions

Zhongjie Lin

Submitted in partial fulfillment of the

requirements for the degree of

Doctor of Philosophy

in the Graduate School of Arts and Sciences

COLUMBIA UNIVERSITY

2014

Abstract

The Chiral and $U(1)_A$ Symmetries of the QCD Phase Transition using Chiral Lattice Fermions

Zhongjie Lin

With regard to the nature of the finite-temperature QCD phase transition and the fate of the chiral and anomalous axial symmetries associated with it, we present in this thesis two parallel sets of investigations into the QCD phase transition region between 139 and 195 MeV. Both studies adopt the Iwasaki gauge action augmented with the dislocation suppression determinant ratio with 2+1 flavors of chiral fermions. This choice of lattice action accurately reproduces the $SU(2)_L \times SU(2)_R$ and $U(1)_A$ symmtries of the continuum.

The first study simulates QCD thermodynamics on a line of constant physics that represents 200 MeV pions and physical kaons using domain wall fermions (DWF) at three space-time volumes: $16^3 \times 8$, $24^3 \times 8$, and $32^3 \times 8$, where the largest volume varies in linear size between 5.6 fm (at $T = 139$ MeV) and 4.0 fm (at $T = 195$ MeV). The chiral condensates, connected and disconnected susceptibilities and the Dirac eigenvalue spectrum are reported and compared between different volumes as well as with the staggered results. We find a pseudo-critical temperature, T_c, of approximately 165 MeV and strong finite volume dependence below T_c. Clear evidence is seen for $U(1)_A$ symmetry breaking above T_c which is quantitatively explained by the measured density of near-zero modes in accordance with the dilute instanton gas approximation.

The second study targets on a line of constant physics with pions of physical mass, which is the very first study using a chiral lattice fermion formulaation. We continue to use the basic setup from the $m_\pi \approx 200$ MeV simulations, except that we use a generalized form of domain wall fermions, known as the Möbius fermions, to further reduce the residual chiral

symmetry breaking present in the domain wall formulation with finite extent in the fifth dimension. Preliminary results including the chiral condensates and the susceptibilities are reported for two space-time volumes of $32^3 \times 8$ and $64^3 \times 8$. We observe a dramatic increase in the disconnected susceptibilities and a shift in the pseudo-critical temperature from 165 MeV to about 154 MeV, when the pion mass is decreased from 200 MeV to 135 MeV.

Contents

List of Tables

List of Figures

ACKNOWLEDGMENTS

Top of all, I would like to thank my advisor, Prof. Norman Christ, who has constantly guided and supported me in study, in research, and also in life during my Ph.D years. His kindness and enthusiasm in the weekly discussion as well as in many other occassions have inspired and benefited me in many ways. I am also deeply in debt to Prof. Robert Mawhinney for many insightful suggestions. Furthermore, both Prof. Christ and Prof. Mawhinney have provided tremendous convenience in commuting between Columbia and BNL so that I am able to join the monthly RBC meeting which is full of interesting topics. I would like to thank every member in the RBC-UKQCD collaboration. Although finite temperature physics is not the central topic in the collaboration, I still received much help from their orignial ideas.

I am also very grateful for the help and discussions from Prof. Frithjof Karsch and members from HotQCD: Michael Cheng, Heng-Tong Ding, Prasad Hegde, Swagato Mukherjee, Dwight Renfrew, Chris Schroeder, and many others.

Ph.D students and postdocs at Columbia have created a harmonious and inspiring environment for the physics discussion which I have benefited a lot. I really enjoy working with Xu Feng, Chris Kelly, Luchang Jin, Xiao-Yong Jin, Qi Liu, Greg McGlynn, Hantao Yin, Jianglei Yu, Daiqian Zhang, and many other colleagues at Columbia.

Finally, I sincerely appreciate years of support and encouragements from my family and friends.

Chapter 1

Introduction

1.1 Standard Model

The Standard Model of particle physics [6] represents humans' current best understanding for the fundamental building blocks of matter and their interactions. Finally established in 1970s, the Standard Model is the consummation of a series of continuing endeavors ever since the beginning of the twentieth century, when the study of subatomic physics started to flourish with both theoretical and experimental approaches.

The Standard Model has successfully predicted and withstood numerous experimental tests: the discovery of W/Z bosons [7, 8], the discovery of the top quark [9, 10], and the discovery of the Higgs boson, a long missing piece for the Standard Model [11, 12], just to name a few.

The Standard Model incorporates three of the four most fundamental forces in nature (gravitational interaction excluded) into a $SU(3) \times SU(2) \times U(1)$ gauge theory. The electroweak $SU(2) \times U(1)$ sector unifies the weak interaction and the electromagnetic interaction, whereas the remaining $SU(3)$ sector describes the strong interaction.

The abelian $U(1)$ Quantum Electrodynamics (QED) was formulated as a first success of

the application of quantum field theory in the 1940s by Feynman, Schwinger and Tomonaga. Later in the 1950's, an enormous population of new subatomic particles was discovered with the assistance of a new generation of particle accelerators. Weak and strong interactions were first introduced in the 1950's [13] to distinguish a class of elementary particles known as "leptons", which only participate in the weak interactions usually associated with particle decays. The other class of particles, the "hadrons", participate in both types of interactions.

In the following decade, the weak interaction was first successfully decoded by Glashow, Salam, and Weinberg [14, 15, 16] and unified with the electromagnetic interaction via spontaneous symmetry breaking and the Higgs mechanism. For the understanding of the remaining strong force, the first crucial breakthrough came when the "eight-fold-way" was proposed and developed by Gell-Mann and independently by Zweig [17, 18, 19, 20] in a effort to categorize the seemingly erratic "particle zoo". The "eight-fold-way" introduced a new intrinsic degree of freedom within the hadrons, a new type of particle named "quarks" by Gell-Mann. The later discovery of the Ω^- [21] provided strong evidence in favor of the existence of quarks. However, the quark model also faced several challenges, for instance, the futile search for an isolated free quark and the seemingly violation of Pauli exclusion principle for some of the baryons. It was not until 1973, that the quark model finally triumphed, when Polizer, Gross and Wilczek independently studied on $SU(3)$ non-abelian gauge theory of the strong interaction and proved that it is asymptotically free [22, 23]. A unit of any one of the three, so-called color charges is assigned to each individual quark. Therefore the gauge theory that describes the strong interaction is named Quantum Chromodynamics (QCD).

In the Standard Model, QCD consists of three generations of quarks that come in pairs: "up" and "down", "strange" and "charm", "bottom" and "top", with eight gluons which serve as the mediators for the strong interactions. QCD displays at least two intriguing phases. At long distances or low energy, the quarks are strongly coupled and they are confined within the hadrons. At short distances or high temperature, quarks become unbound and only

weakly interacting, which has been observed in the experiments [24]. Between these two phases, QCD is expected to undergo a phase transition.

The QCD phase transition, separating the low-temperature phase in which the (approximate) $SU(2)_L \times SU(2)_R$ symmetry of QCD with two light flavors is broken by the vacuum and the high-temperature phase in which this symmetry is restored, has been the subject of active experimental and theoretical study for more than 30 years. The present expectation is that this is a second-order transition belonging to the $O(4)$ universality class when the up and down quark masses are zero [25] and a possibly rapid cross-over for the non-zero, physical light quark mass.

While in the asymptotically free phase, QCD can be studied using perturbation theory, currently there are no known analytical solutions for the hadronic non-perturbative regime. Fortunately, constructed from the Feynman path integral approach, the lattice regularization for QCD introduced by Wilson in 1974 [26] provides a brand new tool to tackle non-perturbative QCD numerically with assistance from computers. After 30 years of development and evolution of the discretization schemes for both the bosonic and fermionic fields as well as significant improvements in the algorithms and numerical methods, lattice QCD now stands as the standard *ab initio* approach to study many phenomena associated with the strong interaction.

Ever since its inception, the lattice formulation of QCD has been applied to investigate the QCD phase transition. For instance, a phase transition was observed with pure $SU(2)$ gauge theory on the lattice [27, 28]. In recent years, the QCD phase transition has been extensively studied using the staggered formulation [29, 30] of lattice fermions, *c.f.* [31, 5]. However, calculations employing chiral fermions are more difficult and less frequent [32, 33, 34, 35, 36]. In contrast to the staggered formulation in which finite lattice spacing effects explicitly break the anomalous $U(1)_A$ symmetry and all but one of the six $SU(2)_L \times SU(2)_R$ symmetry directions, variants of the chiral fermion formulation accurately reproduce these symmetries.

At low temperatures one finds three degenerate light pions and the $U(1)_A$ current obeys an anomalous conservation law identical to that in the continuum up to small, controlled residual chiral symmetry breaking effects.

In this work, we study the temperature region 139 MeV $\leq T \leq$ 195 MeV using chiral, domain wall fermions (DWF) [37, 38] and Möbius domain wall fermions (MDWF) [39, 40] with a lattice volume having a fixed time extent of 8 in lattice units and a variety of spatial volume: 16^3, 24^3, 32^3 or 64^3. The temperature is varied by varying the inverse gauge coupling β between 1.633 and 1.829 using the Iwasaki gauge action combined with a dislocation suppressing determinant ratio (DSDR) [41, 42, 43, 44] to reduce the effects of residual chiral symmetry breaking at these relatively strong couplings. The strange quark mass is set to its physical value while the light quark mass is tuned carefully so that the pion mass is held fixed at either a heavier-than-physical 200 MeV value or right around the physical 135 MeV value. The latter is the first investigation of QCD thermodynamics with chiral lattice fermions at physical value for the light quark mass.

1.2 Organization of Thesis

This thesis summarizes works published in Refs. [35, 45, 46], for which I am one of the major contributors. Many discussions presented in this report are excerpted from these references and most of the citations to them are implicit.

This thesis is organized as follows. In Chapter 2, we describe the QCD lagrangian in the continuum and then introduce several proposals to discretize the gauge fields and the fermion fields. We focus on the domain wall fermion formulation, which is used extensively in our finite-temperature studies, and discuss several methods that can further suppress the residual chiral symmetry breaking, including the Möbius fermion formulation and the dislocation suppression determinant ratio and *etc.*.

In Chapter 3, we give a brief introduction to the exploration for the QCD deconfinement

phase transition and the chiral phase transition in the heavy-ion collision experiments as well as in theory.

In Chapter 4, we describe how we determine the line of constant physics and the corresponding lattice parameters that are used in our simulations. The residual mass plays an important role in the setup procedure, therefore we present a detailed numerical study for the residual mass with both domain wall fermions and the Möbius fermions.

Chapter 5 reports the results from lattices with a variety of volumes and quark masses for the chiral observables, *e.g.* the chiral condensates, connected and disconnected susceptibilities, as probes of the symmetries associated with QCD phase transition.

Chapter 6 is a self-contained discussion for the eigenvalue spectrum of the DWF Dirac operator. The low-lying part of the spectrum provides an important alternative perspective for resolving the fate of $SU(2)_L \times SU(2)_R$ and $U(1)_A$ symmetries associated with the QCD phase transition. Results from $16^3 \times 8$ and $32^3 \times 8$ lattice space-time volume with 200 MeV pions are presented and compared.

Chapter 7 concludes the thesis and gives a brief future outlook.

Finally, Appendix A gives a detailed description for the multiple streams within each ensemble.

Chapter 2

Quantum Chromodynamics and its Lattice Formulations

In this chapter, we start with a brief introduction to the action of Quantum Chromodynamics in the continuum. It is then followed by a discussion of how the QCD action shall be constructed appropriately on a lattice. Several discretization schemes of both the gauge and the fermion fields are presented. In the later part of this chapter, we discuss several methods that are utilized to improve the residual chiral symmetry breaking of the domain wall fermion formulation.

It should be noted that when we start to describe the QCD theory on a lattice, it is implicitly assumed that we adopt the Euclidean space instead of the Minkowski space as one usually do for the continuum field theory. These two can be connected by a Wick rotation, the details of which can be found in many field theory textbooks, *e.g.* [47].

2.1 Continuum QCD

Quantum Chromodynamics (QCD) is the current best description for strong interactions. Formally speaking, it is a non-abelian $SU(3)$ gauge theory, consisting of six flavors of fermions

(quarks) which carry color charges and eight types of bosons (gluons) which mediate the strong interaction. The QCD Lagrangian is given by,

$$\mathcal{L}_{\mathrm{QCD}} = \mathcal{L}_F + \mathcal{L}_G \tag{2.1}$$

$$\mathcal{L}_F(x) = \sum_{f\in u,d,s,c,b,t} \bar{q}_f(x)\left(\not{D} - m_f\right) q_f(x) \tag{2.2}$$

$$\mathcal{L}_G(x) = -\frac{1}{4} F^a_{\mu\nu}(x) F^{a,\mu\nu}(x). \tag{2.3}$$

Here $q_f(x)$ and $A^a_\mu(x)$ are quark fields and gluon fields respectively. The covariant derivative $\not{D}$ and the field strength $F^a_{\mu\nu}(x)$ are defined as:

$$\not{D} = i\gamma^\mu\left(\partial_\mu - g A^a_\mu \frac{\lambda^a}{2}\right) \tag{2.4}$$

$$F^a_{\mu\nu} = \partial_\mu A^a_\nu(x) - \partial_\nu A^a_\mu(x) - g f^{abc} A^b_\mu(x) A^c_\nu(x). \tag{2.5}$$

And λ^a $(a = 1, 2, \ldots, 8)$ are the generators of $SU(3)$ symmetry group, which are also known as the Gell-Mann Matrices. They satisfy the following relations

$$\mathrm{Tr}(\lambda_a \lambda_b) = 2\delta_{ab} \tag{2.6}$$

$$[\lambda_a, \lambda_b] = 2i f_{abc} \lambda_c. \tag{2.7}$$

f^{abc} that appears both in (2.5) and (2.6) are the structure constants for $SU(3)$.

2.2 Gauge Actions on a Lattice

As pointed out in the previous introductory section, QCD is characterized by a local non-abelian symmetry group $SU(3)$. Recall that in the continuum theory, in order to find the action of the gauge fields, we first start with a free fermion action and then introduce a local gauge transformation to the fermionic fields:

$$\begin{cases} \psi(x) \longrightarrow e^{i\theta^b(x)\lambda^b}\psi(x) \\ \overline{\psi}(x) \longrightarrow \overline{\psi}(x) e^{-i\theta^b(x)\lambda^b} \end{cases}.^{1} \tag{2.8}$$

[1] To avoid potential confusion with lattice spacing, we avoid to use a as indices for the gauge fields and *etc.* in the following introduction.

Meanwhile, the resulting gauge fields should transform covariantly as,

$$A^a_\mu \longrightarrow A^a_\mu - \frac{1}{g}\partial_\mu \theta^b - f^{bcd}\theta^c A^d_\mu. \tag{2.9}$$

Then one can prove that the fermionic part of the QCD action 2.2 is manifestly invariant under such gauge transformations.

However, when we start to discretize the theory on the lattice, we have to replace the partial derivatives with the finite differences. Hence rigorously speaking, the lattice action inevitably becomes *non-local*. Therefore, to ensure a manifest gauge invariance for the lattice action, we should at least find a way to make the following two-point function gauge invariant,

$$\overline{\psi}(x)\psi(x+\hat{\mu}a) \longrightarrow \overline{\psi}(x)e^{-i\theta^b(x)t^b}e^{i\theta^b(x+\hat{\mu}a)t^b}\psi(x+\hat{\mu}a), \tag{2.10}$$

where $\hat{\mu} = 1, 2, 3, 4$ are unit vectors that point in one of the four possible directions on the lattice. Fortunately, the *Schwinger line integral* comes to the rescue,

$$U(x,y) = e^{ig\int_x^y \mathrm{d}z_\mu A^b_\mu(z)t^b}. \tag{2.11}$$

It compensates for the difference between the transformation factors associated with two neighboring sites. It can be readily proved that the sandwiched term $\overline{\psi}(x)U(x, x+\hat{\mu}a)\psi(x+\hat{\mu}a)$ is gauge invariant with transformation (2.8) and (2.9). When lattice spacing a is small, the line integral reduces to

$$U_\mu(x) \equiv U(x, x+\hat{\mu}a) \equiv \exp\left(igaA^b_\mu(x)t^b\right), \tag{2.12}$$

Now the discretized gauge fields are represented by $SU(3)$ matrices that reside on the links between the adjacent lattice sites.

With this discretization formulation (2.12), any path ordered product of gauge links that compose a closed loop on the lattice is manifestly gauge-invariant. The simplest example of such loop, the elementary 1×1 square, is referred as the *plaquette*,

$$P_{\mu\nu}(x) = U_\mu(x)U_\nu(x+\hat{\mu}a)U^\dagger_\mu(x+\hat{\nu}a)U^\dagger_\nu(x), \qquad \mu \neq \nu. \tag{2.13}$$

And the renowned Wilson gauge action [26] is expressed in terms of these plaquettes:

$$S_G^{\text{Wilson}} = \frac{\beta}{3} \sum_{x;\mu\neq\nu} \text{ReTr}\left(\mathbf{1} - P_{\mu\nu}(x)\right), \qquad \beta = \frac{6}{g^2}. \tag{2.14}$$

It can be shown that in the continuum limit, the Wilson gauge action reproduces the kinetic term of the gauge fields of the QCD action and the leading discretization errors of the Wilson gauge action are of order $\mathcal{O}(a^2)$.

It has been found in several studies [48, 49] that lattice calculations with the Wilson gauge action deviate appreciably from the continuum theory. The Wilson action is by no means the unique discretization scheme for the QCD gauge action. In fact, any gauge-invariant path ordered loop can be added to the action, so long as it converges to the correct continuum action when the limit $a \to 0$ is taken. A possible choice is the next simplest loop, a planar 1×2 rectangular term $R_{\mu\nu}(x)$,

$$R_{\mu\nu}(x) = U_\mu(x)U_\mu(x+\hat{\mu}a)U_\nu(x+2\hat{\mu}a)U_\mu^\dagger(x+\hat{\mu}a+\hat{\nu}a)U_\mu^\dagger(x+\hat{\nu}a)U_\nu^\dagger(x), \qquad \mu \neq \nu. \tag{2.15}$$

Then the gauge action becomes:

$$S_G^{\text{Improved}} = \frac{\beta}{3} \sum_{x;\mu\neq\nu} \text{ReTr}\left(\mathbf{1} - c_0 P_{\mu\nu}(x) - c_1 R_{\mu\nu}(x)\right). \tag{2.16}$$

The constraint that $c_0 + 8c_1 = 1$ should be imposed to ensure a correct continuum limit. There are two popular choices of the pair of c_1 and c_2, Iwasaki ($c_1 = -0.331$)[50] and DBW2 ($c_1 = -1.4069$)[51] actions. The Iwasaki gauge action, which has been proved to display better chiral behavior[52] when coupled with the domain wall fermion action, is adopted through all of our studies on QCD thermodynamics.

2.3 Fermion Actions on a Lattice

2.3.1 Failure of Naive Lattice Fermions

As mentioned in previous section, the most straightforward method to discretize the fermionic part of the QCD action in Euclidean space is simply to replace the derivatives by

finite differences

$$\partial_\mu \longrightarrow \frac{1}{2a}\left(\delta_{x+\hat{\mu}a,x'} - \delta_{x-\hat{\mu}a,x'}\right). \tag{2.17}$$

Such a symmetric difference guarantees a Hermitian Hamiltonian. The resulting discretized action then takes the following form

$$S_F^{\text{Naive}} = \sum_{x,y} \overline{\psi}(x)\left(\frac{1}{2}\sum_\mu \left(\gamma_\mu \delta_{x+\hat{\mu}a,y} - \gamma_\mu \delta_{x-\hat{\mu}a,y}\right) + m\delta_{x,y}\right)\psi(y). \tag{2.18}$$

If we use a hypercube of extent N in all direction and calculate the fermion propagator

$$\left\langle \psi(x)\overline{\psi}(y)\right\rangle = \frac{1}{Z}\int \left(\prod_x d\psi(x) d\overline{\psi}(x)\right)\psi(x)\overline{\psi}(y)e^{-S_F^{\text{Naive}}} \tag{2.19}$$

in the momentum space, it becomes a integral within the first Brillouin zone:

$$\left\langle \psi(x)\overline{\psi}(y)\right\rangle = \lim_{a\to 0}\int_B \frac{d^4p}{(2\pi)^4}\frac{-i\frac{1}{a}\sum_\mu \gamma_\mu \sin\left(p_\mu a\right) + m}{\frac{1}{a^2}\sum_\mu \sin^2\left(p_\mu a\right) + m^2}e^{ip(x-y)}, \tag{2.20}$$

where the continuum limit is taken as a approaches 0 while N goes to infinity and the total extent in each direction is kept fixed. This solution, however, arrives at an incorrect continuum limit, which is known as the notorious *fermion doubling* problem.

When the continuum limit is taken, the propagator in (2.20) receives a "proper" contribution from the origin ($p_\mu \approx 0$), which equals the correct continuum theory result. However, it also receives "improper" contributions from the corners of the Brillouin zone ($p_\mu \approx \pm\pi/a$). Thus in total, this naive fermion action will produce 16 degenerate fermions instead of the one that we are looking for.

Unfortunately, the fermion doubling problem cannot be cured in a lattice theory that respects the usual hermiticity, locality, translational invariance as well as the chiral symmetry with vanishing quark masses at the same time [53]. Despite this, many efforts and talents have been devoted to remedy the fermion doubling problem. And in the following two subsections, we are going to introduce some of these ingenious methods which are closely related to our QCD finite temperature studies.

2.3.2 The Wilson Fermions

Bearing in mind that the continuum limit is achieved in the limit $a \to 0$, one would recognize that actions that only differ by terms which will vanish in the continuum limit will eventually converge to the same continuum behavior. With this guideline, Wilson [54] introduced a massive second derivative term into the naive fermion action

$$S_F^{\text{Wilson}} \equiv \sum_{xy} \overline{\psi}(x) D_W(x,y) \psi(y) \equiv S_F^{\text{Naive}} - \frac{1}{2} \sum_x \overline{\psi}(x) \,\Box\, \psi(x) \tag{2.21}$$

where $\Box$ is the four-dimensional Laplacean operator and $D_W(x,y)$, the *Wilson Dirac operator* is given by

$$D_W(x,y) = (4+m)\delta_{x,y} - \frac{1}{2} \sum_\mu \left((1-\gamma_\mu)\delta_{x+\hat{\mu}a,y} + (1+\gamma_\mu)\delta_{x-\hat{\mu}a,y} \right). \tag{2.22}$$

Thus the free fermion propagator in the momentum space can be computed as

$$\left\langle \psi(x)\overline{\psi}(y) \right\rangle = \lim_{a\to 0} \int_B \frac{d^4p}{(2\pi)^4} \frac{-i\frac{1}{a}\sum_\mu \gamma_\mu \sin(p_\mu a) + m(p)}{\frac{1}{a^2}\sum_\mu \sin^2(p_\mu a) + m(p)^2} e^{ip(x-y)}, \tag{2.23}$$

where

$$m(p) = m + \frac{2}{a} \sum_\mu \sin^2 \frac{p_\mu a}{2}. \tag{2.24}$$

For any fixed p_μ, $m(p)$ reduces to m when $a \to 0$. In other words, the effects of the extra mass term in the Wilson fermion action vanish in the continuum limit as desired. On the other hand, at the corners of the first Brillouin zone where $p_\mu \approx \pi/a$, the $m(p)$ term diverges in the continuum limit as

$$\frac{2}{a} \sum_\mu \sin^2 \frac{p_\mu a}{2} \propto \frac{1}{a}. \tag{2.25}$$

Furthermore, the $m(p)$ term still contributes the necessary correct piece around the origin $p_\mu \approx 0$. Therefore, the Wilson fermion formalism successfully eliminates the 15 extra doublers in the continuum limit.

However, the benefit of absence of doublers comes with a significant expense, the explicit breaking of chiral symmetry. This can be easily verified once we take a look at the interacting

Wilson Dirac operator by coupling the free fermion fields with the lattice gauge links in a straightforward manner,

$$D_W(x,y;U) = (4+m)\delta_{x,y} - \frac{1}{2}\sum_\mu \left((1-\gamma_\mu)U_\mu(x)\delta_{x+\hat{\mu},y} + (1+\gamma_\mu)U_\mu^\dagger(x-\hat{\mu})\delta_{x-\hat{\mu},y}\right).^2 \quad (2.26)$$

Under the axial gauge transformation

$$\begin{cases} \psi(x) & \longrightarrow & e^{i\gamma_5\theta^b(x)t^b}\psi(x) \\ \overline{\psi}(x) & \longrightarrow & \overline{\psi}(x)e^{i\gamma_5\theta^b(x)t^b} \end{cases}, \quad (2.27)$$

the Wilson mass term fails to preserve the chiral symmetry since it commutes rather than anti-commutes with γ_5. The order of the chiral symmetry breaking due to the Wilson mass term is in general $\mathcal{O}(1)$.

We can investigate the effects of this chiral symmetry breaking by looking at the Ward identity associated with the axial current using the Wilson fermion action. Varying the fermion path integral with the infinitesimal axial gauge transformation (2.27), we would obtain the axial current and its divergence in the following form:

$$A_\mu(x) = \frac{1}{2}\overline{\psi}(x)\gamma_\mu\gamma_5 t^b U_\mu(x)\psi(x+\hat{\mu}) + \frac{1}{2}\overline{\psi}(x+\hat{\mu})\gamma_\mu\gamma_5 t^b U_\mu^\dagger(x)\psi(x) \quad (2.28)$$

$$\begin{aligned}\Delta_\mu A_\mu(x) = {} & 2(4+m)\overline{\psi}(x)\gamma_5 t^a\psi(x) \\ & -\frac{1}{2}\sum_\mu \overline{\psi}(x)\gamma_5 t^b U_\mu(x)\psi(x+\hat{\mu}) - \frac{1}{2}\sum_\mu \overline{\psi}(x)\gamma_5 t^b U_\mu^\dagger(x-\hat{\mu})\psi(x-\hat{\mu}) \\ & -\frac{1}{2}\sum_\mu \overline{\psi}(x-\hat{\mu})\gamma_5 t^b U_\mu(x-\hat{\mu})\psi(x) - \frac{1}{2}\sum_\mu \overline{\psi}(x+\hat{\mu})\gamma_5 t^b U_\mu^\dagger(x)\psi(x),\end{aligned} \quad (2.29)$$

where the lattice version of the divergence operator is defined as the left-associated finite differences $\Delta_\mu f(x) = f(x) - f(x-\hat{\mu})$.

As can be read from Eqs. (2.29), apart from the counterpart to the continuum term $2m\overline{\psi}\gamma_5 t^a\psi$, some $\mathcal{O}(1)$ terms emerge as a consequence of the Wilson fermion formalism. One way to handle the effects of this term is to simply absorb them into the mass term. This yields $\mathcal{O}(1)$ additive renormalization of the fermion mass. Thus in practical calculations, the

[2] From now on, we will suppress the lattice spacing a in the expressions unless necessary.

input quark mass term must be fine-tuned so that the physical quark mass is in line with the designated value.

Wilson fermion formalism is very straightforward in both the physical sense and in real implementation. However, with Wilson fermions, one has to take the continuum limit simultaneously with the chiral limit where extreme care needs to be taken and interpretation of the results of finite lattice spacing can be be quite difficult. Thus the explicit breaking of the chiral symmetry makes the Wilson fermion formalism much less attractive when we are studying questions such as the spontaneous chiral symmetry breaking, which is at the heart of the study on the QCD thermodynamics.

2.3.3 The Domain Wall Fermions

To cure the significant explicit breaking of the chiral symmetry while still taking advantage of its simple physical interpretation, Kaplan proposed a new variant of the Wilson lattice fermion discretization scheme which was later referred as domain wall fermions (DWF) [37, 38].

The DWF formulation successfully solves the fermion doubling problem while keeping chiral symmetry breaking at a controllable minimum level. This is accomplished by introducing an auxiliary fifth dimension to the action, which is commonly referred as the s-direction to be distinguished to the space-time directions x, y, z and t. The DWF action assumes the following form

$$S_F^{\mathrm{DWF}} = \sum_{x,s;x',s'} \overline{\psi}(x,s) D_{\mathrm{DWF}}(x,s;x',s') \psi(x',s'), \tag{2.30}$$

where the domain wall Dirac operator is defined as $(0 \le s, s' \le L_s - 1)$:

$$D_{\mathrm{DWF}}(x,s;x',s') = (\delta_{x,x'} + D_W(x,x'))\delta_{s,s'} - m(s)P_R\delta_{s,s'+1} - m(s+1)P_L\delta_{s,s'-1}. \tag{2.31}$$

Here $D_W(x,x')$ is the usual Wilson Dirac operator (2.22) with a special mass M_5, which is defined as the *domain wall height*. $P_L = \frac{1}{2}(1-\gamma_5)$ and $P_R = \frac{1}{2}(1+\gamma_5)$ are projection operators.

And $m(s)$ is defined as follows

$$m(s) = \begin{cases} 1 & s = 1, 2, \cdots, L_s - 1 \\ -m_f & s = 0 \end{cases}, \tag{2.32}$$

where L_s is the extent of the fifth dimension.

As one can observe from the definitions above, DWF can be regarded as a stack of L_s copies of Wilson fermions, which share the same gauge fields. And the s-direction is coupled by a non-trivial mass matrix $m(s)$. Therefore, superficially DWF still has L_s doublers. However, $L_s - 1$ flavors of these fermions are extremely-heavy (at the order of the UV cutoff) and can be cancelled with a proper Pauli-Villars subtraction, which corresponds to an additional term in the action [55]

$$S_{\mathrm{PV}} = \sum_{x,s;x's'} \phi^\dagger(x,s) D_{\mathrm{DWF}}[m_f = 1](x,s;x',s')\phi(x',s'). \tag{2.33}$$

The surviving physical fermions are represented by a pair of coupled left- and right-handed Weyl fermions localized on the two ends (walls) of the s-direction. These couple strongly to the four-dimensional quark fields q and $\bar{q}$ constructed from the five-dimensional (5-d) DWF fields ψ and $\overline{\psi}$:

$$q(x) = P_L\psi(x,0) + P_R\psi(x,L_s-1) \tag{2.34}$$

$$\overline{q}(x) = \overline{\psi}(x,L_s-1)P_L + \overline{\psi}(x,0)P_R. \tag{2.35}$$

Starting with the following 5-d current associated with the global $U(3)$ flavor transformation, we can investigate the conservation of the physical 4-d currents for DWF [38]:

$$j^b_\mu(x,s) = \overline{\psi}(x+\hat{\mu},s)P_R U^\dagger_\mu(x) t^b \psi(x,s) - \overline{\psi}(x,s)P_L U_\mu(x) t^b \psi(x+\hat{\mu},s). \tag{2.36}$$

The definition of the resulting conserved 4-d vector current is unique:

$$\mathcal{V}^b_\mu(x) = \sum_{s=0}^{L_s-1} j^b_\mu(x,s), \quad \Delta_\mu \mathcal{V}^b_\mu(x) = 0. \tag{2.37}$$

The 4-d axial current tolerates a certain arbitrariness, as long as the transformation assigns opposite signs to left- and right-handed Weyl fermions. We would like to choose one of the symmetric definitions given as:

$$\mathcal{A}_\mu^b(x) = \sum_{s=0}^{L_s-1} \mathrm{sgn}\left(s - \frac{L_s-1}{2}\right) j_\mu^b(x,s). \tag{2.38}$$

Then we will arrive at the *partially-conserved axial current* (PCAC) for DWF [38]:

$$\Delta_\mu \mathcal{A}_\mu^b(x) = 2m_f J_5^b(x) + 2J_{5q}^a(x) \tag{2.39}$$

$$\Delta_\mu \left\langle \mathcal{A}_\mu^b(x) O(y) \right\rangle = 2m_f \left\langle J_5^b(x) O(y) \right\rangle + 2 \left\langle J_{5q}^b(x) O(y) \right\rangle + i \left\langle \delta^b O(y) \right\rangle, \tag{2.40}$$

where

$$J_5^b(x) = -\overline{\psi}(x, L_s-1) P_L t^b \psi(x,0) + \overline{\psi}(x,0) P_R t^b \psi(x, L_s-1) = \bar{q}(x)\gamma_5 t^b q(x) \tag{2.41}$$

is the pseudoscarlar density and

$$J_{5q}^b(x) = -\overline{\psi}(x, L_s/2-1) P_L t^b \psi(x, L_s/2) + \overline{\psi}(x, L_s/2) P_R t^b \psi(x, L_s/2-1) \tag{2.42}$$

is the *midpoint* term.

The first term on the right-hand side of the divergence of the PCAC (2.39) is the same contribution from the bare input quark mass as in the continuum theory. It was also shown in [38] that for operators $O(x)$ composed of only quark fields $q(x)$ and $\overline{q}(x)$, the second term involving $J_{5q}(x)$ vanishes in the limit of $L_s \to \infty$ for flavor non-singlet currents. For flavor singlet axial current, it generates the correct axial anomaly.

When L_s is finite, the midpoint contribution term symbolizes the residual chiral symmetry breaking that is unique to the DWF formulation. It is the remnant of the mixing of modes across the fifth dimension, when L_s is finite. And its leading contribution is equivalent to an additive renormalization to the bare quark mass, which is known as the residual mass m_{res}, *i.e.*

$$J_{5q}^b(x) \approx m_{\mathrm{res}} \bar{q}(x)\gamma_5 t^b q(x), \tag{2.43}$$

so the total effective quark mass becomes

$$\widetilde{m} = m_{\text{input}} + m_{\text{res}}. \tag{2.44}$$

At fixed bare coupling, the dependence of m_{res} on the extent of the fifth direction L_s can be parameterized as [52]:

$$m_{\text{res}} = c_1 \rho_H(\lambda_c) \frac{e^{-\lambda_c L_s}}{L_s} + c_2 \rho_H(0) \frac{1}{L_s}, \tag{2.45}$$

where $\rho_H(\lambda)$ represents the density of eigenmodes of the effective 4-d Hamiltonian $\mathcal{H} = -\log(\mathcal{T})$, where $\mathcal{T}$ is the DWF transfer matrix in the fifth direction that controls the mixing of chiral modes between the 4-d boundaries. The 4-d Hamiltonian, $\mathcal{H}$ is closely related to the Hermitian Wilson operator, $H_W = \gamma_5 D_W(-M_5)$, via $\mathcal{H} = 2\tanh^{-1}\left(H_W/(2+D_W)\right)$, and it has been shown that the zero modes of $\mathcal{H}$ and H_W coincide [38].

The first term in Eq. (2.45) represents contributions from eigenmodes with eigenvalues λ greater than the mobility edge, λ_c. These modes have extended 4-d support and their contributions to m_{res} are exponentially suppressed with L_s. The coefficient of the first term is in proportion to the eigenvalue density near the mobility edge.

The second term in Eq. (2.45) corresponds to contributions from the near-zero eigenmodes of the 4-d Hamiltonian, *i.e.* eigenmodes where the 5-d transfer matrix $\mathcal{T}$ is near unity, thus allowing nearly unsuppressed mixing of the domain walls in the fifth direction. Its coefficient scales with the eigenvalue density near the origin.

In the $L_s \to \infty$ limit, the mixing of domain walls is absent for both the extended and the local modes, so both contributions vanish and the chiral limit is restored. As a consequence, the chiral limit and the continuum limit commute and the DWF formalism successfully limits the residual chiral symmetry breaking to a controllable minimum. Ambiguity in measurements with Wilson fermions for quantities that are sensitive to chiral symmetry breaking can now be resolved in a systematic manner with DWF.

In practice, even though the residual chiral symmetry breaking of DWF is already at a very low level, it is often not sufficiently small when simulating QCD with physical or slightly

heavier than physical pions. This is of particular importance in QCD thermodynamics since the simulations are based on coarse lattices with strong couplings, where the density $\rho_H(0)$ in (2.45) above can be large.

As the total bare quark mass $\widetilde{m}$ is composed of the input quark mass m_{input} and the residual mass m_{res}, there are several possible choices for us to achieve our target small value of $\widetilde{m}$.

1. Use a negative input quark mass. This is the most simple-minded way to reduce the total quark mass and is commonly adopted in the Wilson fermion scheme. This method has the benefits that it does not involving any new schemes or implementations and it will not increase the computational cost. However, it has the potential to produce a singularity in the Dirac operator in a dynamical evolution. The conjugate gradient inversion will fail to converge at when such singularity is present. Although it is not well defined for each individual configuration, the residual mass provides a "safe cushion" for the appearance of this singularity when the negative input quark mass is not too large in magnitude. According to our calculations, if the magnitude of the negative input quark mass is around or below one-third of the magnitude of the corresponding residual mass, the evolution is free of these undesired singularities (at least for all our evolutions with more than 10000 trajectories in total). With the same beta value and the same total quark mass, ensembles with either negative or positive input quark mass have been demonstrated to give the same physical results, which will be discussed in Chap. 4, 5 and 6.

2. Increase the extent of the fifth dimension L_s, which is in general a multiplicative factor to the computational expense. In practice, the typical value of L_s is between 16 and 32, which results in a computational cost one order of magnitude more expensive than a similar simulation with Wilson fermions. With larger L_s, the $1/L_s$ component of the residual mass will dominate. Thus, it becomes very inefficient to reduce m_{res} by

increasing L_s and the computational cost of a calculation with reasonable results and errors will soar to a formidable level. An attempt with L_s = 96 DWF for the QCD thermodynamics can be found in [35].

3. Möbius fermions [39, 40]. This is a generalized version of DWF which has a pair of coefficients at each site of the fifth dimension. These coefficients can be tuned to "customize" the behavior of the chiral symmetry breaking coming from different modes to attain a smaller m_{res}. Details of the Möbius fermion formulation are discussed in the subsequent subsection 2.3.4.

4. Dislocation Suppression Determinant Ratio (DSDR) [41, 42, 43]. This is a modification to the gauge action that will suppress the zero modes of the 4-D Dirac operator D_H and in turns will reduce the $1/L_s$ contribution to m_{res}. Details of DSDR are elaborated in Sec. 2.4.

More numerical results concerning the residual mass will be discussed in Sec. 4.

2.3.4 Möbius Fermions

The standard domain wall fermion formulation is characterized by a controllable chiral symmetry breaking at the expense of a fictitious fifth dimension. It is the simplest formulation of th kind, has the most straightforward physical interpretation and is relatively easy to implement for all sorts of evolutions and calculations. However, it does not necessarily offer the minimal residual chiral symmetry breaking for a given L_s. In recent years, many studies have been carried out to explore a modified or a generalized version of domain wall fermions that can reduce the residual chiral symmetry breaking at a fixed L_s. Among them, optimum domain wall fermions proposed in Ref. [56], as suggested by its name, gives the minimal residual mass for a given L_s, and Möbius domain wall fermions (MDWF/Möbius Fermions) introduced in Refs. [39, 40] is a highly customizable generalization of plain do-

main wall fermions. The latter of the two is widely used in our simulation requiring pions of physical mass. Thus in this subsection, we will focus our introduction on Möbius domain wall fermions. Many theoretical derivations and details of the technical implementation of MDWF can be found in Hantao Yin's thesis [57].

Before we delve into the definition and characteristics of Möbius domain wall fermions, let us first turn to the Ginsparg-Wilson fermions for a moment. As enforced by the aforementioned Nielsen-Ninomiya no-go theorem [53], we have to give up one or several essential properties of the continuum theory, for instance, hermiticity, locality, chirality and *etc.*. However, Ginsparg and Wilson [58] redefined the chiral symmetry on the lattice with the following so-called GW-relation

$$\gamma_5 D + D\gamma_5 = D\gamma_5 D \, . \tag{2.46}$$

If we "pretend" that the GW-relation is the chiral symmetry for lattice fermions, then we will be able to construct a lattice fermion formulation that boasts all the important symmetries and characteristics shared by the continuum theory.

In 1997, Herbert Neuberger proposed a fermion formalism [59, 60], the *overlap fermions*, that satisfies the GW-relation. Its Dirac operator depends on a sign function of a certain Hermitian Wilson-type Dirac operator,

$$D_{OV}(H_W) = \frac{1}{2}\left(1 + m + (1-m)\gamma_5 \epsilon(H_W)\right). \tag{2.47}$$

In Neuberger's original overlap formalism, the kernel of the sign function is the Hermitian Wilson Dirac operator $H_W = \gamma_5 D_W$. Yet there exists an equivalence relation between DWF and overlap fermions as the former can be regarded as an approximation to the latter. The plain domain wall formulation (Shamir DWF) can be expressed in the form of of Eq. (2.47), with H_W replaced by the Shamir kernel $H_T = \gamma_5 D_W (2 + D_W)^{-1}$ and the ideal sign function replace by following truncated version,

$$\epsilon(x) = \frac{(x+1)^{L_s} - (x-1)^{L_s}}{(x+1)^{L_s} + (x-1)^{L_s}}, \tag{2.48}$$

where the exponent L_s is the length of the fifth dimension.

Now we have a new perspective for residual chiral symmetry breaking with the DWF formulation: the deviation of Eq. (2.48) to the ideal sign function. Fig. 2.1 shows the numerical results for the approximated $\epsilon(x)$ for DWF and its deviation from the ideal sign function for a selected set values of L_s [57]. It is also revealed in Fig. 2.1 that the deviation

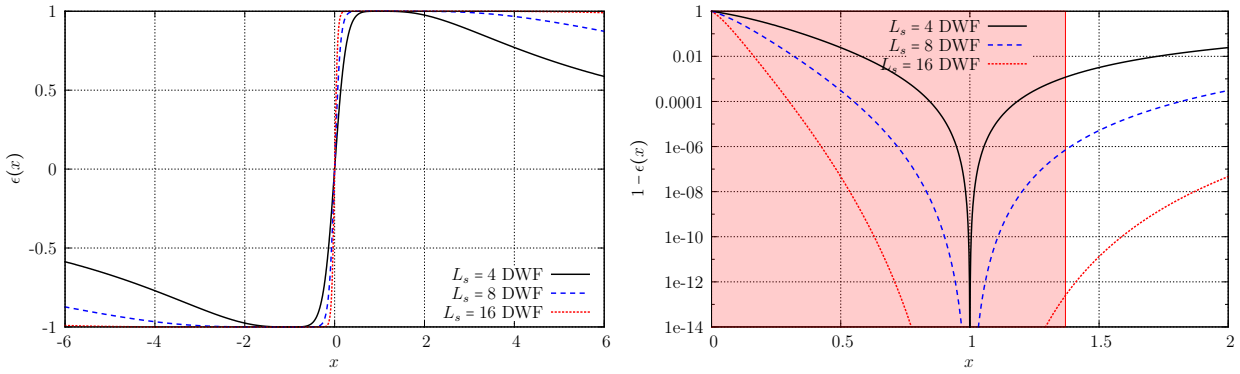

Figure 2.1: Left: plot of $\epsilon(x)$ for the domain wall fermion actions with $L_s = 4, 8, 16$. Right: plot of $\log(1-\epsilon(x))$ for different values of L_s . The shaded region denotes the approximate range of the eigenvalues of the H_T kernel.

comes from two parts, modes that are very close to the origin and modes that approach infinity. The first contribution is usually dominant since the larger modes always have a upper bound due to the lattice cut-off. However, both contributions must be considered when one tries to improve the approximation to the sign function for Shamir domain wall fermions.

The Möbius domain wall fermion formulation is motivated to augment the plain domain wall fermions with more parameters that can be tuned to achieve a better approximation to the sign function. Now let us proceed to give the definitions of the five-dimensional Möbius fermion action and its Dirac operator,

$$S_F^M = \sum_{x,s;x',s'} \overline{\psi}(x,s) D_M(x,s;x',s') \psi(x',s'), \tag{2.49}$$

where $D_M(x,s;x',s')$ is the Möbius Dirac operator:

$$D_{xs;ys'} = D^s_+(x,y)\delta_{s,s'} + D^s_-(x,y)m_s P_+ \delta_{s,s'+1} + D^s_-(x,y)m_{s+1}P_-\delta_{s,s'-1}. \tag{2.50}$$

Here D^s_+ and D^s_- are shifted Wilson Dirac operators defined as

$$D^s_+(x,y) = b_s D_W(x,y) + 1 \tag{2.51}$$

$$D^s_-(x,y) = c_s D_W(x,y) - 1, \tag{2.52}$$

where $D_W(x,y)$ is the Wilson Dirac operator (2.22). The function m_s in Eq. (2.50) is the 5-d mass matrix shared with the Shamir domain wall fermion formalism (2.32).

This Möbius Dirac operator is in its most generic form with L_s pairs of free parameters b_s and c_s for each five-dimensional plane in addition to the original domain wall fermion parameters. With transformations and derivations presented in [40], it can be shown that this Möbius Dirac operator corresponds to a overlap Dirac operator given by an expression similar to Eq. (2.47):

$$D_{OV}(H_M) = \frac{1}{2}\left(1 + m + (1-m)\gamma_5 \epsilon(H_M)\right), \tag{2.53}$$

$$\epsilon(H_M) = \frac{S-1}{S+1}, \tag{2.54}$$

$$S = \prod_s \frac{H^s_T + 1}{H^s_T - 1}, \tag{2.55}$$

$$H^s_T = (b_s + c_s)\gamma_5 D_W \left(2 + (b_s - c_s)D_W\right)^{-1}. \tag{2.56}$$

These sophisticated expressions can be simplified if we employ the following constraints:

1. All $b_s = b$ and $c_s = c$, making b_s and c_s constant along the s-direction;

2. $b - c$ is fixed to 1.

Now the quivalent overlap operator becomes

$$\epsilon(x) = \frac{(\lambda x + 1)^{L_s} - (\lambda x - 1)^{L_s}}{(\lambda x + 1)^{L_s} + (\lambda x - 1)^{L_s}}, \tag{2.57}$$

where $\lambda = b + c$ is still left as a free parameter subject to tuning. This is the basic setup for the MDWF we have adopted for our finite temperature simulations.

Following a Taylor expansion of $\epsilon(x)$ about $x = 0$, the Möbius DWF operator turns out to be a very good approximation to that of the plain DWF Dirac operator, if we set $\lambda = L_d/L_m$. Here L_d and L_m are respectively extents of the fifth dimension of Shamir DWF and Möbius DWF under comparison. In other words, we are able to shrink the auxiliary fifth dimension with a fact of of $\lambda = b + c = 2c + 1$ once we switch from Shamir DWF to Möbius DWF. Based on this argument, we can use large λ (or equivalently large c) instead of large L_s to save computational cost. However there are at least two loopholes behind this simple-minded deduction [57]:

1. Such great approximation from Taylor expansion no longer holds when λ or λL_s is very large. Keeping $L_s \times \lambda$ fixed, there exists an optimum choice of λ that will minimize the residual mass;

2. If we adopt λ close to the optimum value or even larger, much of the chiral symmetry breaking begins to come from large eigenvalues of the overlap kernel while less chiral symmetry breaking comes from eigenvalues near zero. This is achieved by making the step function very steep which produces large forces and requires a smaller step size, slowing down the evolution significantly.

To circumvent these issues, we need to perform several scans in search for the optimum choice of λ that will minimize the overall computational cost and give minimum m_{res} that is required for our simulations with physical pions. Details of the scans can be found in [57] and also in Chap. 4.

The optimum domain wall fermion method, on the other hand, utilizes the Zolotarev optimal rational approximation to approximate the sign function, which is theoretically the best one as measured by the minimum of the maximum deviation (L_∞ measure). However, it loses the mirror symmetry in the fifth dimension and thus brings some extra ambiguity

and difficulty in computation. Moreover, it is plagued with a severe slow-down in evolutions similar to the one mentioned above. Based on these considerations, we choose the more flexible MDWF formalism over the optimum DWF in our thermodynamics simulations with physical pions.

The construction of the 4-d fermions fields and the partially-conserved axial current of MDWF is more complicated and contains more arbitrariness than the plain DWF. We can choose a set of definitions parallel to the plain DWF. Details can be found in [57] and we simply quote the results below. The 4-d physical fermion fields are defined as follows,

$$q(x) = P_-\psi_0(x) + P_+\psi_{2N-1}(x) \tag{2.58}$$

$$\overline{q}(x) = -\sum_y \overline{\psi}_{2N-1}(y) D_-^{2N-1}(y,x) P_- - \sum_y \overline{\psi}_0(y) D_-^0(y,x) P_+. \tag{2.59}$$

Formally J_5 and J_{5q} are defined the same as the DWF in Eqs. 2.41 and 2.42. Nevertheless, the Dirac propagator $D_{\rm dwf}^{-1}$ used in calculating the correlator in the DWF formulation should be replaced by $D^{-1}D_-$ in the MDWF formulation.

2.4 Dislocation Suppression Determinant Ratio (DSDR)

Let us restate below the dependence of $m_{\rm res}$ on L_s in Eq. (2.45):

$$m_{\rm res} = c_1\rho_H(\lambda_c)\frac{e^{-\lambda_c L_s}}{L_s} + c_2\rho_H(0)\frac{1}{L_s},$$

The exponentially decaying contribution which results from the extended eigenmodes will drop shapely when one increases L_s. The second contribution, however comes largely from localized dislocations in the gauge field corresponding to topology change [61, 62, 63]. At strong coupling, gauge field dislocations rapidly become more common, so that the dominant contribution to $m_{\rm res}$ comes from the near-zero eigenmodes of $\mathcal{H}$ and the second, power-suppressed term in Eq. (2.45) dominates. This effect becomes more prominent when L_s is already very large.

One method to reduce the large residual chiral symmetry breaking is to augment the gauge action with the determinant of the 4-d Hermitian Wilson Dirac operator, $H_W(-M_5) = \gamma_5 D_W(-M_5)$ [41, 42, 43], where M_5 is the domain wall height ($M_5 = 1.8$ in our calculations). Including this determinant as a weighing factor in the path integral explicitly suppresses those configurations which have a small eigenvalue of H_W, and especially also those with near-zero modes of $\mathcal{H}$.

Unfortunately, the suppression of the zero modes of H_W also suppresses exactly those configurations that change topology during a molecular dynamics evolution. Therefore, in order to allow for the correct sampling of all topological sectors, we augment the Wilson Dirac operator with a chirally twisted mass,

$$D_W(-M_5) \to D_W(-M_5 + i\epsilon\gamma_5) \; . \tag{2.60}$$

We then employ the following ratio of weighting factors on the gauge fields:

$$\begin{aligned} \mathcal{W}(M_5, \epsilon_b, \epsilon_f) &= \frac{\det\left[D_W^\dagger(-M_5 + i\epsilon_f\gamma_5) D_W(-M_5 + i\epsilon_f\gamma_5)\right]}{\det\left[D_W^\dagger(-M_5 + i\epsilon_b\gamma_5) D_W(-M_5 + i\epsilon_b\gamma_5)\right]} \\ &= \frac{\det\left[D_W^\dagger(-M_5) D_W(-M_5) + \epsilon_f^2\right]}{\det\left[D_W^\dagger(-M_5) D_W(-M_5) + \epsilon_b^2\right]}. \end{aligned} \tag{2.61}$$

The bosonic and fermionic "twisted-mass" parameters ϵ_b, ϵ_f can be tuned so that gauge field topology changes at a reasonable rate during the Hybrid Monte Carlo (HMC) evolution, but the localized dislocations which contribute to the residual mass are suppressed [44]. We call the weighting factor $\mathcal{W}(M_5, \epsilon_b, \epsilon_f)$ the Dislocation Suppressing Determinant Ratio.

Employing the DSDR in our action ensures that the ultraviolet modes of the theory are minimally affected so that bare parameters such as β and the quark masses do not shift significantly from those used in the standard domain wall fermion action. With these precautions, the calculations using the DSDR action are very similar to those with the standard Wilson or Iwasaki action but bring the benefit of a much lower residual mass *c.f.* [44].

Chapter 3

QCD Phase Transition and the Symmetries of QCD

This chapter starts with an overview of the theoretical and experimental investigations of the QCD phase transition. It is followed by a brief introduction to the chiral and $U(1)_A$ symmetries that are tightly connected with the QCD phase transition.

3.1 Overview of QCD at Finite Temperature and Density

$SU(3)$ Quantum Chromodynamics is now widely accepted as the fundamental complete description of the strongly interacting nuclear force. However, due to the non-perturbative nature of $SU(3)$ gauge theory, many aspects of QCD are yet to be understood. Among them, the phase structure of QCD is one of the most fundamental issues that intrigues physicists both in theory and in experiment.

At ordinary temperature and conditions, quarks and gluons are confined within hadrons. In contrast, at extremely high temperature, quarks become weakly interacting and the

hadronic matter is expected to turn into a brand new state, "the quark gluon plasma" (QGP) [64], which displays properties that resemble a perfect fluid. Similar transitions may also take place for quark matters at extreme density, which is speculated to be a candidate for the composition of a neutron star [65]. Such hot and dense quark matter is presumably also present at an early stage ($\lessapprox 10\mu s$) of the universe after the Big Bang. Thus, a better characterization of the QCD phase transition would deepen profoundly our understanding of the evolution of the universe. Fig. 3.1 shows a qualitative sketch of the phase diagram of the quark matter [3].

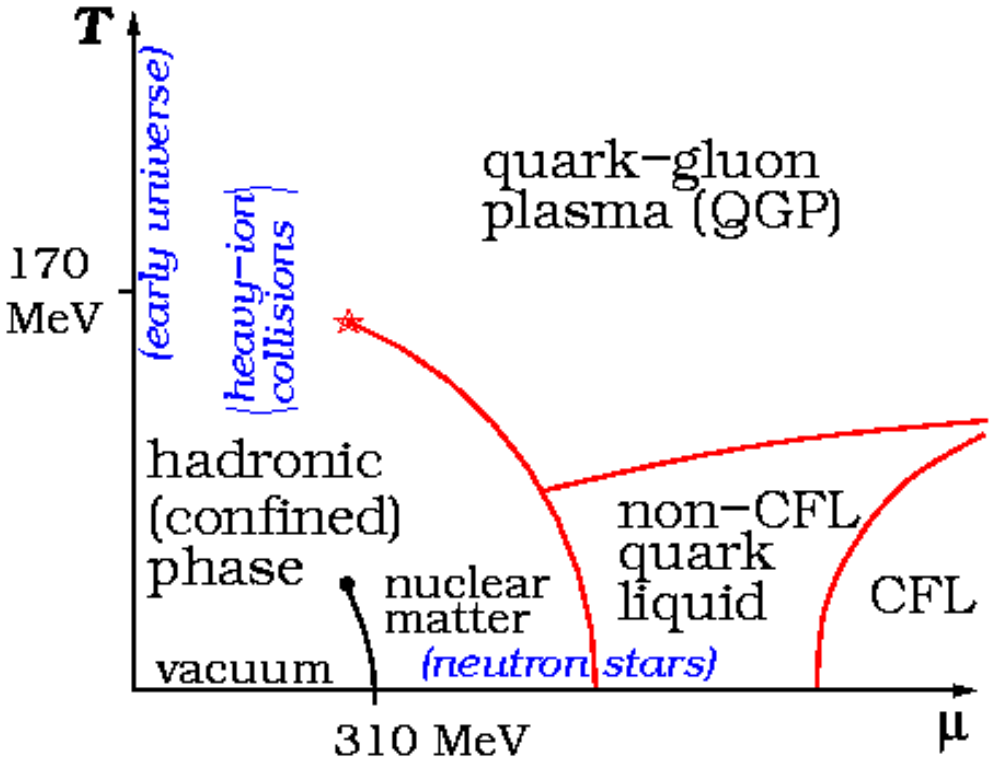

Figure 3.1: A qualitative sketch of the phase diagram of quark matter in temperature-density space [3].

At present, the heavy-ion community is trying to replicate these extreme conditions in ongoing as well as future heavy-ion collision experiments that are carried out at various facilities, for instance Relativistic Heavy Ion Collider (RHIC), Large Hadron Collider (LHC),

Facility for Antiproton and Ion Research (FAIR), and Nuclotron-based Ion Collider Facility (NICA). All the following phenomena and many others are expected to be experimental signatures for the formation of the QGP phase:

Strangeness Enhancement Strangeness is absent from the initial state of the heavy-ion collision, as the ordinary nucleons are all composed of up and down (u, d) valence quarks. When the QGP is formed, abundant strange anti-strange quark pairs $(s\bar{s})$ are created. As they move freely within the hot and dense medium, $\bar{s}$ can readily find a u or d quark to form K^+ or K^0 mesons. However, it would be less likely for a s quark to find $\bar{u}$ or $\bar{d}$ quark. Thus, the production of strangeness is a good indicator for the existence of QGP [66]. This signature has been captured in many experiments, as reported in [66, 67, 68, 69, 70].

J/Ψ **Suppression** J/Ψ, or charmonium, is the bound state of a $(c\bar{c})$ pair that is expected to be created in the hot QCD medium. The binding force can successfully hold the pair together if the two quarks are within the color Debye screening length. However, if the hot matters enters the QGP phase, the decreased screening radius may fall short of the binding radius, which will result in the meltdown of J/Ψ [71]. Consequently, the suppression of charmonium production in the heavy-ion collision as compared to that from baseline production in the nucleon-nucleon collisions provides a signal for the QGP phase. Some information was collected at Super Proton Synchrotron (SPS) [72, 73]. However, when the abundance of charmonium generated in the heavy-ion collission exceeds a certain level at sufficiently high energy, charmonium suppression might be reversed, becoming charmonium enhancement [74].

Jet Quenching In hadronic collisions, due to the hard momentum transfer, some quark-gluon constituents will be knocked out of the interacting medium and form hadrons, which are referred as "jets". However, if these quark-gluon constituents have to experience the QGP medium before escaping, they will suffer a substantial amount of

energy loss due to their strong interaction with the medium. This so-called "jet-quenching" [75] has been observed at RHIC [76, 77] and LHC [78].

Chiral Phase Transition All the above signatures put emphasis on the quark deconfinement aspects of the phase transition. It is also expected that chiral symmetry is also restored in the QGP phase, although its critical temperature might differ slightly from the deconfinement critical temperature. The effective mass of some mesons, ϕ for instance, is sensitive to the chiral symmetry, while the properties of leptons are preserved as they are not participants in the strong interactions. This would result in a shift of the decaying branching ratio for these mesons [79], which could provide an informative probe of the restoration of chiral symmetry. This aspect of the QCD phase transition is the central topic of this thesis. More discussion can be found in the following section and in the rest of this thesis.

Despite the success in the discovery of this new form of QCD matter (for reviews *c.f.* [80, 81, 82]), locating the phase boundaries and pinpointing the pseudo-critical temperature remain puzzles to be solved.

In theory, the phase transition is indicated by the divergence of a sufficiently high order derivative of the free energy density at a critical temperature. For a non-vanishing quark mass, as in the real world, the notion of a critical temperature becomes obscured and a pseudo-critical temperature is introduced to locate the crossover transition behavior. In this work, we define a pseudo-critical temperature at the peak of the disconnected piece of the chiral susceptibility, χ_{disc}.

A variety of continuum studies both from QCD and first principles as well as from its low energy effective theory have been devoted to resolve the QCD phase transition (for reviews *c.f.* [83, 84, 85, 86]). On the other hand, lattice QCD provides important insights into thermodynamics from many perspectives. For instance, the phase transition for a pure gauge $SU(3)$ was shown to be first order with $T_c \approx 240$ MeV [87, 88], consistent with the

effective theory prediction [89]. The equation of state for QCD can also be determined from the lattice formulation, with some most recent progress reported in Refs. [90, 91]. Despite the "sign problem" in Euclidean space, many efforts have been devoted to introduce a finite chemical potential on the lattice so that a study of finite-density QCD is accessible. A variety of techniques have been developed in [92, 93, 94, 95, 96, 97, 98, 99].

The majority of these exploration of QCD thermodynamics using lattice QCD employ staggered fermions, which suffer from additional breaking of the full chiral and anomalous $U(1)_A$ symmetries due to lattice artifacts. These effects will not disappear until a continuum limit is taken where demanding computational cost and careful extrapolation are required. Domain wall fermions and other variants of chiral fermions are ideally suited to study the chiral and anomalous $U(1)_A$ symmetries and their degree of restoration with increasing temperature, which is a natural focus of this thesis.

3.2 Symmetries Associated with QCD Phase Transition

In the limit of N_f flavors of vanishing quark masses, QCD possesses a chiral $SU(N_f)_L \times SU(N_f)_R$ symmetry. However, the QCD vacuum does not respect this symmetry. Instead the non-vanishing vacuum expectation value of $SU(N_f)_L \times SU(N_f)_R$ non-invariant operator $\overline{\psi}\psi$ reflect a smaller, $SU(N_f)_V$ vacuum symmetry. This symmetry-breaking vacuum order parameter $\langle\overline{\psi}\psi\rangle$ is expected to disappear at high temperature implying a phase transition separating a low-temperature chirally asymmetric phase from a high-temperature phase with restored chiral symmetry. The order of the transition depends on the number of flavors of light quarks. As argued in Ref. [25], QCD with $N_f \geq 3$ will undergo a first-order chiral phase transition. For a 2-flavor theory, the order of the phase transition may further depend on the degree to which the anomalous $U(1)_A$ symmetry is realized in QCD. For a massive QCD, the

order of the phase transition will depend on the quark mass as well as the non-zero baryon chemical potential as demonstrated in Fig. 3.2([4]).

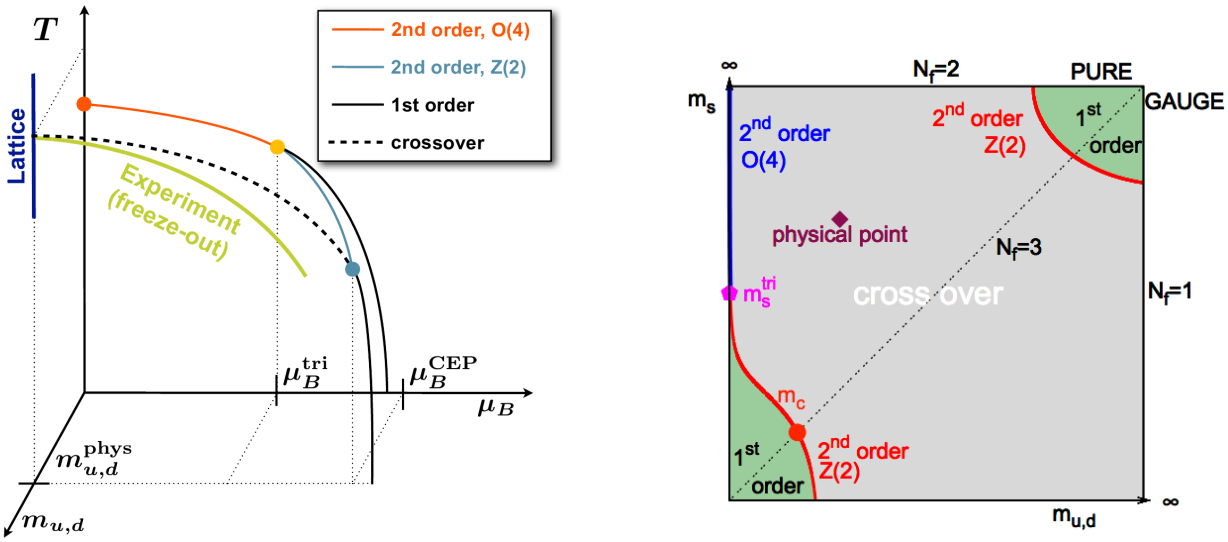

Figure 3.2: Left panel shows the conjectured phase diagram of QCD in the space of temperature, baryon chemical potential and light quark mass [4]. The solid blue line labelled by "Lattice" marks the chiral transition region at vanishing baryon chemical potential ($\mu_B = 0$) and physical quark masses, the focus of this work. Right panel is the "Columbia plot", the phase diagram of QCD in the light-strange quark mass plane at vanishing chemical potential.

The $U(1)_A$ symmetry, which is respected by QCD at the classical level, is broken by the axial anomaly. This results in both the anomalous term in the conservation law for the $U(1)_A$ axial current of Adler [100] and Bell and Jackiw [101] as well as 't Hooft's explicit violation of the global symmetry [102] arising from fermion zero modes associated with topologically non-trivial gauge field configurations. At low temperatures this anomalous $U(1)_A$ symmetry is also broken by the QCD vacuum. However, above the QCD phase transition vacuum symmetry breaking has disappeared and the effects of the axial anomaly can be studied directly.

At sufficiently high temperatures anomalous $U(1)_A$ symmetry breaking can be studied

using the dilute instanton gas approximation (DIGA) [103, 104]. In this approximation one finds exponential suppression of the instanton density as the gauge coupling decreases so that the $U(1)_A$ symmetry becomes exact in the limit $T \to \infty$. When the DIGA is justified, the $U(1)_A$ symmetry breaking effects it predicts are very small. With decreasing temperature, the semi-classical approximation underlying the dilute instanton gas picture becomes unreliable and the degree of anomalous symmetry breaking becomes a non-perturbative question well suited to a DWF lattice study. While one might imagine that anomalous $U(1)_A$ breaking remains small as the temperature decreases from asymptotically large values, even down to the critical temperature, T_c, it is also possible that new, non-perturbative phenomena emerge at lower temperatures leading to a significant topological charge density and to large $U(1)_A$ symmetry breaking.

As aforementioned, the degree of $U(1)_A$ symmetry breaking may have interesting consequences for the order of the 2-flavor massless QCD chiral phase transition. Namely, if the $U(1)_A$ breaking is significant near the phase transition, then the resulting four massless degrees of freedom ($\vec{\pi}$ and σ) can support $O(4)$ critical behavior at T_c, the location of the phase transition. However, if anomalous breaking of the $U(1)_A$ is small so there are eight light degrees of freedom at T_c ($\vec{\pi}$, σ, $\vec{\delta}$ and η) then the chiral transition is expected to be first order, although a second order phase transition may still be permitted with a different $SU(2)_L \times SU(2)_R / U(2)_V$ universality class as suggested in Refs. [105, 106]. Thus, a thorough study of the behavior of the anomalous $U(1)_A$ symmetry has essential consequences for the nature of the chiral phase transition.

In heavy-ion collision experiments, it may also be possible to observe signatures of $U(1)_A$ symmetry restoration through measurements of low-mass dileptons [107]. Moreover, an effective restoration of the axial $U(1)_A$ symmetry above T_c may lead to softening of the η' mass resulting in interesting experimental signatures [108, 109, 110]. In fact, recently it has been claimed that the results from the RHIC suggest softening of the η' mass indicating partial

restoration of the $U(1)_A$ symmetry in hot and dense matter [111]. Hence, studies related to $U(1)_A$ symmetry restoration with increasing temperature have important theoretical and phenomenological consequences.

Chapter 4

Simulation Details

This chapter focuses on setting up the basic parameters for the generation of our finite temperature ensembles with DWF/MDWF. We start with the determination of the line of constant physics, followed by several tables listing the parameters that we adopt in practical simulations. Detailed explanations are provided for certain aspects that need some attention. We also present some very recent results from a zero temperature ensemble to verify our choices for the parameters. In the third section, a brief summary for the plaquette is discussed. In the last section of this chapter, we present a thorough discussion for the numerical results of the residual mass that is essential for the DWF/MDWF calculation.

Note that the results from the zero-temperature ensembles presented in the chapter are last updated when the relevant calculations for the line of constant physics were performed. The results from some of these zero ensembles have since been improved and thus may be different from those presented here.

4.1 Determine the Line of Constant Physics

In some earlier explorations of QCD phase transition with DWF *c.f.* [33, 35] the total bare quark mass wes held constant instead of the total physical quark mass due to the lack of

relevant data and the difficulty in tuning the residual and the total quark mass. This resulted in a pion mass changing from $m_\pi \approx 225$ MeV at the lowest temperature to $m_\pi \approx 275$ MeV at the highest temperature for these studies. The 20% difference in the pion mass could in turn causes ambiguities in determining the pseudo-critical temperature and the breaking and restoration of various symmetries associated with the QCD phase transition. Fortunately, we have now collected reasonable statistics from zero-temperature ensembles that allows us to determine a line of constant physics (LCP) with a pion mass fixed at 200 MeV or even lower.

Before we start, let us present some of the features of the zero-temperature ensembles that are listed in Table 4.1. All these ensembles were generated with the Iwasaki + DSDR

#	β	N_σ	N_τ	L_s	m_l	m_s	m_{res}	m_π (MeV)	N_{traj}
1	1.70	16	32	32	0.013	0.047	0.00420(2)	394(9)	1360
2	1.70	16	32	32	0.006	0.047	0.00408(6)	303(7)	1200
3	1.75	16	16	32	0.006	0.037	-	-	2242
4	1.75	32	64	32	0.0042	0.045	0.00180(5)	246(5)	1288
5	1.75	32	64	32	0.001	0.045	0.00180(5)	172(4)	1560
6	1.82	16	32	32	0.013	0.040	0.00062(2)	398(9)	2235
7	1.82	16	32	32	0.007	0.040	0.00063(2)	304(7)	2134

Table 4.1: Summary of zero temperature ensembles with the DSDR action. Each lattice ensemble is given a label for later reference. The total molecular dynamics time per trajectory is $\tau = 1.0$. The residual mass, m_{res} is also tabulated. The values given for run # 5 are zero temperature results from RBC-UKQCD [1, 2]

.

gauge action and $2 + 1$ flavors of DWF action. Some of the ensembles have been expanded to include additional configurations, which were not used in the process of determining the

input parameters. Therefore in this section, we present the results just as they were when we chose the parameters for our finite temperature simulations. A recently generated zero temperature ensemble with new results will be discussed in Sec. 4.2 after we present choice of the parameter that were used in the finite temperature ensembles reported here.

4.1.1 LCP for $m_\pi \approx 200$ MeV Ensembles

For the DSDR ensembles, we have endeavored to move along a line of fixed physical pion mass, $m_\pi = 200$ MeV. Table 4.2 summarizes our results for m_π, m_ρ, and r_0 on the zero temperature ensembles.

#	β	m_l	r_0	m_ρ	m_π	$1/a^\dagger$ (GeV)
1	1.70	0.013	2.895(11)	0.68(2)	0.310(1)	-
2		0.006	2.992(27)	0.67(2)	0.238(1)	-
Extrapolated		-0.0040	3.13(7)	0.66(6)	-	1.27(4)
4	1.75	0.0042	3.349(20)	0.57(2)	0.1810(3)	-
5		0.0010	3.356(22)	0.56(2)	0.1264(3)	-
Extrapolated		-0.0018	3.36(4)	0.56(4)	-	1.36(3)
6	1.82	0.013	3.743(28)	0.56(2)	0.255(2)	-
7		0.007	3.779(37)	0.53(2)	0.195(2)	-
Extrapolated		-0.00064	3.83(9)	0.49(5)	-	1.55(5)

Table 4.2: Results for r_0, m_ρ, m_π, and the lattice scale, a^{-1}. At each value of β, we perform simple linear extrapolations to $m_l = -m_{\rm res}$, *i.e.*, the chiral limit, for r_0 and m_ρ. The lattice scale is fixed using the extrapolated value for r_0. †Lattice scale determined using $r_0 = 0.487(9)$ fm.

In order to determine the lattice scale, we have used the Sommer parameter r_0, determined from the static quark potential. The quantity r_0, extrapolated to the chiral limit, can

be related to the lattice scale using its physical value $r_0 = 0.487(9)$ fm, determined in earlier domain wall fermions caculations [112]. The temperature is given by $T = 1/N_\tau a$. The values for r_0/a in Table 4.2 allow us to determine the bare couplings needed for finite temperature lattice ensembles in the transition region.

To describe $T(\beta)$ in physical units, we use a modified form of the two-loop renormalization group running, which includes an extra term incorporating the $\mathcal{O}(a^2)$ lattice artifacts:

$$T(\beta) = \frac{1}{N_\tau a(\beta)} = \left(c_0 + c_1 \hat{a}^2(\beta)\right) \frac{1}{\hat{a}(\beta)} \tag{4.1}$$

$$\hat{a}(\beta) = \exp\left(-\frac{\beta}{12 b_0}\right)\left(\frac{6 b_0}{\beta}\right)^{-b_1/(2b_0^2)};\ b_0 = \frac{9}{(4\pi)^2};\ b_1 = \frac{64}{(4\pi)^4}, \tag{4.2}$$

where $\hat{a}(\beta)$ describes the continuum two-loop RG running at the lattice spacing. The left panel of Fig. 4.1 shows the result of the fit of the β-dependence of the temperature to both the lattice-corrected RG fit of Eq. (4.1), and to the continuum RG running, *i.e.*, the case where $c_1 = 0$. As can be seen, the lattice-corrected fit provides a better description of the data.

To ensure that we simulate along a line of fixed pion mass, we must account for the running of the bare quark masses as the bare coupling is changed. Since the residual chiral symmetry breaking results in an additive shift in the quark mass, to leading order in chiral perturbation theory, the pion mass depends on the total quark mass, $\widetilde{m}_l = m_l + m_{\rm res}$, as:

$$m_\pi^2 \propto (m_l + m_{\rm res}). \tag{4.3}$$

This linear quark mass dependence is a surprisingly good description of earlier data [112] and sufficiently accurate for the present purpose.

This allows us to determine the bare quark masses required for a specific line of constant physics from the zero temperature ensembles listed in Table 4.2. Figure 4.2 shows the quark masses required for $m_\pi = 200$ MeV. We also fit these results for $\widetilde{m}_l(\beta)$ to the lattice-corrected two-loop running of the mass anomalous dimension:

$$\widetilde{m}_l \equiv (m_l + m_{\rm res}) = \left(A + B\hat{a}^2(\beta)\right)\left(\frac{12 b_0}{\beta}\right)^{4/9} \tag{4.4}$$

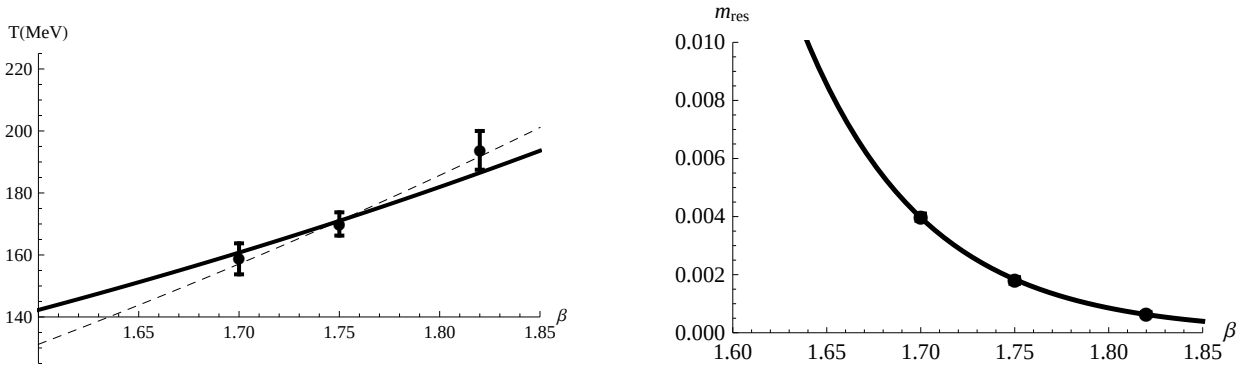

Figure 4.1: Left panel: temperature for $N_\tau = 8$ is plotted versus β. The solid curve is the fit to the continuum RG running; $c_0 = 25.2(3)$ MeV. The dashed curve is the result of the fit to Eq. (4.1) which includes an added a^2 correction; $c_0 = 29.7(2.9)$ MeV, $c_1 = -204(132)$ MeV. Right panel: $m_{\rm res}a$ is plotted versus β with an exponential fit: $m_{\rm res}(\beta) = A\exp(-B\beta)$; $A = 8.7(9.7) \times 10^8$, $B = 15.4(6)$.

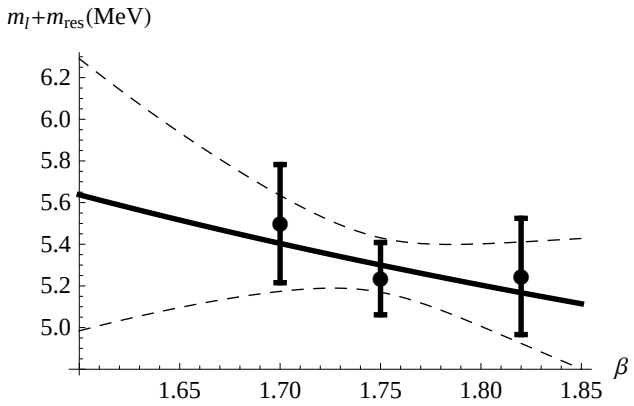

Figure 4.2: Total light quark mass for the $m_\pi = 200$ MeV line of constant physics, with a fit to the lattice-corrected mass anomalous dimension. Dashed curves represent the 1-σ error band.

This lattice-corrected fit provides a good interpolation formula that allows us to achieve a line of constant physics on the finite temperature ensembles.

Finally, we must estimate the residual mass at different values of β.. The zero temperature ensembles show that the residual mass is strongly dependent on the lattice spacing. At coarser lattice spacings, the localized dislocations of gauge fields are more common and cause m_{res} to increase rapidly as one moves from high to low temperature. The right panel of Fig. 4.1 shows m_{res} as a function of β. We find that a simple exponential ansätz describes the data well.

4.1.2 LCP for $m_\pi \approx 135$ MeV Ensembles

As revealed by the equivalence relations in Eqs. (2.47) and (2.53), both plain DWF and MDWF are approximations to overlap fermions and are thus approximations to each other. Consequently the adoption of Möbius domain wall fermions has minimal effects on the lattice spacing, and we can safelyare keep our β values and the corresponding temperatures unchanged from the $m_\pi \approx 200$ DWF esembles. Hence the only quantities that need to be determined for the Möbius domain wall fermion sembles at $m_\pi \approx 135$ are the total bare quark mass and the residual mass. In this subsection we will focus on the former and leave the latter to Section 4.4 later in this chapter.

From our zero temperature ensembles, run $\#4$ and run $\#5$ with $\beta = 1.75$ and $L_s = 32$, we have determined the following values that should correspond to physical pion and kaon masses [1, 2], We can calculate the scale change appropriate to a given shift in β from a simple exponential extrapolation

$$a_2/a_1 = \exp(s(\beta_2 - \beta_1)), \tag{4.5}$$

where $s = 1.66$ can be determined from the extrapolated results of $\beta = 1.70$ and $\beta = 1.82$ in Table 4.2.

a^{-1}	1.371 GeV
m_{res}	0.001842
$\widetilde{m}_l$	0.001752
$\widetilde{m}_s$	0.048552

Table 4.3: Extrapolation of ensembles in run # 4 and run # 5 to the physical pion point.

Using the scale factor s, $\widetilde{m}_l$ and $\widetilde{m}_s$ from the $\beta = 1.75$ ensemble, we can find the total quark masses at other values of β, if we know the relative quark renormalization factors, Z. The Z factors to convert to $\overline{\text{MS}}(\mu = 2 \text{ GeV})$ scheme are given later in Table 6.4. We want to keep $Z_m \widetilde{m}_f / a$ a constant, namely

$$\widetilde{m}_f(\beta) = \frac{Z_m(1.75)\widetilde{m}_f(1.75)a(\beta)}{Z_m(\beta)a(1.75)}. \tag{4.6}$$

In Table 4.4 we show the estimated values for $\widetilde{m}_l(\beta)$ and $\widetilde{m}_s(\beta)$ Note that the results

β	T (MeV)	$\widetilde{m}_l(\beta)$	$\widetilde{m}_s(\beta)$
1.633	139	0.00222	0.0616
1.671	149	0.00206	0.0571
1.707	159	0.00192	0.0531
1.740	168	0.00179	0.0496
1.771	177	0.00168	0.0465
1.801	186	0.00158	0.0437
1.829	195	0.00149	0.0414

Table 4.4: The estimated value for the total quark mass of ensembles that lie on a line of constant physics with m_π at physical value.

in Table 4.4 keep the ratio of $\widetilde{m}_s/\widetilde{m}_l$ fixed at 27.71, which is the value from the quark masses for $\beta = 1.75$ obtained from our customary global fits. Although the scaling formula in Eq. (4.6) is simpler than the lattice corrected Eq. (4.4), the lattice scales and temperatures

are essentially the same.

4.2 Parameter Settings of the Ensembles

4.2.1 $m_\pi \approx 200$ MeV Ensembles

Tables 4.5, 4.6, and 4.7 list the basic parameters for the three sets of ensembles. All of them share the same choices of the input quark masses, which are adjusted to bring the pion mass close to the $m_\pi = 200$ MeV target. They only differ in their spatial volumes, which are of $32^3 \times 8$, $24^3 \times 8$, and $16^3 \times 8$. All three ensemble sets cover the temperature region around the QCD phase transition. The $16^3 \times 8$ simulations produced 8 ensembles roughly evenly separated, in a range between $T = 139$ MeV and 195 MeV with the exception of 2 ensembles with different input quark masses at $T = 149$ MeV. The $24^3 \times 8$ ensembles cover a narrower region with 5 temperatures between $T = 149$ MeV and 186 MeV. The ensembles with the largest volume $32^3 \times 8$ have almost the same temperature values as the $16^3 \times 8$ ensembles, except that there is an extra point at $T = 164$ MeV and only one ensemble at $T = 149$ MeV, obtained with a negative input quark mass.

For all the ensembles listed in Tables 4.5, 4.6, and 4.7, we adopt the same Iwasaki gauge action augmented with the dislocation suppression determinant ratio (DSDR) and the domain wall fermion (DWF) action with $2 + 1$ flavors. The extent of the fifth dimension L_s for all the ensembles is 32, except for the $T = 139$ MeV ensembles and one of the $T = 149$ ensembles with $16^3 \times 8$ where L_s is set to 48. For the twisted mass coefficients in the determinant ratio, we found that the choice of $\epsilon_f = 0.02$ and $\epsilon_b = 0.5$ allows for a reasonable rate of tunneling between topological sectors while still suppresses residual chiral symmetry breaking [44].

Following the method described in the previous section 4.1, the input light quark masses are adjusted so that all the ensembles lie on a line of constant physics with $m_\pi \approx 200$ MeV

and the ratio $\widetilde{m}_l/\widetilde{m}_s = 0.088$ is fixed to ensure a physical mass strange quark. Here and later in the text, a tilde indicates the total bare quark mass, given by the sum of the input and the residual quark masses as in Eq. 2.44.

Because of the rapidly increasing residual mass with decreasing temperature, we use negative input quark masses for the two ensembles with the lowest temperatures ($T = 139$ and 149 MeV). While much larger negative input quark masses are standard for Wilson fermion calculations, the use of negative m_{input} is uncommon in a DWF calculation and, as in the Wilson case, could potentially jeopardize the stability of the evolution because of a singularity in the Dirac operator.

At $T = 139$ MeV, we initially used a negative light quark mass of $m_l = -0.00786$, with $m_{\text{res}} \approx 0.013$ at $L_s = 32$. It was quickly discovered that this resulted in a singular fermion matrix, signaled by the non-convergence of the conjugate gradient inversion. As a result, we switched to $L_s = 48$ at this temperature, where a smaller, but still negative light quark $m_l = -0.00136$ could be used to achieve the desired total light quark mass. Fortunately, we observed no "exceptional configurations" in all the following evolutions with our intentional choice of negative input quark masses that are small in magnitude.

Since this is the first time a negative input quark mass is introduced in the DWF evolution, we carried out two simulations, one with positive and one with negative input light quark masses at $T = 149$ MeV as a sanity check. Both of these ensembles (ensembles run # 9 and run # 10 in Table 4.5) correspond to approximately the same pion mass, $m_\pi \approx 200$ MeV with carefully tuned input quark masses and L_s. We did not see any significant differences between these two ensembles in quantities such as the disconnected chiral susceptibility, renormalization coefficients, or eigenvalue spectrum. However, in the chiral condensate we did see a significant difference in the two ensembles, a different that should be expected to arise from a $1/a^3$ residual breaking of chiral symmetry present in this local operator. The consistency between these two ensembles provides strong support that our interpretation of

$\widetilde{m}_l$ and choice of negative input quark mass is solid and correct.

#	T (MeV)	β	L_s	m_l	m_s	$m_{\rm res}$	$N_{\rm traj}^{\rm equil}$
8	139	1.633	48	-0.00136	0.0519	0.00588(39)	2696
9	149	1.671	32	-0.00189	0.0464	0.00643(9)	5700
10	149	1.671	48	0.00173	0.0500	0.00295(3)	6700
11	159	1.707	32	0.000551	0.0449	0.00377(11)	3359
12	168	1.740	32	0.00175	0.0427	0.00209(9)	3043
13	177	1.771	32	0.00232	0.0403	0.00132(6)	3240
14	186	1.801	32	0.00258	0.0379	0.00076(3)	4415
15	195	1.829	32	0.00265	0.0357	0.00047(1)	8830

Table 4.5: Summary of input parameters (β, L_s, m_l and m_s) and the measured results for $m_{\rm res}$ for each ensembles with $m_\pi \approx 200$ MeV at $16^3 \times 8$ space-time volume. Each is assigned a label in the first column for later reference. The final $N_{\rm traj}^{\rm equil}$ column lists the number of equilibrated trajectories that remain after the imposition of the thermalization and decorrelation cuts described in the text.

The errors quoted in the temperature column in Table 4.7 (suppressed elsewhere) are the 1-σ error from the extrapolation in Eq. (4.1). The pion mass m_π given in Table 4.7 is computed using the Gell-Mann-Oakes-Renner relation [113], indicating the ratio of the target and the calculated total quark masses, which differes from one because estimate of the residual quark mass has been replaced by its measured value. Thus, this is not an actual measurement result for m_π, but serves as a proxy of the accuracy of our estimates for the input parameters, which are interpolated fitting results. These values should not be mistaken for the actual pion masses extracted from the correlating functions measured on corresponding zero-temperature enesmbles. Nevertheless, our estimate of the input quark masses work fairly well as most of the pion masses deviate no more than 3% from the target value of 200 MeV.

#	T (MeV)	β	L_s	m_l	m_s	m_{res}	$N_{\text{traj}}^{\text{equil}}$
16	149	1.671	32	-0.00189	0.0464	0.00659(6)	4721
17	159	1.707	32	0.000551	0.0449	0.00370(4)	2265
18	168	1.740	32	0.00175	0.0427	0.00216(3)	2423
19	177	1.771	32	0.00232	0.0403	0.00129(3)	2892
20	186	1.801	32	0.00258	0.0379	0.00084(3)	3142

Table 4.6: Summary of input parameters (β, L_s, m_l and m_s) and the measured results for m_{res} for each ensembles with $m_\pi \approx 200$ MeV at $24^3 \times 8$ space-time volume. Each is assigned a label in the first column for later reference. The final $N_{\text{traj}}^{\text{equil}}$ column lists the number of equilibrated trajectories that remain after the imposition of the thermalization and decorrelation cuts described in the text.

#	T (MeV)	β	L_s	m_l	m_s	m_{res}	m_π(MeV)	$N_{\text{traj}}^{\text{equil}}$
21	139(6)	1.633	48	-0.00136	0.0519	0.00657(2)	205(8)	2700
22	149(5)	1.671	32	-0.00189	0.0464	0.00653(2)	201(5)	2700
23	159(4)	1.707	32	0.000551	0.0449	0.00366(2)	200(3)	2643
24	164(4)	1.725	32	0.00138	0.0436	0.00277(1)	202(3)	2700
25	168(4)	1.740	32	0.00175	0.0427	0.00220(2)	200(2)	2708
26	177(4)	1.771	32	0.00232	0.0403	0.00135(1)	198(2)	2700
27	186(5)	1.801	32	0.00258	0.0379	0.00083(2)	197(3)	2729
28	195(6)	1.829	32	0.00265	0.0357	0.00049(1)	195(4)	3112

Table 4.7: Summary of input parameters (β, L_s, m_l and m_s) and the measured results for m_{res} and the projected pion mass for each ensemble with $m_\pi \approx 200$ MeV at $32^3 \times 8$ space-time volume. Each is assigned a label in the first column for later reference. The final $N_{\text{traj}}^{\text{equil}}$ column lists the number of equilibrated trajectories that remain after the imposition of the thermalization and decorrelation cuts described in the text.

The number of effective trajectories for each ensemble that are used in the measurement reported later is also listed in the right-most column of Tables 4.5, 4.6, and 4.7. For ensembles with volume $16^3 \times 8$ and $32^3 \times 8$, we discard the first 300 trajectories to account for thermalization. However, because we changed the evolution algorithm during the early stages of the generation of the $24^3 \times 8$ ensembles, a larger number of initial trajectories were discarded for those. For each ensemble, each trajectory has a uniform length of one molecular dynamics time unit.

In order to increase the statistics, we have evolved multiple streams for ensembles corresponding to run # 16 and run # 17. Ensemble run # 16 is composed of 8 streams, two of which began from an ordered start, another two from a disordered start and the remaining four were split from the previous four streams after thermalization. Ensemble run # 17 is composed of two streams one beginning from an ordered and the other from a disordered configuration. The multiple streams in each ensemble are pooled together after removing an initial 300 trajectories from each stream with a fresh start. For streams that were split from a previously thermalized stream, about 100 initial trajectories of the new stream were discarded to ensure that the child stream is not correlated with its parent.

4.2.2 $m_\pi \approx 135$ MeV Ensembles

With the installation of the supercomputers Sequoia and Vulcan at the Lawrence Livermore National Laboratory, we are able to extend our study for QCD thermodynamics to lattices with dynamical physical pions. Table 4.8 summarizes the basic input parameters for the lattice ensembles simulated using the Iwasaki + DSDR gauge action and $2 + 1$ Möbius fermion action with space-time volume of $32^3 \times 8$. Such a combination of lattice actions allows a small residual mass and makes the simulation of dynamic physical pions possible.

Similar to the $m_\pi \approx 200$ MeV ensembles, the input quark mass at each temperature is adjusted so that all each ensemble has a pion mass close to its physical value ($m_\pi \approx 135$ MeV).

However, since we had not evolved lattices with Möbius fermions before, we did not have a good estimate for the residual mass at the starting stage of the simulation. We decided to begin our simulations with some tentative choices of input light and strange quark mases. As the simulation took place and statistics were collected, we measured the residual mass at each temperature. Then for some of the ensembles where the deviation between the estimate and measured values is substantial, we tuned the input quark mass accordingly toward the designated value. The initial choices for the parameters and the details of the evolution history for each stream of evolution are listed in Appendix A.

As shown in Table 4.8, there are 9 temperature values under investigation for our $32^3 \times 8$ ensembles with physical pions, each of which contains 2 to 4 streams of evolutions. The temperature range is still between T = 139 MeV and 195 MeV, but an extra T = 154 MeV point in the vicinity of the phase transition has been added as compared to the $m_\pi \approx 200$ MeV ensemble set. Also there is an additional c column in the table that gives the Möbius coefficient c for each ensemble. As discussed in subsection 2.3.4, $(2c+1)L_s$ is the effective L_s that is comparable to a plain DWF ($c = 0$) L_s, which shares the same physical parameters.

To study the finite-volume effects, we extend our study of finite temperature QCD with physical pion mass to a larger $64^3 \times 8$ space-time volume. Table 4.9 summarizes the parameters for the four $64^3 \times 8$ ensembles at $139 \leq T \leq 168$ MeV. The details of each ensemble can also be found in Appendix A.

As most ensembles are composed of more than one evolution stream, we pool together all the thermalized trajectories from various streams with each individual trajectory equally weighted. The ensemble average is calculated from the pool using the jackknife method after binning the results into blocks 50 trajectories to eliminate possible autocorrelations.

#	T (MeV)	β	L_s	c	m_l	m_s	m_{res}	$N_{\text{traj}}^{\text{equil}}$
29	139	1.633	24	1.5	0.00022	0.05960	0.00219(1)	5768
30	149	1.671	16	1.5	0.00034	0.05538	0.00175(1)	7823
31	154	1.689	16	1.5	0.00075	0.05376	0.00120(1)	6108
32	159	1.707	16	1.5	0.00112	0.05230	0.00091(1)	8714
33	164	1.725	16	1.5	0.00120	0.05045	0.00068(1)	7149
34	168	1.740	16	1.2	0.00126	0.04907	0.00057(1)	5840
35	177	1.771	16	1.0	0.00132	0.04614	0.00043(1)	8603
36	186	1.801	16	1.0	0.00133	0.04345	0.00026(1)	10142
37	195	1.829	16	0.9	0.00131	0.04122	0.00019(1)	10140

Table 4.8: Summary of input parameters (β, L_s, c, m_l and m_s) and the measured results for m_{res} for each ensembles with $m_\pi \approx 135$ MeV and with a $32^3 \times 8$ space-time volume. Each is assigned a label in the first column for later reference. The final $N_{\text{traj}}^{\text{equil}}$ column lists the total number of equilibrated trajectories that remain after the imposition of the thermalization and decorrelation cuts described in the text.

#	T (MeV)	β	L_s	c	m_l	m_s	m_{res}	$N_{\text{traj}}^{\text{equil}}$
38	139	1.633	24	1.5	0.00022	0.05960		380
39	149	1.671	16	1.5	0.00034	0.05538		2853
40	159	1.707	16	1.5	0.00112	0.05230		3431
41	168	1.740	16	1.2	0.00126	0.04907		1200

Table 4.9: Summary of input parameters (β, L_s, c, m_l and m_s) and the measured results for m_{res} for each ensembles with $m_\pi \approx 135$ MeV with a $64^3 \times 8$ spece-time volume. Each is assigned a label in the first column for later reference. The final $N_{\text{traj}}^{\text{equil}}$ column lists the total number of equilibrated trajectories that remain after the imposition of the thermalization and decorrelation cuts described in the text.

4.2.3 Verification of the Input Parameters

To verify our choices for the input parameters for the finite temperature ensembles, we generate a zero temperature ensemble with the same setup as the run # 29 at T = 139 MeV with N_τ = 8 replaced by N_τ = 64. Its parameters are listed in Table 4.10. Compared with the finite temperature results, the change in the residual mass is at a remarkable low level (about 1%), indicating a minimum finite volume/temperature effect on the MDWF $m_{\rm res}$. This agreement on the coarsest lattice also establishes the accuracy for $m_{\rm res}$ calculated at other larger β values, since any depenendence of $m_{\rm res}$ on temperature can be viewed as a finite lattice spacing effects.

#	β	N_σ	N_τ	L_s	c	m_l	m_s	$m_{\rm res}$	$N_{\rm traj}^{\rm equil}$
42	1.633	32	64	24	1.5	0.0022	0.05960	0.002167(16)	500

Table 4.10: Summary of input parameters (β, L_s, c, m_l and m_s) and the measured result for $m_{\rm res}$ for the zero temperature ensemble with the similar setup from run # 29.

A variety of measured results in lattice units as well as in physical units is tabulated in Table 4.11 with comparisons to the physicals value from experiment. The lattice spacing a^{-1} and its error are first determined by equating m_Ω from the lattice to the experimental value. Then the masses and the decay constants for the pseudoscalar can be computed in physical units from the lattice results with propagated statistical errors.

Although the measured total light quark mass $\widetilde{m}_l$ = 0.002387(16) (Table 4.10) exceeds our target value $\widetilde{m}_l$ = 0.222 (Table 4.4) by about 7%, the realized pion mass is actually smaller than the physical by about 4% reflecting inaccuracy in our target value for the input quark mass. This error is in line with the deviation for the kaon mass, the decaying constants and $m_{\rm res}$. Moreover, the temperature for β = 1.633 and N_τ = 8 ensemble can be readily determined from a^{-1} to be 136.9(5) MeV, which is only about 1.5% away from the

	a^{-1}	MeV	Expt (MeV)
m_π	0.11824(49)	129.5(1.0)	135
m_K	0.42301(51)	463.4(2.2)	495
m_Ω	1.5267(55)		1672.45
f_π	0.12640(25)	138.5(7)	130.4
f_K	0.14852(48)	162.7(1.1)	156.1
a^{-1}		1095(4)	

Table 4.11: Comparisons of a variety of hadron masses and decay constants between the lattice results (run # 42) and the experimental results. The lattice spacing a^{-1} in the last row is determined from m_Ω value and then the lattice results in physical units listed in the last column is computed.

extrapolated value at 139 MeV[1]. The discrepancies between the values of $1/a$, $m_{\rm res}$ and m_π result from inaccurate values for our choices of β, $\widetilde{m}_l$ and $\widetilde{m}_s$. The differences between our results for f_π and f_K and their experimental values $\sim 5\%$ result from this this miss tuning of $\widetilde{m}_l$ and $\widetilde{m}_s$ as well as finite lattice spacing errors.

4.3 Plaquette

Tables 4.12 and 4.13 show the average plaquette defined as:

$$\langle U_\Box \rangle = \frac{1}{6N_s^3N_t}\sum_x\sum_{\mu,\nu}\mathrm{ReTr}\ P_{\mu\nu}(x)\,, \tag{4.7}$$

for ensembles with pion mass of 200 MeV and 135 MeV respectively.

The difference of the average plaquette value between the different volumes is essentially zero. All the results agree at the 1-σ level or even better. This indicates the effects coming from the volume difference are minimal.

[1]In this work, for consistency we will still adopt 139 MeV as the temperature for the $\beta = 1.633$ and $N_\tau = 8$ ensembles in the following analysis and discussions.

The second row with T = 149 MeV in Table 4.12 come from the ensemble with L_s = 48 while the first from L_s = 32. They show a 0.2% difference in the average plaquette value, as we should expect from the small change in the fermion determinant caused by the increase in L_s from 32 to 48. We also expect that similar small discrepancies could result from our shift of fermion formalisms in the simulation from DWF to MDWF. However, the differences are so small that we can neglect in our study for QCD thermodynamics.

		$16^3 \times 8$		$24^3 \times 8$		$32^3 \times 8$	
T (MeV)	β	#	$\langle U_\Box \rangle$	#	$\langle U_\Box \rangle$	#	$\langle U_\Box \rangle$
139	1.633	8	0.46913(8)			21	0.46898(2)
149	1.671	9	0.48491(3)	16	0.48490(2)	22	0.48488(1)
		10	0.48407(2)				
159	1.707	11	0.49777(4)	17	0.49783(2)	23	0.49785(1)
164	1.725					24	0.50406(1)
168	1.740	12	0.50912(4)	18	0.50909(2)	25	0.50911(1)
177	1.771	13	0.51916(4)	19	0.51916(2)	26	0.51913(1)
186	1.801	14	0.52845(3)	20	0.52840(2)	27	0.52844(1)
195	1.829	15	0.53672(3)			28	0.53674(1)

Table 4.12: Summary of the average plaquette value for the various ensembles with $m_\pi \approx$ 200 MeV. The second row at T = 149 MeV is for the L_s = 48 ensemble.

Fig. 4.3 displays a comparison of the average plaquette among different temperatures and ensembles. It is transparent that the plaquettes for different volumes and input quark masses agree very well.

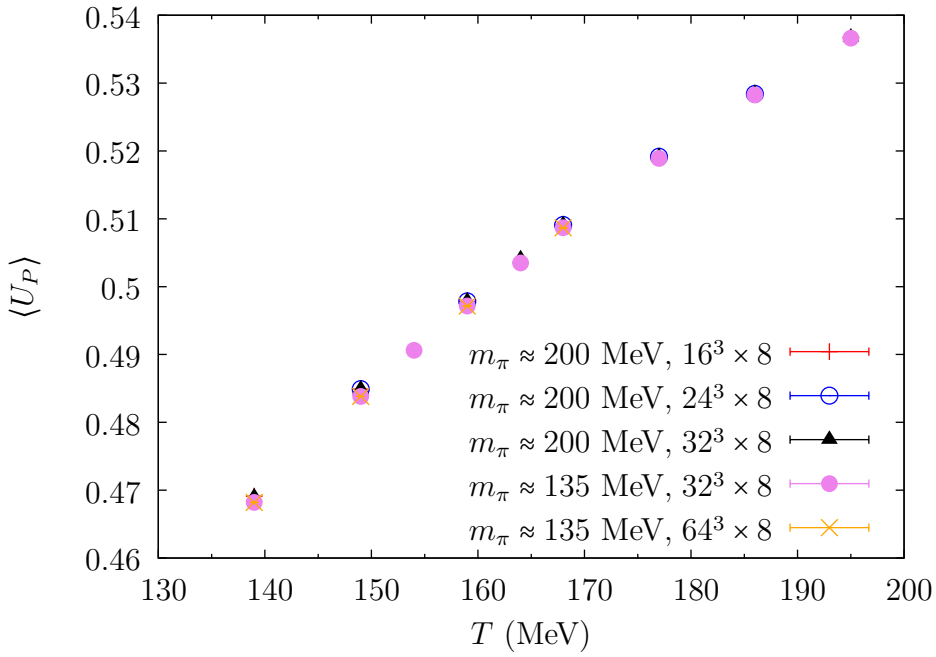

Figure 4.3: Plot of the average plaquette for ensembles with different volumes and pion masses.

		$32^3 \times 8$		$64^3 \times 8$	
T (MeV)	β	#	$\langle U_\square \rangle$	#	$\langle U_\square \rangle$
139	1.633	29	0.468194(11)	38	0.46819(2)
149	1.671	30	0.483823(9)	39	0.483824(5)
154	1.689	31	0.490621(9)		
159	1.707	32	0.497145(8)	40	0.497150(3)
164	1.725	33	0.503497(8)		
168	1.740	34	0.508667(9)	41	0.508676(8)
177	1.771	35	0.518892(6)		
186	1.801	36	0.528245(6)		
195	1.829	37	0.536612(6)		

Table 4.13: Summary of the average plaquette value for the various ensembles with $m_\pi \approx$ 135 MeV.

4.4 Residual Mass

4.4.1 Measuring Residual Mass

Recall the PCAC relation for DWF in Eq. (2.39)

$$\Delta_\mu A_\mu^b(x) = 2m_f J_5^b(x) + 2J_{5q}^a(x).$$

Assuming the midpoint contribution can be similarly described as an ordinary mass term in the Symanzik effective theory [114] (leading low-energy contributions at large L_s and small lattice spacing)

$$\mathcal{L}_{\text{eff}} = \mathcal{L}_{\text{QCD}}(m_f = 0) + (m_f + m_{\text{res}})\overline{q}q \ , \tag{4.8}$$

it should behave at low energies in the same way as $J_5(x)$ with a coefficient, which is proportional to m_{res} as one would expect, *i.e.*

$$J_{5q}^b = m_{\text{res}} J_5^b = m_{\text{res}} \overline{q}\gamma_5 \tau^b q \ . \tag{4.9}$$

Thus we can calculate the residual mass from the ratio [115, 116, 114, 117]:

$$R(t) = \frac{\left\langle \sum_{\vec{x}} J^b_{5q}(\vec{x},t)\pi^b(0)\right\rangle}{\left\langle \sum_{\vec{x}} J^b_{5}(\vec{x},t)\pi^b(0)\right\rangle}, \tag{4.10}$$

where no summations over b are implied. Here π^b can be any pion interpolating operator. In our practical computation, it is chosen to be J^b_5. At a sufficiently large time separation t where the low-energy physics dominates, J_{5q} should have the form given in Eq. (4.9), and $R(t)$ should show a plateau at the value of m_{res}. In numerical calculation, m_{res} is obtained from the average value of $R(t)$ over points in the plateau.

For finite temperature ensembles, a ratio $R(x)$ of spatially separated correlation functions is used instead of the temporal separated ones in Eq. (4.10).

4.4.2 Residual Mass Tuning

Enforcing a line of constant physics for DWF simulations often requires some fine tuning of the input quark masses as the residual masses for most of the planned ensembles are not known beforehand. It is thus extremely beneficial to determine the dependence of m_{res} on different variables such as L_s, β, the Möbius coefficient c, *etc.*. In the rest of this section, we will discuss our studies of such dependence and how they provided crucial guidelines that helped us in determining the parameters for the MDWF simulations with physical pions.

Dependence of m_{res} on L_s

The extent of the fictitious fifth dimension has an significant impact on the magnitude of the residual chiral symmetry breaking of DWF, signaled by the additive mass renormalization m_{res}. There exists an expression for the dependence of m_{res} on L_s given in Eq. (2.45), and rewritten below in a simplified form,

$$m_{\text{res}} = a\frac{e^{-\lambda L_s}}{L_s} + b\frac{1}{L_s}, \tag{4.11}$$

where a, b and λ are the three parameters to be fitted.

While an explicit check for the validity of the form in Eq. (4.11) with dynamical fermions requires a set of ensembles of different L_s and is thus fairly expensive, a partially quenched calculation is quite accessible. In order to determine the minimum L_s that is compatible with a physical pion mass for Shamir DWF formulation, we performed several partially quenched calculation on a selected set of $16^3 \times 8$ ensembles.

The results are presented in Fig. 4.4. Each panel displays a fit result for the form of Eq. (4.11) at a given temperature. The label of the dynamic ensemble and the input valence quark mass is given in the legend. Given the fitted parameters and χ^2/dof shown in the plots, Eq. (4.11) does indeed give a accurate description for the residual mass for a given value of β.

The target value of the total light quark mass proposed in Table 4.4 is also marked in the plots as a black dotted line. It is worth noting that the minimum L_s required for a zero input quark mass is about 40 at T = 159 MeV and about 60 T = 149 MeV. Naturally, at T = 139 MeV, which is absent from this study, the minimum L_s would be even larger. These constraints can of course be loosed slightly if we adopt a negative input quark mass but it will not exempt us completely from the burden of a large L_s. Therefore it motivated us to shift from plain DWF to the MDWF formalism to reduce the extent of the fifth dimension significantly, especially for the ensembles below the pseudo-critical temperature.

$m_{\mathbf{res}}$ Dependence on Möbius Coefficient c

In Möbius construction, when L_s is sufficiently large and c is not too large, ensembles with fixed $(b + c)L_s$ are related by the equivalence relation presented in 2.3.4 and hence should give the same residual mass. To verify the equivalence, we generated a dynamical MDWF evolution whose setup is identical to the T = 149 MeV, L_s = 48 ensemble (run # 10) except that L_s = 18, c = 0.832 (we label it as run # **??**) [57] and collected 950 thermalized

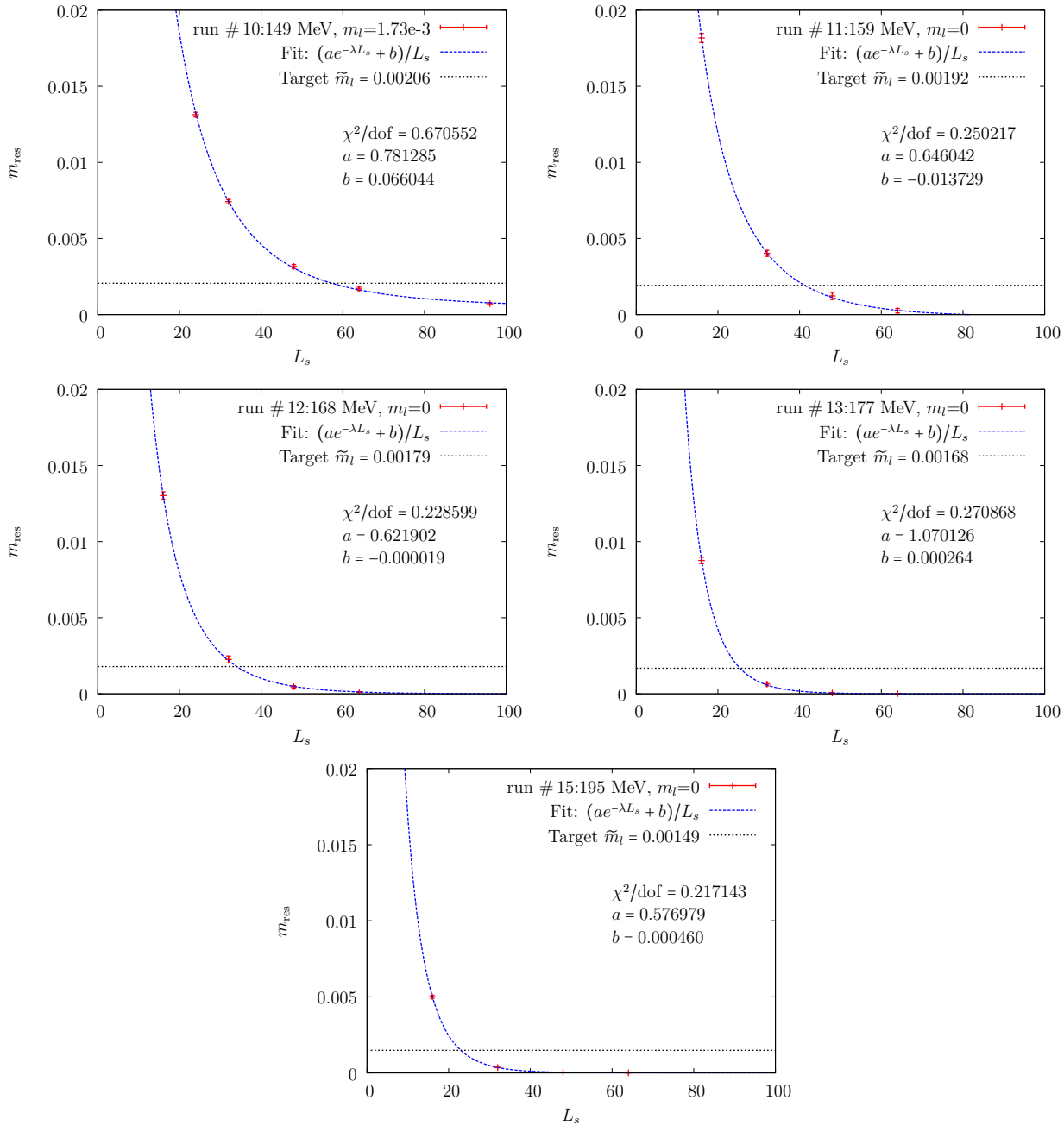

Figure 4.4: L_s dependence of $m_{\rm res}$ for partially quenched, $16^3 \times 8$ ensembles measured on every 10 trajectory after thermalization using a point source and correlation function studied with increasing separations along the x direction. The corresponding run number and valence quark mass is shown in the legend. The fitted parameters and χ^2/dof for the form in Eq. (4.11) are also shown. The target total quark mass that corresponds to a physical pion is marked with a dotted horizontal black line.

trajectories. Again, we performed a partially quenched calculation with various L_s and compared it with the results from run # 10, which is shown in Fig. 4.5. After we normalize

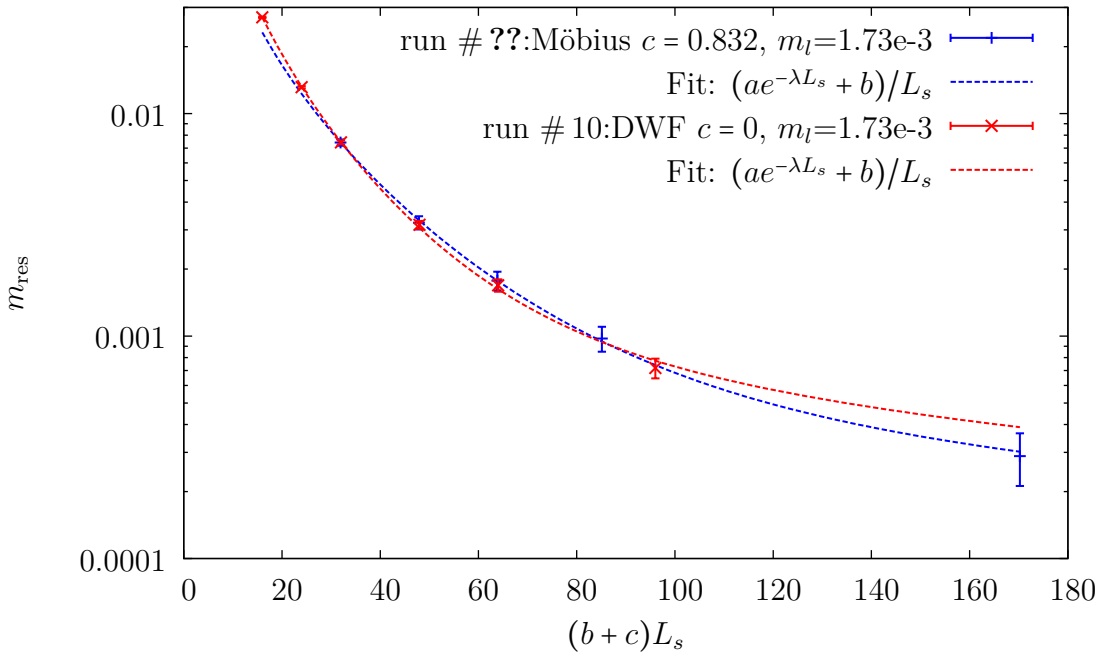

Figure 4.5: Comparison of $m_{\rm res}$ using a normalized $(b + c)L_s$ for two sets of ensembles with otherwise identical parameters except L_s and c. A logarithm scale is used on the y axis.

the effective fifth dimension to be $(b + c)L_s$, the equivalence of fixed $(b + c)Ls$ MDWF with respect to $m_{\rm res}$ is remarkable as the two fitted lines lie almost on top of each other for the region $L_s \leq 100$.

This equivalence allows us to estimate $m_{\rm res}$ for MDWF based on results from DWF simulations. As we have explained in Section 2.3.4, when the Möbius coefficient c passes a certain threshold, there is a dramtic slowing down in the HMC evolution which overwhelms the benefits obtained from a smaller L_s. The threshold for c is often located around the point where $m_{\rm res}$ is minimized for a fixed L_s. Hence we need to determine the combinations of c and L_s that will minimize the overall computational cost.

To this end, we performed another series of valence calculation with different c on the

$16^3 \times 8$ DWF ensembles. Fig. 4.6 shows the results at $T = 139$ MeV for three different L_s. Obviously, $L_s = 16$ MDWF cannot reduce $m_{\rm res}$ to be lower than the target $\widetilde{m}_l$ with any choice of c. $L_s = 20$ can narrowly meet the requirement, but the Möbius coefficient could be too close to the "critical slowing down" region. Therefore, we decided to adopt $L_s = 24$ and $c = 1.5$ in our practical simulation.

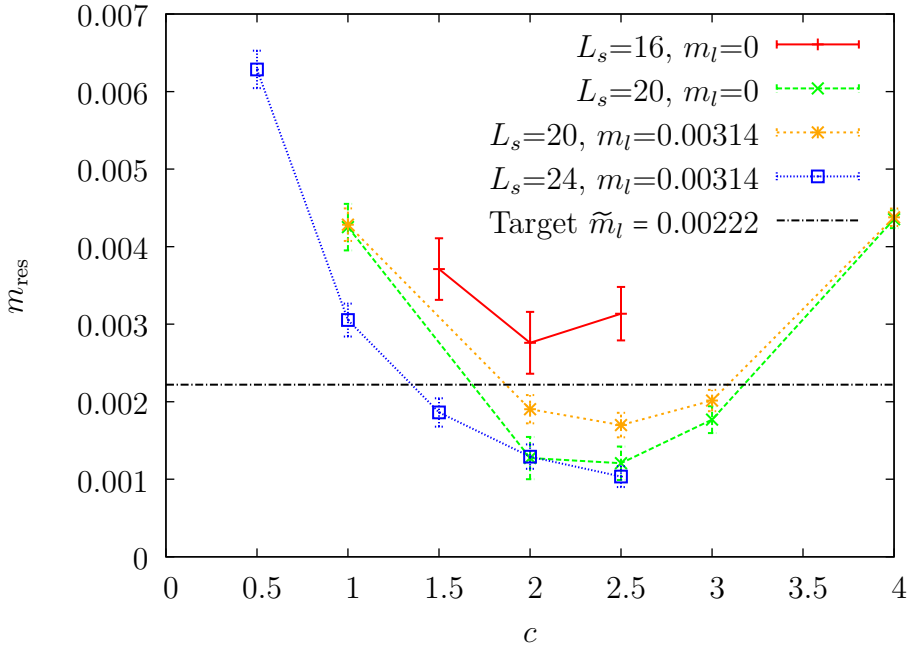

Figure 4.6: $m_{\rm res}$ measured from a partially quenched calculation at $T = 139$ MeV (run # 8) with $L_s = 16$, 20 and 24 and two valence quark masses. Target $\widetilde{m}$ that corresponds to a physical pion is marked as a horizontal black line.

On the other hand, $L_s = 16$ is large enough to satisfy the constraint imposed by $\widetilde{m}_l$ for all the other temperatures. The results for the partially quenched calculation with $L_s = 16$ is shown in Fig. 4.7.

All these studies set a starting point for our choice of the input parameters of the MDWF thermodynamics simulation with physical pions. One should keep in mind that they are based on the partially quenched results and there is an appreciable dependence of $m_{\rm res}$ on the

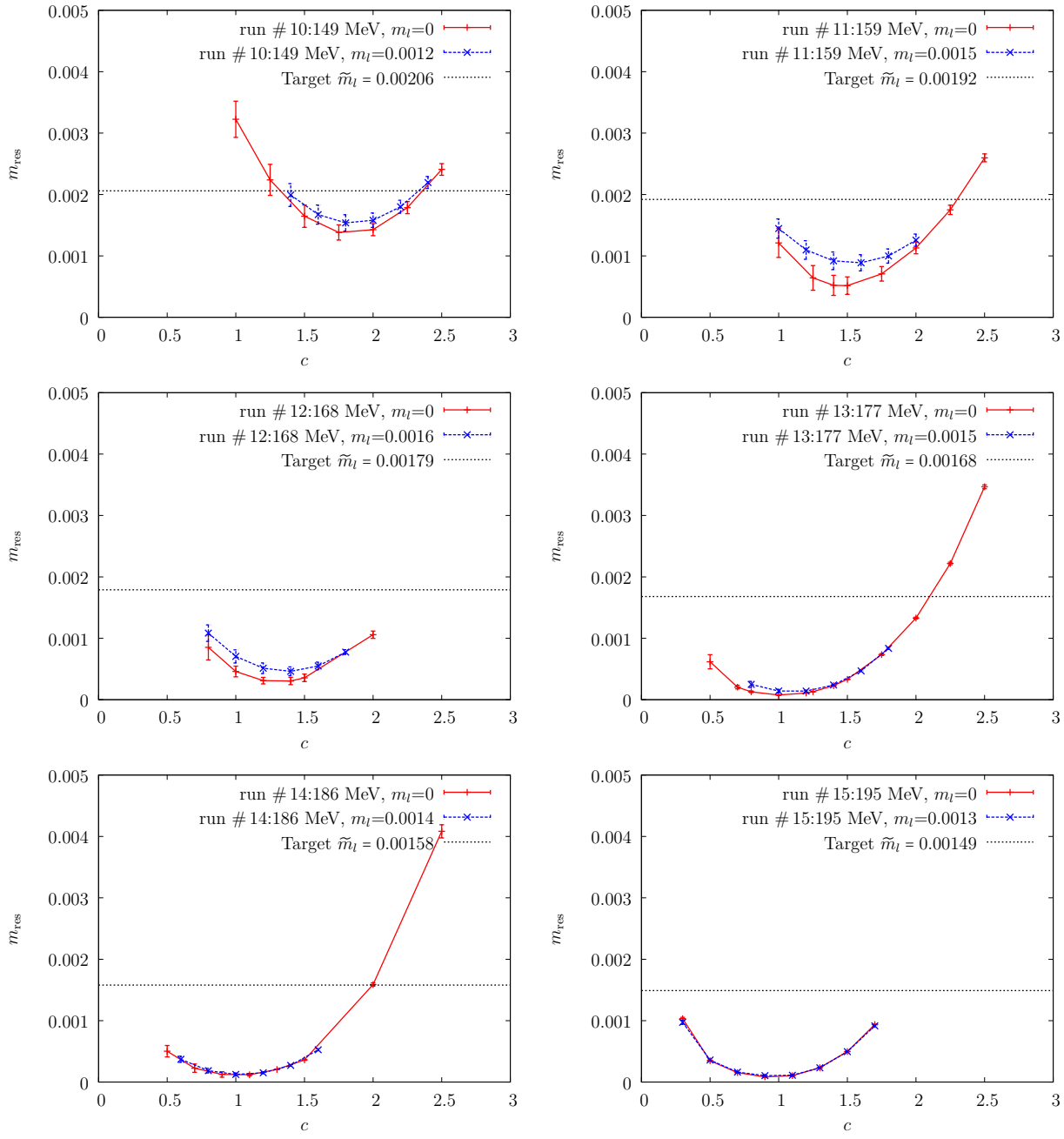

Figure 4.7: $m_{\rm res}$ measured from a partially quenched calculation at 149 MeV$\leq T \leq$ 195MeV with L_s = 16 two valence quark masses. Target $\widetilde{m}$ that corresponds to a physical pion is marked by a horizontal black line.

input quark mass. Moreover, the parameter determining studies from the zero-temperature ensemble contains errors as well. Therefore, the input quark masses we adopt in Table A.3 and 4.8 are by no means precise values that correspond to a line of constant physics with a physical pion and kaon. However, with careful adjustments during the evolution, we are able to stay close to the line of constant physics with an error less than 5%.

Chapter 5

Chiral Symmetry with Correlation Functions

In this Chapter we will discuss Green's functions constructed from the eight scalar and pseudoscalar operators: $\overline{\psi}_l\psi_l$, $\overline{\psi}_l\tau^i\psi_l$, $\overline{\psi}_l\gamma^5\psi_l$, $\overline{\psi}_l\tau^i\gamma^5\psi_l$. Here ψ_l is a doublet of up and down quark fields and $\{\tau_i\}_{1\leq i\leq 3}$ the usual Pauli matrices. These operators are related by the $SU(2)_L \times SU(2)_R$ chiral symmetry of QCD and the anomalously broken $U(1)_A$ symmetry. In Sec. 5.1 we review the relations among these eight operators and their Green's functions implied by the $SU(2)_L \times SU(2)_R$ and $U(1)_A$ symmetries, paying particular attention to the degree to which these relations should hold at finite lattice spacing for the DWF formulation.

In Sec. 5.2 we present our numerical results, focusing on those relations implied by $SU(2)_L \times SU(2)_R$ chiral symmetry and examining their dependence on temperature. Some empirical fittings for $\chi_{\rm disc}$ are then discussed in order to locate the pseudo-critical temperature. In the final section, Sec. 5.3, we examine the relations implied by $U(1)_A$ symmetry, including evidence for non-zero anomalous, $U(1)_A$ symmetry breaking above the pseudo-critical temperature T_c, a non-vanishing asymmetry which disappears rapidly as the temperature increases above T_c.

The numerical results from $m_\pi \approx 200$ MeV ensembles discussed in this Chapter are complete, while those from $m_\pi \approx 135$ MeV ensembles are preliminary. The connected susceptibilities at volume $64^3 \times 8$ have not yet been measured at the time when this thesis is composed.

5.1 Preliminaries

In this section, we present a brief review of a variety of chiral observables and the relations among them implied by the $SU(2)_L \times SU(2)_R$ and $U(1)_A$ symmetries as illustrated in Fig. 5.1. A detailed description can also be found in Ref. [35].

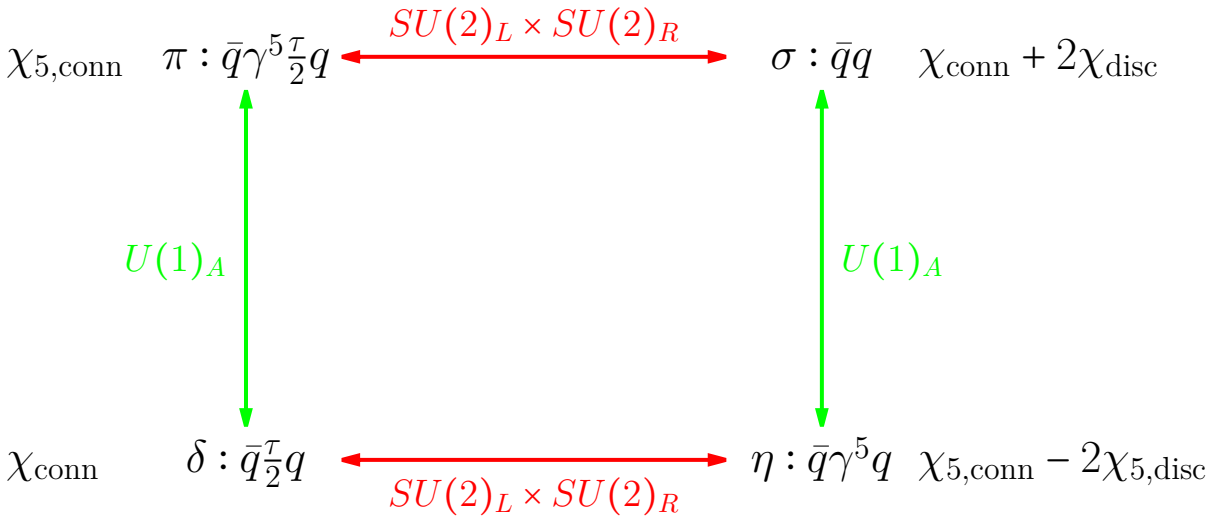

Figure 5.1: A graphical presentation for the symmetry transformations that relate the scalar and pseudoscalar mesons in flavor singlet and flavor non-singlet channels.

The standard order parameter for the chiral phase transition is the single-flavor, light-

quark chiral condensate,

$$\Sigma_l \equiv -\frac{1}{2}\left\langle \overline{\psi}_l \psi_l \right\rangle \tag{5.1}$$

$$= \frac{1}{2}\frac{T}{V}\frac{\partial \ln Z}{\partial m_l} \tag{5.2}$$

$$= \frac{1}{N_\sigma^3 N_\tau}\left\langle \mathrm{Tr} M_l^{-1} \right\rangle, \tag{5.3}$$

where M_l is the single-flavor, light-quark Dirac matrix and the brackets $\langle \ldots \rangle$ in the bottom equation indicate an average over gauge fields. However, this quantity contains an ultraviolet divergent contribution that is proportional to m_q/a^2 for the case of a lattice regularization. In order to remove this ultraviolet divergence, it is standard to introduce a subtracted chiral condensate constructed from a weighted difference between the chiral condensates of the light and strange quarks [118]:

$$\Delta_{l,s} = \Sigma_l - \frac{\widetilde{m}_l}{\widetilde{m}_s}\Sigma_s. \tag{5.4}$$

Here Σ_s is defined using the strange quark Dirac matrix in a manner analogous to Eq. (5.3). For domain wall fermions there is a further difficulty associated with the short distance contributions to Σ_q and the subtracted quantity $\Delta_{l,s}$. For a finite fifth dimensional extent, $L_s < \infty$, the DWF chiral symmetry is only approximate and residual chirally symmetry breaking effects appear. The largest such effect is a small additive shift in the quark mass: the residual mass m_{res} mentioned in Chap. 2. Similar residual chiral breaking will appear in Σ_q and will be of order m_{res}/a^2 if we express m_{res} in physical units. However, since the detailed mechanism which generates the residual mass is not directly related to that which introduces the additive constant into Σ_q, the subtraction coefficient α that would be needed to remove both the m_q/a^2 and the $O(m_{\mathrm{res}}/a^2)$ terms in $\Sigma_l - \alpha\Sigma_s$ is not known.

Thus, the subtracted quantity $\Delta_{l,s}$ defined in Eq. (5.4) will contain an unphysical, $O(m_{\mathrm{res}}/a^2)$ constant which will decrease the utility of $\Delta_{l,s}$ computed in a DWF simulation. In particular, we cannot compare $\Delta_{l,s}$ with the same difference of chiral condensates obtained from other lattice fermion formulations. While this added unphysical constant does

not depend on temperature, it does depend strongly on the gauge coupling g so the usual procedure of varying the temperature by varying g at fixed N_τ will induce an apparent temperature dependence in this unphysical contribution to $\Delta_{l,s}$. However, the definition of $\Delta_{l,s}$ given in Eq. (5.4) (which differs from that used in the earlier paper [35]) does have a useful property. As will be discussed in Chap. 6, this subtraction using for α the physical quark mass ratio, $\alpha = \widetilde{m}_l/\widetilde{m}_s$ will lead to a more convergent spectral expression for $\Delta_{l,s}$.

Results for the quantities Σ_l, Σ_s and $\Delta_{l,s}$ are given in Tables 5.3 and 5.4. For each configuration used in the calculation, the volume-averaged, chiral condensate is computed from the right hand side of Eq. (5.3), using 10 Gaussian random volume sources to estimate the trace. In the later part of this introductory section, we will use the Gell-Mann-Oakes-Renner (GMOR) relation to define an improved, subtracted chiral condensate $\widetilde{\Delta}_{l,s}$, which contains a much smaller unknown correction and can be compared with the results from other formulations of lattice fermions.

The chiral condensate Σ_l and the various subtracted versions discussed above can be used to explore the vacuum breaking of $SU(2)_L \times SU(2)_R$ and $U(1)_A$ symmetry and their restoration (or partial restoration) as the temperature is increased. However, much more information can be obtained from the susceptibilities defined as integrated correlation functions of the eight local operators,

$$\sigma = \overline{\psi}_l \psi_l \tag{5.5}$$

$$\delta^i = \overline{\psi}_l \tau^i \psi_l \tag{5.6}$$

$$\eta = i\overline{\psi}_l \gamma_5 \psi_l \tag{5.7}$$

$$\pi^i = i\overline{\psi}_l \tau^i \gamma_5 \psi_l. \tag{5.8}$$

Such susceptibilities are both much more sensitive to the transition from the ordered to the disordered state and also allow independent measures of $SU(2)_L \times SU(2)_R$ and $U(1)_A$ symmetry breaking. The operator quadruplets (σ, π^i) and (η, δ^i) each transform as an irreducible 4-dimensional representation of $SU(2)_L \times SU(2)_R$. The four pairs, (σ, η), $(\delta^i, \pi^i)_{1 \le i \le 3}$ each

transform under the simple, two-dimensional representation of $U(1)_A$. We then identify the four distinct susceptibilities which are allowed by isospin symmetry:

$$\chi_\sigma = \frac{1}{2}\int \mathrm{d}^4x \left\langle \sigma(x)\sigma(0)\right\rangle \tag{5.9}$$

$$\chi_\delta = \frac{1}{2}\int \mathrm{d}^4x \left\langle \delta^i(x)\delta^i(0)\right\rangle \tag{5.10}$$

$$\chi_\eta = \frac{1}{2}\int \mathrm{d}^4x \left\langle \eta(x)\eta(0)\right\rangle \tag{5.11}$$

$$\chi_\pi = \frac{1}{2}\int \mathrm{d}^4x \left\langle \pi^i(x)\pi^i(0)\right\rangle \tag{5.12}$$

where the factor 1/2 has been introduced so that these correspond to the single flavor quantities that are typically computed using lattice methods and no sum over the repeated index i is intended. In light of the multiplet structure defined above, the following relations are implied by $SU(2)_L \times SU(2)_R$ and $U(1)_A$ symmetry (*c.f.* 5.1):

$$\left.\begin{aligned}\chi_\sigma &= \chi_\pi \\ \chi_\eta &= \chi_\delta\end{aligned}\right\} \qquad SU(2)_L \times SU(2)_R, \tag{5.13}$$

$$\left.\begin{aligned}\chi_\sigma &= \chi_\eta \\ \chi_\pi &= \chi_\delta\end{aligned}\right\} \qquad U(1)_A. \tag{5.14}$$

These susceptibilities can be written in terms of the Dirac operator M_l. For the correlators of the operators π^i and δ^i, which introduce non-zero isospin, only connected combinations appear:

$$\chi_\pi = \frac{1}{N_\sigma^3 N_\tau}\mathrm{Tr}\left\langle \gamma_5 M_l^{-1}\gamma_5 M_l^{-1}\right\rangle \tag{5.15}$$

$$\chi_\delta = -\frac{1}{N_\sigma^3 N_\tau}\mathrm{Tr}\left\langle M_l^{-1} M_l^{-1}\right\rangle \tag{5.16}$$

where the notation "Tr" indicates a trace over spinor and color indices as well as the space-time volume. The σ and η susceptibilities are a combination of the connected parts which appear in χ_δ and χ_π respectively and a disconnected part:

$$\chi_\sigma = \chi_\delta + 2\chi_{\mathrm{disc}} \tag{5.17}$$

$$\chi_\eta = \chi_\pi - 2\chi_{5,\mathrm{disc}} \tag{5.18}$$

where the disconnected parts $\chi_{\rm disc}$ and $\chi_{5,\rm disc}$ are given by

$$\chi_{\rm disc} = \frac{1}{N_\sigma^3 N_\tau}\left\{\left\langle\left(\mathrm{Tr}M_l^{-1}\right)^2\right\rangle - \left(\left\langle\mathrm{Tr}M_l^{-1}\right\rangle\right)^2\right\} \tag{5.19}$$

$$\chi_{5,\rm disc} = \frac{1}{N_\sigma^3 N_\tau}\left\langle\left(\mathrm{Tr}M_l^{-1}\gamma_5\right)^2\right\rangle. \tag{5.20}$$

As is conventional, we have removed the truly disconnected piece $2N_s^3N_\tau\Sigma_l^2$ from the expression for χ_σ given in Eq. (5.17). This extra term would appear if the right hand side of the definition given by Eq. (5.9) where completely evaluated. The factor of two that appears in Eqs. (5.17) and (5.18) was mistakenly omitted from the published version of Ref. [35] and arises when these relations are written in terms of single flavor quantities. The signs of $\chi_{\rm disc}$ and $\chi_{5,\rm disc}$ have been chosen so that each is positive.

We can combine Eqs. (5.13), (5.17) and (5.18) to obtain relations between the $U(1)_A$ symmetry breaking difference $\chi_\pi - \chi_\delta$ and $\chi_{\rm disc}$ and $\chi_{5,\rm disc}$ if $SU(2)_L \times SU(2)_R$ symmetry is assumed:

$$\chi_\pi - \chi_\delta = (\chi_\pi - \chi_\sigma) + (\chi_\sigma - \chi_\delta) \tag{5.21}$$

$$= 2\chi_{\rm disc} \tag{5.22}$$

$$= 2\chi_{5,\rm disc} \tag{5.23}$$

where the second equation is true if the $SU(2)_L \times SU(2)_R$ relation $\chi_\pi = \chi_\sigma$ of Eq. (5.13) is valid while the third is obtained by a similar manipulation and the second $SU(2)_L \times SU(2)_R$ relation $\chi_\delta = \chi_\eta$.

The connected Green's functions can be computed from the lattice by integrating the two-point correlators from a point source over the whole volume. This method was used for the calculations on the $16^3 \times 8$ and $24^3 \times 8$ ensembles with $m_\pi \approx 200$ MeV. On the $32^3 \times 8$ ensembles with either pion mass we achieved a reduced statistical error by using instead a random Z_2 wall source. The disconnected parts are calculated by averaging products of chiral condensates where the stochastic evaluation of the trace appearing in each factor is obtained from different stochastic sources.

The $SU(2)_L \times SU(2)_R$ relations given in Eqs. (5.13) should be valid in the continuum for $T > T_c$ when $SU(2)_L \times SU(2)_R$ becomes an accurate symmetry. They should also be true when $T > T_c$ in a lattice formulation which preserves chiral symmetry. However, for our DWF formulation we should expect deviations arising from residual chiral symmetry breaking. For low energy quantities, $m_{\rm res}$ should provide a good measure of this residual chiral symmetry breaking, with effects that are well described as arising simply from the total bare quark mass $\widetilde{m}_l = m_l + m_{\rm res}$.

However, the four susceptibilities being discussed are not simple long-distance quantities since the space-time integrals that appear in their definitions include points where the two local operators collide. In fact, the connected parts of the susceptibilities contain quadratic divergences while the disconnected parts diverge logarithmically. The presence of quadratic divergences in the connected susceptibilities, *e.g.* χ_π and χ_δ, can be easily deduced from the Wilson operator product expansion and dimensional arguments. The product of two dimension-three fermion bilinears separated by a space-time distance x should contain a constant behaving as $1/x^6$ as $x \to 0$. When integrated over space-time to form the susceptibility, this $1/x^6$ term will give a quadratic divergence. For the disconnected parts of the susceptibilities, a similar dimensional argument applies. However, the disconnected parts are constructed from the product of two independent fermion loops, each evaluated as a separate trace. For the case of scalar or pseudoscalar susceptibilities, chiral symmetry requires that each trace be proportional to m_l so the product will behave as m_l^2/x^4 leading to a logarithmic divergence multiplied by the very small factor m_l^2. Thus, if the continuum regulator respects chiral symmetry, then the $SU(2)_L \times SU(2)_R$ and $U(1)_A$ breaking differences $\chi_\pi - \chi_\sigma$, $\chi_\delta - \chi_\eta$, $\chi_\pi - \chi_\delta$ and $\chi_\eta - \chi_\sigma$ will all contain only small, logarithmic singularities proportional to $m_l^2 \ln(m_l/\Lambda)$ if evaluated order-by-order in QCD perturbation theory, where Λ is the continuum cutoff scale.

In our lattice-regulated domain wall theory, the residual chiral symmetry breaking will

result in these same differences containing small unphysical pieces of order $m_{\rm res}^2$. As in the case of the chiral condensate, $m_{\rm res}$ does not literally enter these differences but instead we expect that $m_{\rm res}^2$ will provide a reasonable estimate of their size. Note, when expressed in physical units $m_{\rm res} \sim e^{-\alpha L_s}/a$ so that our estimate $m_{\rm res}^2 \sim e^{-2\alpha L_s}/a^2$ of a chiral symmetry breaking difference remains quadratically divergent but is suppressed by the same factor that makes $m_{\rm res}^2$ small. (Here, for simplicity, we assume that the residual chiral symmetry breaking effects fall exponentially with increasing L_s, with an exponent α, unrelated to the α used earlier in this Section.) For the purposes of this paper $m_{\rm res}^2 \sim (10\ {\rm MeV})^2$, a quantity that is negligible on the $(\Lambda_{\rm QCD})^2 \approx (300\ {\rm MeV})^2$ scale of the physical parts of the susceptibilities being subtracted.

Finally we examine two additional identities that hold in the continuum limit. The first is the relation between $\chi_{5,\rm disc}$ and the topological susceptibility $\chi_{\rm top}$. This relation begins with the identity

$$Q_{\rm top} = m_l^c \,{\rm Tr}\left\{\gamma_5 \frac{1}{M_l}\right\} \tag{5.24}$$

which for the continuum theory will hold for each gauge configuration. Here for clarity we have introduced the quantity m_l^c to represent the light quark mass in the continuum theory. This is easily understood by using a sum over Dirac operator eigenvectors to evaluate the trace and recognizing that the result is simply the number of right- minus the number of left-handed zero modes [119] which is equal to $Q_{\rm top}$ by the Atiyah-Singer theorem. Recall that

$$Q_{\rm top} = \frac{g^2}{32\pi^2} \int {\rm d}^4x F^a_{\mu\nu}(x) \widetilde{F}^a_{\mu\nu}(x). \tag{5.25}$$

Here $\widetilde{F}_{\mu\nu} = \frac{1}{2}\sum_{\rho\sigma} \epsilon_{\mu\nu\rho\sigma} F_{\rho\sigma}$ where $\epsilon_{\mu\nu\rho\sigma}$ is the usual anti-symmetric Levi-Civita tensor with $\epsilon_{1234} = 1$.

The desired identity:

$$\chi_{\rm top} = (m_l^c)^2 \chi_{5,\rm disc} \tag{5.26}$$

is simply the ensemble average of the square of Eq. (5.24). This continuum equation should

also relate DWF lattice quantities provided the total bare quark mass $\widetilde{m}$ is used in place of the continuum mass m_l^c. As was explored at length in Ref. [35], this relation is badly violated for our lattice calculation because at our relatively coarse lattice spacing the quantity $Q_{\rm top}$ is difficult to compute directly. The right hand side of Eq. (5.26) appears to nicely define the topological susceptibility giving the same answer even when the light quark quantity $\widetilde{m}_l^2\chi_{5,\rm disc}$ is replaced with the corresponding strange quark quantity or the product of strange and light quark expressions. (Note the right hand side of Eq. (5.24) is expected to give the same result on a given gauge configuration independent of the quark mass.) For completeness $\chi_{5,\rm disc}/T^2$ and $\chi_{\rm top}/(\widetilde{m}_l T_c)^2$ are tabulated in the two right-most columns of Table 5.3, where $\chi_{\rm top}$ is computed using the procedure described in Ref. [35]. As can be seen in Table 5.3, their disagreement is substantial. However, the fractional discrepancy does decrease with increasing temperature (and decreasingly lattice spacing) as should be expected if this is a finite lattice spacing artifact. We will not make further use of $\chi_{\rm top}$.

The second identity is the usual Ward identity connecting χ_π and the chiral condensate. This can be derived in the continuum for non-zero quark mass by evaluating the following integrated divergence:

$$0 = \int \mathrm{d}^4x \partial_\mu \left\langle 0|T\left(A^{a\mu}(x)\pi^b(0)\right)|0\right\rangle \tag{5.27}$$

$$= \int \mathrm{d}^4x \left\langle 0|T\left(-2m_l^c i\pi^a(x)\pi^b(0)\right)|0\right\rangle - 2i\left\langle 0|\sigma(0)|0\right\rangle \delta^{ab} \tag{5.28}$$

where a and b are isospin indices. Here the left term in the second line comes from the divergence of the axial current, $\partial_\mu A(x)^{a\mu}$, while the right term results from the equal-time commutator that arises when the partial derivative with respect to the time is brought inside the time-ordered product. The result is the Gell-Mann-Oakes-Renner relation [113]:

$$m_l^c\chi_\pi = \Sigma_l. \tag{5.29}$$

While this relation should be true in a continuum theory which has been regulated in a chirally symmetric way, both the right- and left-hand sides of Eq. (5.29) contain quadratic

divergences as discussed earlier. Thus, we should not expect this equation to be obeyed in our DWF theory unless we take the limit of infinite L_s at finite a so that our theory has an exact chiral symmetry.

However, this equation has two important uses. First, we can repeat its derivation in our lattice theory using the partially conserved, 5-dimensional axial current $\mathcal{A}^{a\mu}$ constructed by Furman and Shamir [38] and the divergence equation obeyed by $\mathcal{A}^{a\mu}$:

$$\partial_\mu \mathcal{A}^{a\mu} = -2im_l\pi^a + 2J^a_{5q} \tag{5.30}$$

which has also been discussed in Eq. (2.39) in Chap. 2. When used in the above derivation this relation yields the lattice identity:

$$2m_l\chi_\pi + \int \mathrm{d}^4x \, \langle 0|T\left(iJ_{5q}(x)^a\pi^a(0)\right)\rangle = 2\Sigma_l \tag{5.31}$$

for $a = 1$, 2 and 3. In the usual application of Eq. (5.30), iJ^a_{5q} is replaced in Eq. (5.31) by $m_{\mathrm{res}}\pi^a$ which would provide a DWF derivation of Eq. (5.29) in which the continuum light quark mass m_l^c is replaced by $\widetilde{m}_l = m_l + m_{\mathrm{res}}$. However, the low-energy relation $iJ^a_{5q} \approx m_{\mathrm{res}}\pi^a$ cannot be used here because short-distances are involved. Nevertheless, we can simply evaluate both sides of Eq. (5.31) in our lattice calculation as a check of this discussion and find agreement within errors. Our numerical results for the three quantities which appear in Eq. (5.31) are tabulated in Tables 5.1, 5.2, 5.3, and 5.4 as well as the right- and left-hand sides of Eq. (5.31) after a common factor of 2 has been removed.

We also plot in Fig. 5.2 both the left- and right-hand sides of Eq. (5.31) as well $\widetilde{m}_q\chi^q_\pi$ ($q = l, s$), as the result of the naive use of the low-energy relation $iJ^a_{5q} \approx m_{\mathrm{res}}\pi^a$. The left panel of Fig. 5.2 shows these quantities for the light-quark case discussed here while the right panel shows the same quantities computed using the strange quark. In Tables 5.1 and 5.2 and Fig. 5.2, the mixed susceptibility appearing in Eq. (5.31) is represented by Δ^q_{mp}:

$$\Delta^q_{\mathrm{mp}} = \int \mathrm{d}^4x \left\langle 0|T\left(iJ^{(q)}_{5q}(x)\pi^{(q)}(0)\right)\right\rangle. \tag{5.32}$$

where in this equation we construct the quark bilinears $J_{5q}^{(q)}$ and $\pi^{(q)}$ from a single flavor of quark specified by $q = l$ or s and include only connected graphs, in which the quark fields are contracted between J_{5q} and π.

In these tables and figures and those which follow, when a combination of quantities that were computed separately are combined, such as $m_l \chi_\pi^l + \Delta_{\rm mp}^l$ we will use the jackknife method to compute the error on the combined quantity so that the effects of statistical correlations between the quantities being combined are included. However, for simplicity, if a computed renormalization factor, factor of a expressed in physical units or factor of $m_{\rm res}$ appears, these factors usually have smaller errors than the quantities they multiply and their fluctuations will be ignored.

The top panel of Fig. 5.2 clearly reveal the perfect agreement between Σ_q and $m_q \chi_\pi^q + \Delta_{\rm mp}^l$ for both light and strange quarks as enforced exactly by the DWF Ward identity. The finite discrepancy between $\widetilde{m}_q \chi_\pi^q$ and the two quantities above implies short-distance effects that cannot be represented by an additive $m_{\rm res}$. As expected, the discrepancy is most pronounced at the lowest temperature where the residual chiral symmetry breaking is the most significant. Since a similar Ward identity holds for Möbius fermions, similar patterns also exist in the lower panel of Fig. 5.2 in which the results from the $m_\pi \approx 135$ MeV are presented. Furthermore, the reduced residual chiral symmetry breaking for these Möbius ensembles is also reflected in the much suppressed short-distance effects, signaled by the narrowed or even closed gap between $\Sigma_q / m_q \chi_\pi^q + \Delta_{\rm mp}^l$ and $\widetilde{m}_q \chi_\pi^q$.

A second use of Eq. (5.29) is to provide a method to compute a more physical result for $\Delta_{l,s}$ in a DWF calculation. Since no chiral limit has been taken in the continuum derivation of Eq. (5.29), it will hold equally well if applied to either strange or light quarks. If we use the resulting equations for Σ_l and Σ_s to determine the weighted difference $\Delta_{l,s}$ we obtain:

$$\Delta_{l,s} = m_l^c \left(\chi_{\pi_l} - \chi_{\pi_s} \right), \tag{5.33}$$

where we use the symbol χ_{π_s} to represent the "pion" susceptibility that results if the light

#	T (MeV)	β	$\Delta^l_{\rm mp}/T^3$	$\Delta^s_{\rm mp}/T^3$	$\frac{m_l\chi^l_\pi+\Delta^l_{\rm mp}}{T^3}$	$\frac{m_s\chi^s_\pi+\Delta^s_{\rm mp}}{T^3}$
21	139	1.633	13.34(8)	1.833(11)	9.94(6)	41.21(2)
22	149	1.671	11.14(14)	1.939(10)	7.11(10)	36.52(3)
23	159	1.707	4.77(7)	1.038(6)	5.71(9)	33.71(5)
24	164	1.725	2.99(7)	0.757(5)	5.05(10)	32.00(5)
25	168	1.740	1.91(6)	0.576(5)	4.16(11)	30.70(7)
26	177	1.771	0.83(3)	0.329(2)	3.23(9)	27.94(3)
27	186	1.801	0.33(1)	0.193(2)	2.39(6)	25.42(4)
28	195	1.829	0.18(1)	0.118(1)	2.15(6)	23.20(2)
16	149	1.671	11.6(7)	2.02(7)	7.5(5)	36.6(3)
17	159	1.707	4.3(3)	1.05(4)	5.2(4)	33.6(3)
18	168	1.740	1.96(15)	0.61(3)	4.3(3)	31.2(2)
19	177	1.771	0.79(12)	0.33(2)	3.1(3)	28.0(2)
20	186	1.801	0.31(2)	0.184(7)	2.35(8)	25.2(1)
8	139	1.633	12.6(2)	1.825(21)	9.30(18)	41.26(8)
9	149	1.671	10.1(2)	1.922(13)	6.34(14)	36.43(6)
10	149	1.671	4.84(8)	0.815(7)	8.40(12)	38.24(6)
11	159	1.707	4.09(16)	1.034(10)	4.92(19)	33.64(7)
12	168	1.740	1.83(11)	0.573(7)	4.00(19)	30.73(8)
13	177	1.771	0.80(7)	0.326(4)	3.15(19)	27.89(7)
14	186	1.801	0.35(3)	0.196(3)	2.46(11)	25.50(6)
15	195	1.829	0.17(1)	0.118(1)	2.10(5)	23.22(4)

Table 5.1: The unrenormalized iso-vector pseudoscalar and mixed pseudoscalar/mid-point susceptibilities from ensembles with $m_\pi \approx 200$ MeV for the light and strange quarks as well as the combinations $(m_q\chi^q_\pi + \Delta^q_{\rm mp})/T^3$ for $q = l, s$, which appear in the Ward identity, Eq. (5.31). The Ward identity requires second- and first-from-right columns to agree with the fourth and the fifth columns from the left in Table 5.3 respectively. Moving from top to bottom, the three sections in this table correspond to the volumes $32^3 \times 8$, $24^3 \times 8$ and $16^3 \times 8$.

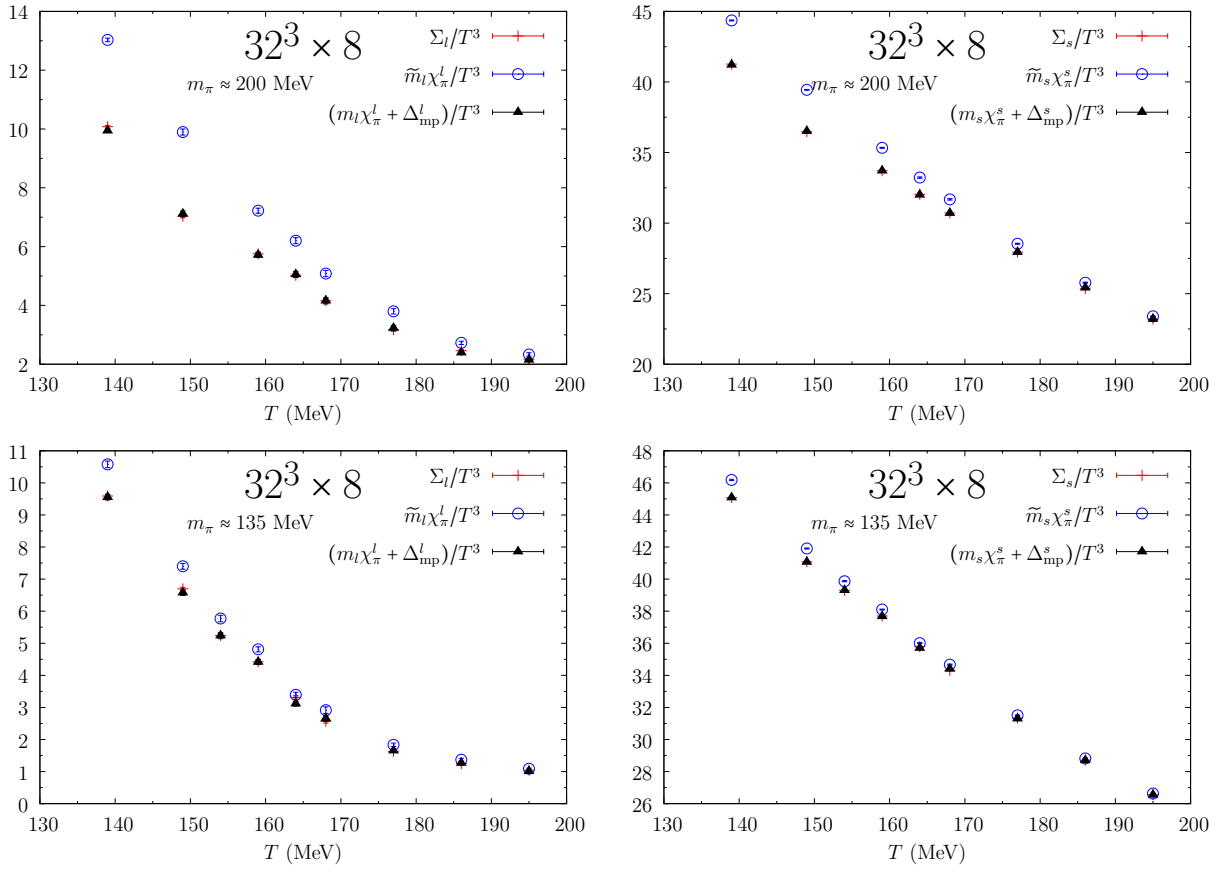

Figure 5.2: The left panel shows the light-quark chiral condensate, Σ_l, and the sum of $m_l\chi_\pi$ and the mixed $\pi - J_{5q}/2$ susceptibility to which it should be equal according to the Ward identity in Eq. (5.31). Also shown is $\widetilde{m}_l\chi_\pi$ which would equal Σ_l if $m_{\rm res}$ were the only effect of residual chiral symmetry breaking. The right panel shows the same quantities computed using the strange instead of the light quark. The top panel displays results from $m_\pi \approx 200$ MeV while the bottom panel from $m_\pi \approx 135$ MeV. Similar agreement between the right and left hand sides of Eq. (5.31) is found for the 24^3 and 16^3 volumes, as can be seen from Table 5.1

#	T (MeV)	β	$\Delta^l_{\rm mp}/T^3$	$\Delta^s_{\rm mp}/T^3$	$\frac{m_l\chi^l_\pi+\Delta^l_{\rm mp}}{T^3}$	$\frac{m_s\chi^s_\pi+\Delta^s_{\rm mp}}{T^3}$
29	139	1.633	8.59(8)	0.532(5)	9.56(9)	45.08(4)
30	149	1.671	5.37(7)	0.442(3)	6.58(8)	41.07(3)
31	154	1.689	3.02(6)	0.306(2)	5.24(10)	39.31(4)
32	159	1.707	1.76(4)	0.227(2)	4.42(8)	37.68(3)
33	164	1.725	0.95(3)	0.171(1)	3.12(8)	35.70(3)
34	168	1.740	0.65(3)	0.126(1)	2.65(10)	34.40(4)
35	177	1.771	0.27(1)	0.085(1)	1.65(5)	31.30(2)
36	186	1.801	0.12(1)	0.048(1)	1.27(4)	28.70(2)
37	195	1.829	0.06(1)	0.034(1)	1.01(2)	26.55(2)

Table 5.2: The same quantities as tabulated in Table 5.1 for the ensembles with $m_\pi \approx$ 135 MeV. The Ward identity identity requires second- and first-from-right columns to agree with the fourth and the fifth columns from the left in Table 5.4 respectively.

quark mass is replaced by that of the strange quark and add the subscript l to the usual pion susceptibility for clarity. From the perspective of the continuum theory both sides of Eq. (5.33) provide an equally good value for the subtracted chiral condensate. Neither quantity contains a quadratic divergence and the much smaller logarithmic divergences present on both sides are equal. For a DWF theory with residual chiral symmetry breaking this equation does not hold and the left hand side $\Delta_{l,s}$ contains an unphysical additive constant $O(m_{\rm res}/a^2)$. However, the right-hand side is much better defined with no $1/a^2$ term. Thus, we can use the right-hand side of Eq. (5.33) to provide a more physical result for $\Delta_{l,s}$ which will contain only a small, unphysical piece of order $m_l m_s^2 \ln(m_s a)$. Thus, we can define an improved value for $\Delta_{l,s}$:

$$\widetilde{\Delta}_{l,s} = \widetilde{m}_l \left(\chi_{\pi_l} - \chi_{\pi_s}\right) \tag{5.34}$$

which we will use to compare with spectral formulae and with the results for $\Delta_{l,s}$ from other

lattice fermion formulations.

5.2 Chiral Symmetry Restoration

In this section we present and discuss our numerical results for the chiral condensate and for the disconnected chiral susceptibility as a function of temperature.

5.2.1 Chiral Condensate

Fig. 5.3 shows the Monte Carlo time histories of the light-quark chiral condensate for seven of the temperatures studied with $m_\pi \approx 200$ MeV. The time evolutions for the $32^3 \times 8$ ensembles are displayed in the top left panel, those from $24^3 \times 8$ in the right left and $16^{\times}8$ in the bottom. The evolutions of the light-quark condensates from all sets of ensembles appear to follow the same trend. For the lower temperature region ($T \leq 168$ MeV), the light quark condensate fluctuates around its average value. However, as temperature grows higher, the fluctuations can better be described as upward spikes added to an otherwise flat base line.

This behavior is typically seen in finite temperature DWF calculations and arises because above T_c the main contribution to the chiral condensate comes from isolated, near-zero modes [120]. These modes become increasingly infrequent as the temperature is increased but, when present, produce a noisy, non-zero chiral condensate. The noise results from the relatively small space-time extent of each zero mode which is therefore sampled in our stochastic determination with relatively few random numbers.

Such behavior becomes most pronounced for $T \geq 186$ MeV in the $32^3 \times 8$ calculations. At $T = 177$ MeV, the $24^3 \times 8$ Monte Carlo time evolution shows this characteristic plateau-spike structure more distinctly than does the comparable $32^3 \times 8$ time history. This suggests a lower pseudo-critical transition temperature for the smaller volume or that the larger 32^3 volume supports a larger number of such zero modes, reducing the size of the intervals when

none are present and the chiral condensate is nearly zero.

If the correlation length is finite, the fluctuations of chiral condensate from the gauge noise should be suppressed by a factor in proportion to $\sqrt{V}$. Such volume effect can be observed from the evolution plots with different lattice sizes.

The Monte Carlo time histories of the light-quark chiral condensate for nine of the temperatures studied with $m_\pi \approx 135$ MeV are illustrated in Fig. 5.4. One stream of evolution at each temperature is presented for the $32^3 \times 8$ lattices (left panel) and for the $64^3 \times 8$ (right panel). The suppression of fluctuation from the volume effect is transparent from the comparison of the two panels. At the $64^3 \times 8$ volume, the short-term fluctuations can be easily seen to almost absent by examining the plot.

Moreover, the fluctuations of the chiral condensate are also inversely related to the quark mass, an effect which can be seen from a comparison of the $32^3 \times 8$ ensembles with different light quark masses. The plateau-spike structure starts to emerge at T = 168 MeV and becomes very pronounced at T = 177 MeV, which happens at lower temperatures than the $m_\pi \approx 200$ MeV ensembles. This indicates a lower pseudo-critical temperature for the physical pion ensembles as compared with those for heavier pions.

In the lower panel of Fig. 5.4, we also present four averaged time histories of the light quark chiral condensate on the $32^3 \times 8$ lattice with $m_\pi \approx 135$ MeV at T = 154 MeV, which is chosen to be very close to the pseudo-critical temperature. Two of the evolutions started with ordered ensembles (labeled as "ord" in the figure) while the other two with disordered ensembles (labeled as "dis" in the figure). Each point with separation of 20 configurations in the plot is an average of $\overline{\psi}_l \psi_l$ on 20 consecutive configurations All four streams converge quickly, no later than 200 trajectories, and no signal for the "two-state" fluctuation expected for a first-order transition are observed. This provides clear evidence for the absence of a first order phase transition for physical pion mass.

The ensemble averages of the light, subtracted and strange chiral condensates are sum-

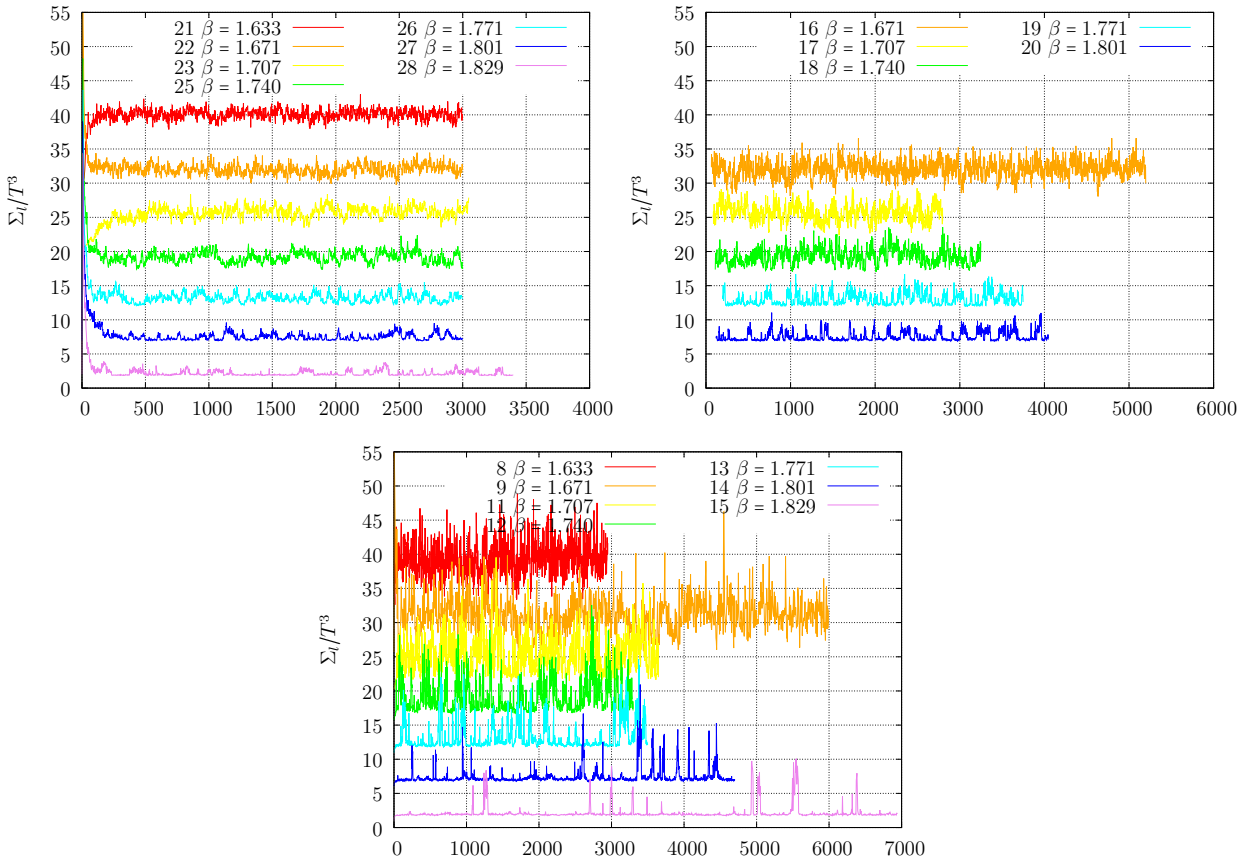

Figure 5.3: Monte Carlo time histories of the light-quark chiral condensate Σ_l/T^3 for the $32^3 \times 8$ (top left), $24^3 \times 8$ (top right) and $16^3 \times 8$ (bottom) ensembles with $m_\pi \approx 200$ MeV. (Only the longest streams from 16 and 17 are displayed.) There is a vertical offset of 5 units between successive data sets with the $\beta = 1.829$ results unshifted. Note that the time evolution corresponding to $\beta = 1.725$, $32^3 \times 8$ (24) behaves in a similar manner to those of its neighboring ensembles, but is omitted from the graph to preserve a uniform separation between each ensemble.

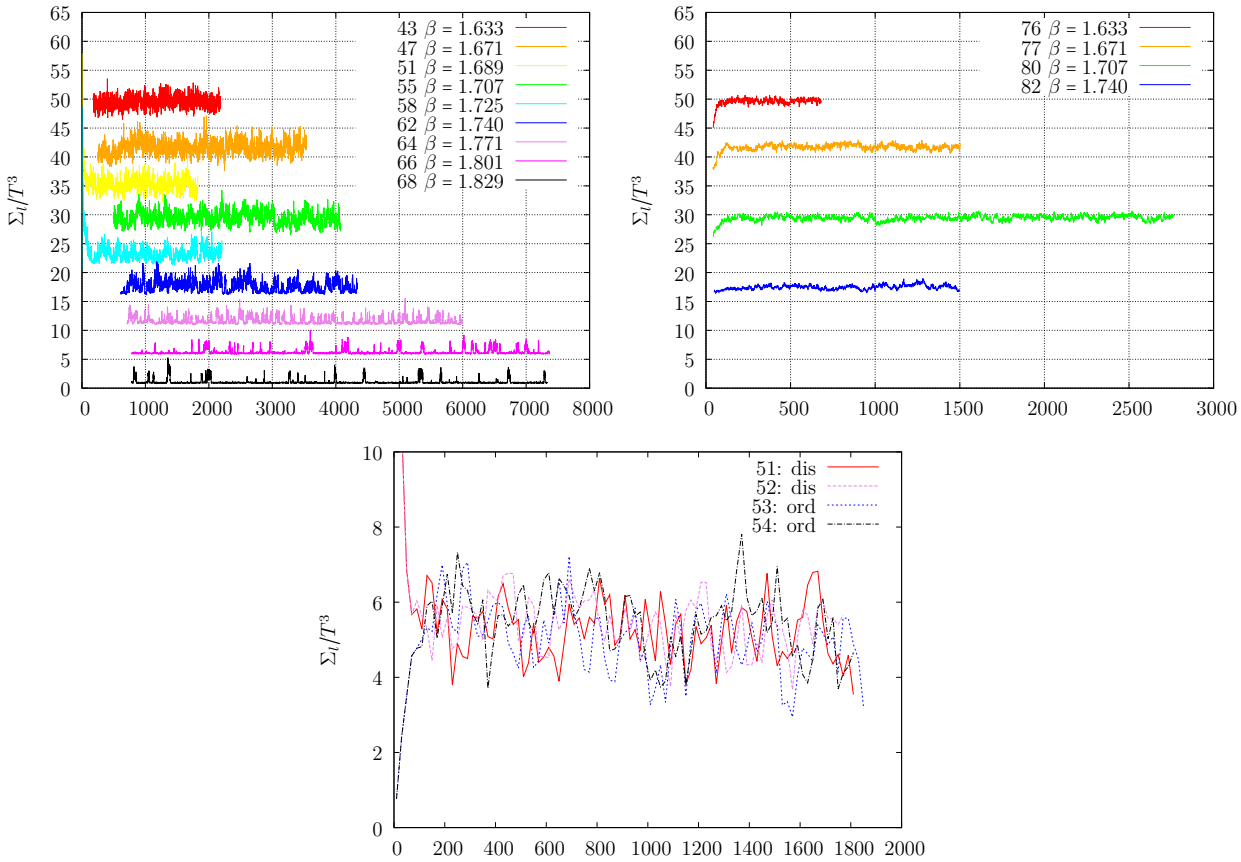

Figure 5.4: Monte Carlo time histories of the light-quark chiral condensate Σ_l/T^3 for the $32^3 \times 8$ (top left) and $64^3 \times 8$ (top right) ensembles with $m_\pi \approx 135$ MeV. (Only the longest streams at each temperature are displayed.) There is a vertical offset of 5 units between successive data sets from the $32^3 \times 8$ ensembles with the $\beta = 1.829$ results unshifted. The data from the $64^3 \times 8$ ensembles are vertically aligned with the corresponding $32^3 \times 8$ results. The bottom panel plot the four streams of time histories of the light-quark chiral condensate at $T = 154$ MeV. Each point represents the average of measurements made with 10 random sources on each of 20 successive configurations.

marized in Tables 5.3 and 5.4. The temperature dependence of the light and the subtracted condensates is also illustrated in Fig. 5.5. As that figure shows, for the $m_\pi \approx 200$ MeV ensembles, results from $32^3 \times 8$ and $24^3 \times 8$ ensembles agree well throughout the transition region, whereas those from the $16^3 \times 8$ ensembles show an appreciable discrepancy for $T < 168$ MeV, indicating a small but well-resolved finite volume effect. For the $m_\pi \approx 200$ MeV ensembles, both volumes give very similar results for all the temperatures under inspection, which suggests that $32^3 \times 8$ should be large enough even for the physical pion lattices.

Due to the m_q/a^2 divergence in the chiral condensate, the agreement of Σ_l between different pion masses depends on the subtraction scheme. Without subtraction, the divergent piece dominates at high temperature, where Σ_l differs between ensembles with different pion mass (upper panel in Fig. 5.5). With the subtraction scheme of Eq. 5.4, they agree well at temperatures above the transition region but differ at low temperatures. With $\widetilde{\Delta}_{l,s}$ defined in Eq. (5.34), they tend to be consistent for all temperatures.

5.2.2 Chiral Susceptibilities

A second measure of the restoration of $SU(2)_L \times SU(2)_R$ symmetry is the two differences $\chi_\pi - \chi_\sigma$ and $\chi_\eta - \chi_\delta$, following Eq. (5.13). These two $SU(2)_L \times SU(2)_R$-breaking differences are plotted in Fig. 5.6. The quantity $\chi_\pi - \chi_\sigma$ shows the behavior that might be expected from the temperature dependence of the chiral condensate shown Fig. 5.5. A large $SU(2)_L \times SU(2)_R$-breaking difference is seen for $T \leq 159$ MeV which becomes zero for $T \geq 168$ MeV with $m_\pi \approx 200$ MeV and $T \geq 164$ MeV with $m_\pi \approx 135$ MeV. A finite small $SU(2)_L \times SU(2)_R$-breaking difference is still present at $T = 164$ MeV with $m_\pi \approx 200$ MeV. The second difference $\chi_\eta - \chi_\delta$ is more surprising, being essentially zero throughout our temperature range. While we do not have a crisp explanation for this unexpected $SU(2)_L \times SU(2)_R$ symmetry below T_c we do expect this difference to vanish for $T > T_c$ and to be small relative to $\chi_\pi - \chi_\sigma$ for $T < T_c$ since the large value of χ_π reflects the small pion mass while the δ, σ and η are all

#	T (MeV)	β	Σ_l/T^3	Σ_s/T^3	$\Delta_{l,s}/T^3$	$\chi_{\rm disc}/T^2$	$\chi_{5,\rm disc}/T^2$	$\chi_{\rm top}/(\widetilde{m}_l T)^2$
21	139	1.633	10.07(4)	41.27(2)	6.40(4)	20(2)	118(7)	261(11)
22	149	1.671	7.03(6)	36.48(2)	3.84(5)	28(3)	94(8)	177(11)
23	159	1.707	5.80(6)	33.73(2)	2.83(6)	33(3)	70(8)	118(10)
24	164	1.725	5.02(7)	32.04(3)	2.16(7)	38(3)	49(4)	78(4)
25	168	1.740	4.16(8)	30.72(3)	1.46(7)	37(3)	38(5)	54(4)
26	177	1.771	3.17(5)	27.94(2)	0.71(5)	22(2)	24(3)	37(3)
27	186	1.801	2.46(4)	25.38(2)	0.22(4)	12(2)	10(2)	15(2)
28	195	1.829	2.15(3)	23.20(1)	0.14(3)	7(1)	10(1)	15(2)
16	148	1.671	7.10(6)	36.53(2)	3.90(6)	31(2)	89(5)	165(7)
17	159	1.707	5.58(10)	33.68(3)	2.66(10)	36(3)	64(6)	110(6)
18	168	1.740	4.40(10)	30.84(4)	1.69(10)	32(3)	47(6)	67(6)
19	177	1.771	3.03(7)	27.90(3)	0.57(7)	19(2)	21(3)	32(3)
20	186	1.801	2.58(6)	25.41(2)	0.34(6)	13(2)	14(2)	18(2)
8	139	1.633	9.26(13)	41.02(4)	5.61(12)	36(3)	113(7)	252(11)
9	149	1.671	6.26(12)	36.42(5)	3.07(12)	44(3)	89(6)	159(6)
10	149	1.671	8.39(10)	38.30(3)	5.00(10)	41(2)	90(6)	168(7)
11	159	1.707	5.25(17)	33.81(6)	2.27(16)	43(4)	55(6)	97(7)
12	168	1.740	4.03(18)	30.66(7)	1.33(18)	35(5)	37(5)	60(7)
13	177	1.771	3.16(15)	27.88(6)	0.71(15)	25(4)	24(4)	36(4)
14	186	1.801	2.44(9)	25.43(4)	0.20(9)	11(4)	9(3)	21(6)
15	195	1.829	2.10(5)	23.22(3)	0.09(5)	6(2)	6(2)	11(2)

Table 5.3: The unrenormalized chiral condensates and disconnected chiral susceptibilities for ensembles with $m_\pi \approx 200$ MeV. The two right-most columns should agree according to Eq. (5.26). As discussed, we attribute their large difference to inaccuracy in the strong-coupling measurement of $\chi_{\rm top}$. Moving from top to bottom, the three sections correspond to the volumes $32^3 \times 8$, $24^3 \times 8$ and $16^3 \times 8$.

#	T (MeV)	β	Σ_l/T^3	Σ_s/T^3	$\Delta_{l,s}/T^3$	$\chi_{\rm disc}/T^2$	$\chi_{5,\rm disc}/T^2$
29	139	1.633	9.59(3)	45.08(1)	9.43(3)	44(2)	232(9)
30	149	1.671	6.70(4)	41.09(1)	6.58(4)	67(3)	186(7)
31	154	1.689	5.25(6)	39.30(1)	4.70(6)	79(4)	140(7)
32	159	1.707	4.42(5)	37.70(1)	3.62(5)	71(3)	100(5)
33	164	1.725	3.32(5)	35.79(1)	2.46(5)	63(3)	79(5)
34	168	1.740	2.57(6)	34.31(1)	1.69(6)	55(4)	61(7)
35	177	1.771	1.63(3)	31.34(1)	0.73(3)	22(2)	23(2)
36	186	1.801	1.25(2)	28.70(1)	0.37(2)	13(1)	14(2)
37	195	1.829	1.04(2)	26.55(1)	0.20(2)	8(2)	7(1)
38	139	1.633	9.69(6)	45.08(2)	9.52(6)	42(9)	213(37)
39	148	1.671	6.76(3)	41.07(1)	6.64(3)	65(5)	187(11)
40	159	1.707	4.46(3)	37.68(1)	3.65(3)	75(7)	120(9)
41	168	1.740	2.53(6)	34.31(1)	1.65(6)	67(14)	58(15)

Table 5.4: The same quantities as are tabulated in Table 5.3 for the ensembles with $m_\pi \approx$ 135 MeV. The topological charge is not measured for these ensembles. Thus, the $\chi_{\rm top}$ column is excluded. Moving top to bottom, the two sections correspond to the volumes $32^3 \times 8$ and $64^3 \times 8$.

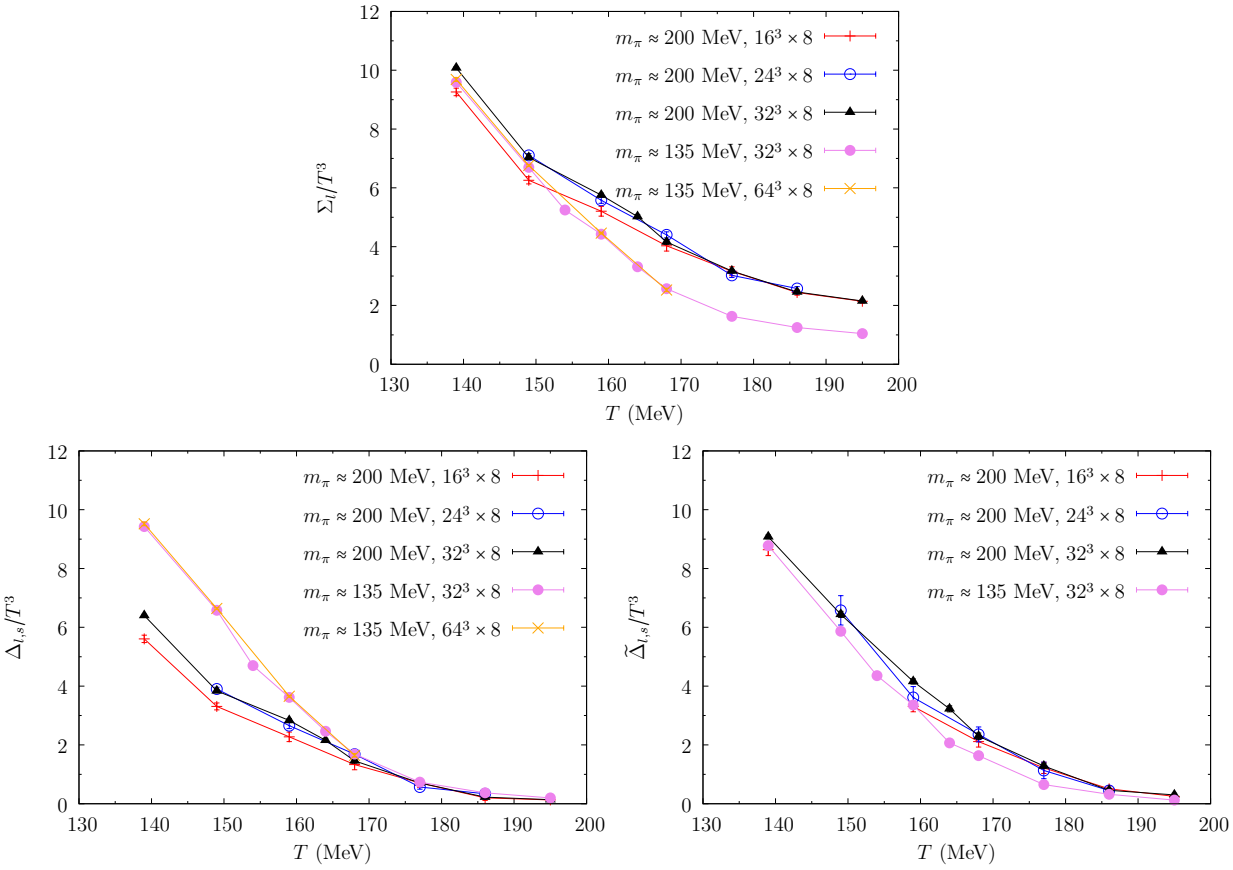

Figure 5.5: Comparison of light-quark (upper), subtracted (lower left) and improved subtracted (lower right) chiral condensates computed on different volumes with different pion masses. For $m_\pi \approx 200$ MeV, the 32^3 and 24^3 volumes agree reasonably well for all temperatures but are 5-10% larger than the corresponding values from the 16^3 volume for $T < 168$ MeV. The results appear to be volume independent for $T \geq 168$ MeV. Results from $m_\pi \approx 135$ MeV agree very well at all temperatures, but differ from the heavier pion mass results. The discrepancies depend on the subtraction scheme.

expected to be relatively massive below T_c.

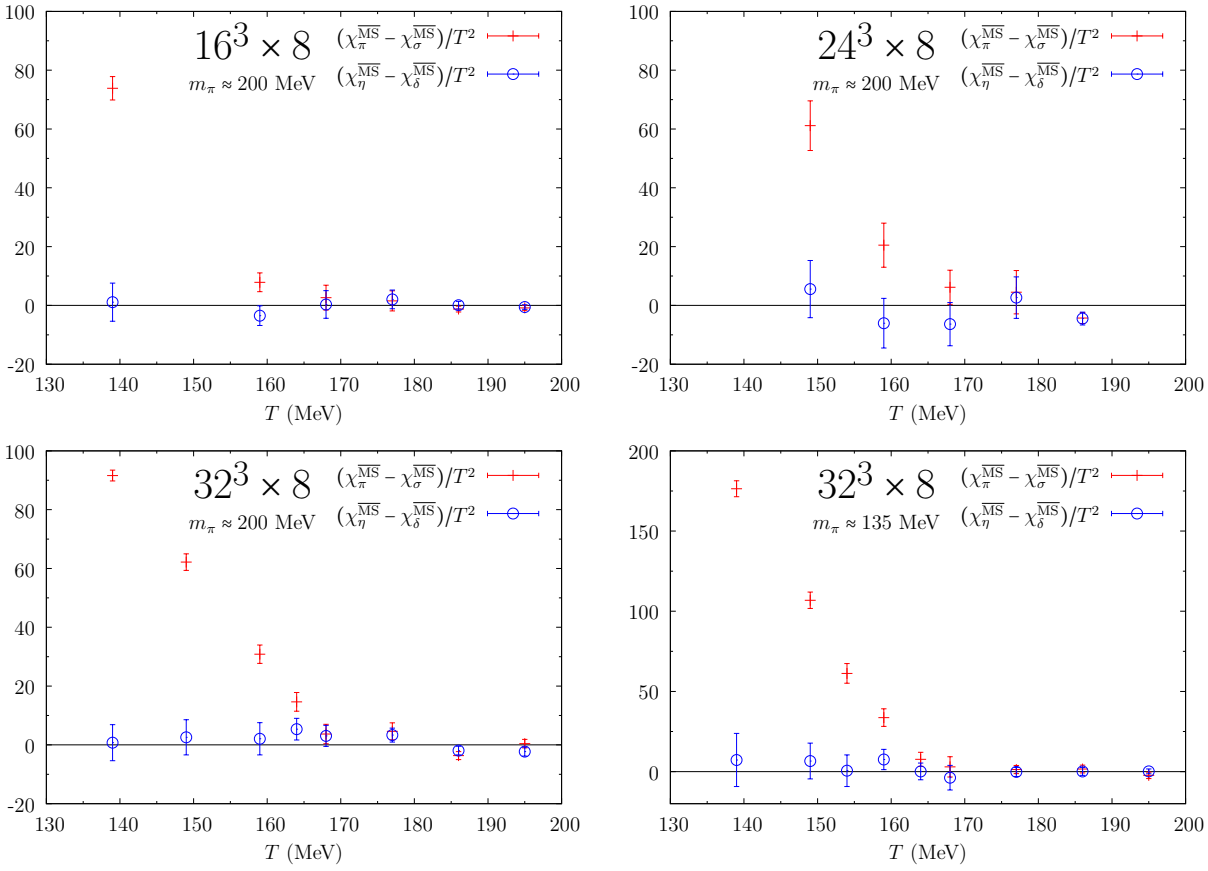

Figure 5.6: The two $SU(2)_L \times SU(2)_R$-breaking susceptibility differences $\chi_\pi^{\overline{\rm MS}} - \chi_\sigma^{\overline{\rm MS}}$ and $\chi_\delta^{\overline{\rm MS}} - \chi_\eta^{\overline{\rm MS}}$ plotted as a function of temperature for our three spatial volumes: 16^3, 24^3 and 32^3 with $m_\pi \approx 200$ MeV as well as for 32^3 with $m_\pi \approx 135$ MeV. For temperatures of 168 MeV (164 MeV for $m_\pi \approx 135$ MeV) and above these differences are consistent with zero and the expected restoration of chiral symmetry above T_c. The quantity $\chi_\pi - \chi_\sigma$ becomes very large below T_c reflecting the small mass of the pseudo-Goldstone π meson below T_c. In contrast, the second difference $\chi_\eta - \chi_\delta$ remains relatively small as the temperature decreases below T_c, reflecting the relatively large masses of the δ and η mesons.

While the chiral condensate is the order parameter for the chiral transition, its strong ap-

parent temperature dependence results from a combination of the finite temperature physics of interest and its dependence on the lattice scale as a dimension 3 operator. (This can be recognized by noting that we often discuss the dimensionless quantity Σ_l/T^3 which will change significantly with temperature simply because of the $1/T^3$ factor.) The location of the pseudo-critical temperature is much more easily seen by examining the disconnected chiral susceptibility $\chi_{\rm disc}$. This has dimension 2 and so varies a little less strongly with the lattice scale (which we are changing to varyint T on our $N_\tau = 8$ lattice) and shows a dramatic peak near the transition which can be used to define the the pseudo-critical temperature T_c as discussed in Chap. 3. Numerical results for $\chi_{\rm disc}$ before renormalization are presented in Table 5.3 for ensembles with $m_\pi \approx 200$ MeV and in Table 5.4 for ensembles with $m_\pi \approx 135$ MeV. The corresponding normalized values in the $\overline{\rm MS}(\mu = 2\ {\rm GeV})$ scheme are listed in Tables 5.5 and 5.7 in order to allow a comparison with results from the staggered formalism. Susceptibilities normalized in the $\overline{\rm MS}$ scheme at 2 GeV can be obtained from the directly-computed lattice quantities using the relation:

$$\chi^{\overline{\rm MS}} = \left(\frac{1}{Z_{m_f\to\overline{\rm MS}}}\right)^2 \chi^{\rm bare}. \tag{5.35}$$

The renormalization factor $Z_{m_f\to\overline{\rm MS}}$ is discussed in Chap. 6 when we discuss the renormalization of the eigenvalue distribution. They are obtained from the dependence of the pion mass, expressed in physical units, on the input quark mass and the known value of $\widetilde{m}_l$ which corresponds to the physical value of m_π [112]. These values for $Z_{m_f\to\overline{\rm MS}}$ are listed in Table 6.4.

The dependence of the renormalized $\chi_{\rm disc}$ on volume is shown in the left panel of Fig. 5.7. At $T = 168$ MeV and above the disconnected chiral susceptibilities from all volumes with $m_\pi \approx 200$ MeV agree within errors. For $T \geq 177$ MeV, they further converge to results from the $m_\pi \approx 135$ MeV ensembles.

However, at lower temperatures there is a large discrepancy between the $16^3 \times 8$ and the $32^3 \times 8$ ensembles with $m_\pi \approx 200$ MeV which becomes larger as temperature decreases. Results

from $24^3 \times 8$, fall in between, although they tend to lie closer to the $32^3 \times 8$ points. This volume effect is predicted with the $O(4)$ finite volume scaling behavior in Refs. [121, 122]. For ensembles with $m_\pi \approx 135$ MeV, the disconnected chiral susceptibilities from volumes 32^3 and 64^3 are consistent, though the errors for the results from the larger volume are still substantial. This is another piece of evidence strongly in favor of the absence of a first order phase transition.

Since we are studying only a single value of N_τ, it is premature to draw a definite quantitative conclusion about the pseudo-critical transition temperature. However, a qualitative examination of the left panel in Fig. 5.7 for ensembles with $m_\pi \approx 200$ MeV suggests that a peak in $\chi_{\rm disc}$ occurs for the 16^3 and 24^3 volumes at approximately 160 MeV and that this peak position increases to slightly above 165 MeV as the volume is increased to 32^3. For ensembles with $m_\pi \approx 135$ MeV, a distinct peak can be observed for the 32^8 volume at the $T = 154$ MeV point, while the curve for the 64^8 volume with fewer points and larger error-bars is peaked around $T = 160$ MeV. A quantitative extraction of the pseudo-critical temperature using a empirical formula will be discussed in the next subsection Sec. 5.2.3.

The right panel of Fig. 5.7 compares both the $m_\pi \approx 200$ MeV, DWF and $m_\pi \approx 135$ MeV MDWF results at volume $32^3 \times 8$ for $\chi_{\rm disc}$ with those obtained from staggered fermions using an $48^3 \times 12$ volume and the HISQ and ASQTAD staggered actions with $m_\pi = 161$ and 179 MeV respectively [5]. Again, the disconnected chiral condensates are consistent among these three methods for $T \geq 175$ MeV. However, the ASQTAD results lie substantially below the DWF and HISQ results for temperatures at and below the transition region. The HISQ results are in good agreement with the $32^3 \times 8$ $m_\pi \approx 200$ MeV DWF results. However, this agreement appears to be coincidental, since the HISQ results are obtained for a quoted pion mass of 161 MeV, significantly smaller than the 200 MeV pion mass of the DWF ensembles. The expected strong dependence of $\chi_{\rm disc}$ near T_c on the pion mass suggests that $m_\pi = 160$ MeV DWF results would lie above those found with HISQ. The discrepancy between the

DWF and ASQTAD results and the expected discrepancy with comparable HISQ results are likely explained by lattice discretization errors associated with staggered taste symmetry breaking. The disconnected chiral susceptibilities from the DWF ensembles with physical pions lie well above those with heavier pions for $T \leq 168$ MeV.

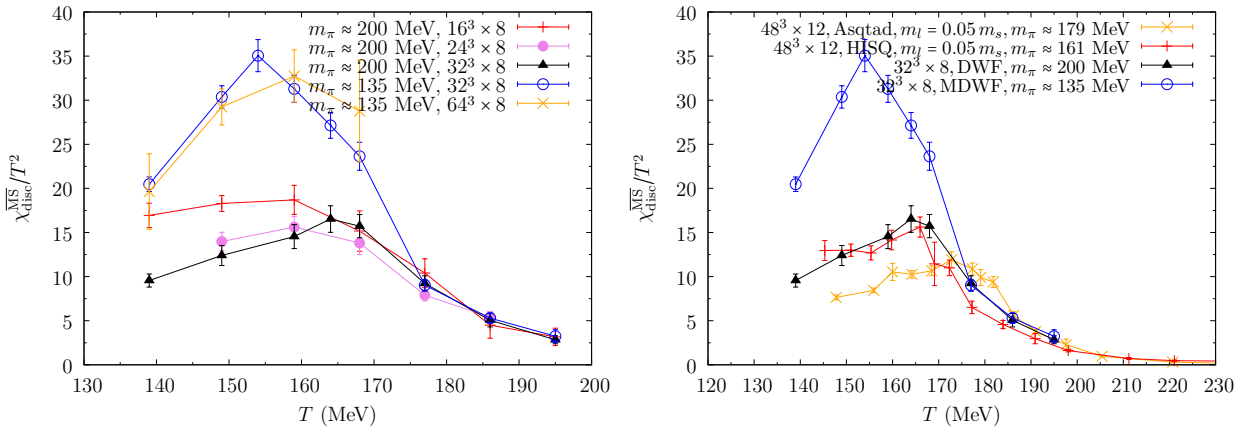

Figure 5.7: The left panel compares $\chi^{\overline{\rm MS}}_{\rm disc}$ computed using DWF on 32^3, 24^3 and 16^3 volumes with $m_\pi \approx 200$ MeV. Significant volume dependence can be seen between 32^3 and 16^3, while the 24^3 results agree with those from 32^3 within errors. The left panel also plots $\chi^{\overline{\rm MS}}_{\rm disc}$ from DWF ensembles with $m_\pi \approx 135$ MeV on 32^3 and 64^3 volumes, where no substantial volume effect is observed. The right panel compares the 32^3, $N_\tau = 8$ DWF results for $\chi^{\overline{\rm MS}}_{\rm disc}$ with those from staggered fermions on a $48^3 \times 12$ volume using both the ASQTAD and HISQ actions [5]. In each case $\chi^{\overline{\rm MS}}_{\rm disc}$ is renormalized in the $\overline{\rm MS}(\mu = 2\ {\rm GeV})$ scheme.

5.2.3 Determining T_c

In this subsection, we intend to determine the pseudo-critical temperature from our results for the disconnected chiral susceptibilities with $m_\pi \approx 135$ MeV.

If the QCD phase transition is described by the universality class of three-dimensional $O(2)$ or $O(4)$ model the scaling function for the order parameter (subtracted chiral conden-

sate) and its susceptibilities (the full chiral susceptibilities) should behave as one of the two shown in Fig. 5.8. Details of the scaling analysis as well as the effects of finite volume can be found in Refs. [123, 124, 122, 125].

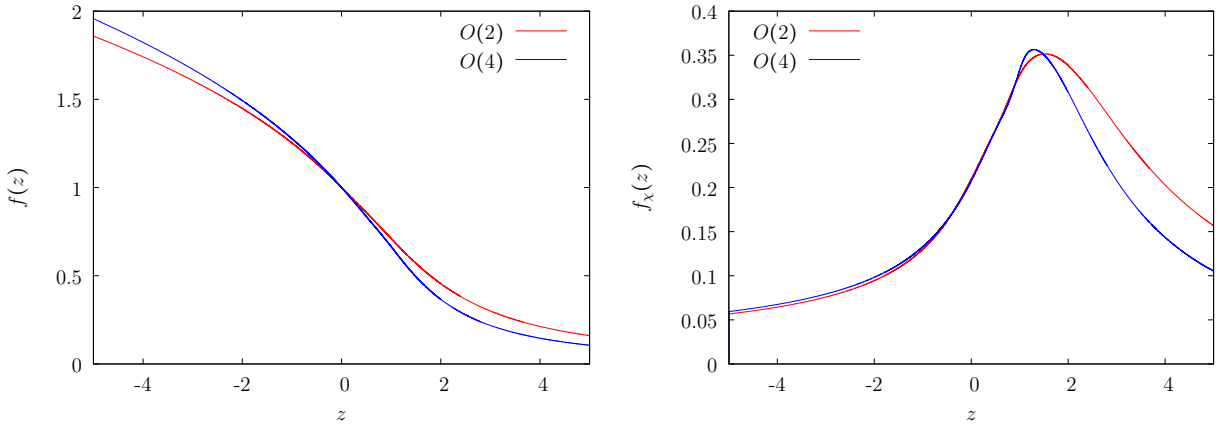

Figure 5.8: The left panel shows the scaling function for the order parameter for the universality classes of the three-dimensional $O(2)$ and $O(4)$ models. The right panel shows the scaling function for the chiral susceptibility.

With ensembles of two pion masses and several space-time volumes, we might venture to carry out a thorough scaling analysis of the chiral condensate and the full chiral susceptibility, including both the regular and sigular contributions. However, this analysis is beyond the scope of thie thesis. Instead, we are going to use some empirical formulae to describe the disconnected chiral susceptibilities near the phase transition region to locate the pseudo-critical temperature. These empirical formulae lack a deep physical interpretation, yet provide a quantitative tool to extract the pseudo-critical temperature from the dependence of the disconnected chiral susceptibility on temperature.

We adopt three fitting functions. The first is a Gaussian function for the three points within range 149 MeV $\leq T \leq$ 159 MeV. Our empirical fitting is performed with a "super-jackknife" method (for details *c.f.* [126]). Since the number of jackknife blocks from each

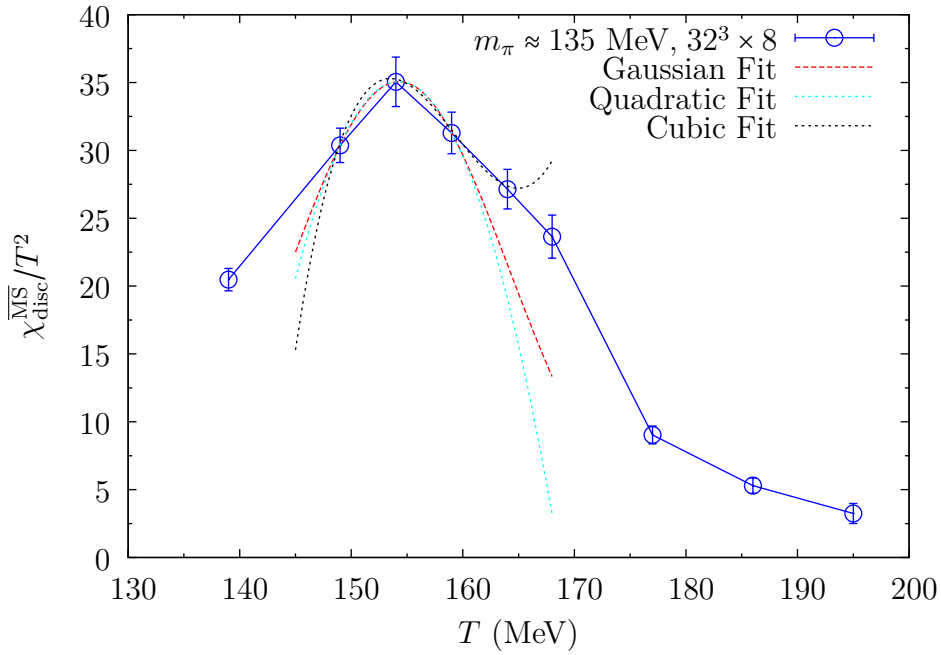

Figure 5.9: Empirical fits for the disconnected chiral susceptibilities. the red dashed line is the fitted curve for the Gaussian function within range 149 MeV $\leq T \leq$ 159 MeV. The black dotted line is the fitted curve for the cubic function within range 149 MeV $\leq T \leq$ 164 MeV. However, neither of them give a good description of the points that lie outside the fitting region.

ensemble is different, we join results from all three ensembles together in a larger jackknife data set, where each of three subsets contains one jackknife re-sampled $\chi^{\overline{\rm MS}}_{\rm disc}$ at one temperature and two ensemble averaged $\chi^{\overline{\rm MS}}_{\rm disc}$ from the other temperatures. Therefore the total number of elements in the super-jackknife data set N is the sum of numbers of jackknife data from each of the three ensembles. This factor N is also used to scale up the variance of the re-sampled data to get the estimator for the true error. The fitted result is $\chi^{\overline{\rm MS}}_{\rm disc}/T^2 = 35.1\exp\{-0.00514(T-154.3)^2\}$ which is represented by a red dotted line in Fig. 5.9. The pseudo-critical temperature is at $T_c = 154.3(6)$ MeV, which is not far from the $T = 154$ MeV point. Outside the fitting range, the fitting curve quickly deviates from the data points, as the Gaussian form has little physical significance. We also employ a quadratic form for fitting the three points, the cyan line on the plot. Its fitting result, $\chi^{\overline{\rm MS}}_{\rm disc}/T^2 = -0.0169T^2 + 52.1T - 3986$, is very close to the Gaussian form within the fitting region and so is its fitted pseudo-critical temperature $T_c = 154.3(6)$ MeV.

In order to incorporate the skewness, we also tried a cubic fitting form for the four points within range 149 MeV $\leq T \leq$ 164 MeV with the super-jackknife method, which results in $\chi^{\overline{\rm MS}}_{\rm disc}/T^2 = 0.0108T^3 - 5.15T^2 + 818T - 43280$, represented by a black dotted line in Fig. 5.9. The pseudo-critical temperature is quoted as $T_c = 153.5(8)$ MeV, consistent with the previous form, which is quite consistent with the other fitting result. However, the credibility of these fitted results for T_c should be discounted since all fitting forms fail outside the fitting region.

There are several issues that might affect the fitting results for the pseudo-critical temperature. Firstly, we adopt the temperature T rather than the β as the fitting variable. T is a derived quantity computed from the lattice spacing which contains errors in itself. However, within such a small interval, the relation between β and T is almost linear. If we had used β in the fit and then converted it back to the temperature, we will not shift the relative position of the peak. Secondly, the renormalization factors Z_m contain errors, which are not considered in the fitting. However, from Table 6.4, these factors are almost

uniform within the transition region. Even though a small overall shift in Z_m is possible, its effect on the fitting is insignificant. Thirdly, we the dimensionless quantity $\chi_{\rm disc}^{\overline{\rm MS}}/T^2$ rather than $\chi_{\rm disc}^{\overline{\rm MS}}$ in physical units is used in the empirical fittings. This would lead to about 10% relative change in $\chi_{\rm disc}$. However, the peak point at $T = 154$ MeV is so sharp that it easily overwhelms this relative change. Nevertheless, a small increase in T_c is expected if we had used $\chi_{\rm disc}^{\overline{\rm MS}}$ in physical units.

Therefore, based on the fitting presented in Fig. 5.9 and arguments in the previous paragraph, we would argue the T_c for $N_\tau = 8$ and $m_\pi \approx 135$ MeV should be close to $T = 154$ MeV, and is located by a distinct peak. If we take the expected discretization error ($5\% \times 154$ MeV ≈ 8 MeV) into account, it would dominate the error estimated for the pseudo-critical temperature. A more realistic value and error for T_c with finite lattice spacing and finite volume corrections would be expected if we were able to perform a complete $O(4)$ scaling analysis. Furthermore, additional ensembles in the vicinity of the peak would also be very beneficial.

5.3 $U(1)_A$ symmetry

We will now discuss the degree to which the anomalous $U(1)_A$ symmetry is restored above T_c by examining the two implications of this symmetry for the four susceptibilities given in Eq. (5.14): $\chi_\pi = \chi_\delta$ and $\chi_\sigma = \chi_\eta$. The numerical results for each of these four susceptibilities are summarized in Table 5.5 for ensembles with $m_\pi \approx 200$ MeV and in Table 5.7 for ensembles with $m_\pi \approx 135$ MeV as well as their $U(1)_A$-breaking differences $\chi_\pi - \chi_\delta$ and $\chi_\sigma - \chi_\eta$ which we will often abbreviate as $\Delta_{\pi,\delta} = \chi_\pi - \chi_\delta$ and $\Delta_{\sigma,\eta} = \chi_\sigma - \chi_\eta$. The integrated susceptibilities χ_π and χ_δ are calculated from the corresponding two point correlation functions by summing the position of the sink over the entire space-time volume. For the $16^3 \times 8$ and $24^3 \times 8$ ensembles, we use a single point source located at $(0, 0, 0, 0)$, while for the $32^3 \times 8$ ensembles with either pion masses, we use a random Z_2 wall source located at a fixed, 3-dimensional spatial slice,

perpendicular to one of the three spatial directions, e.g. $x = 0$.

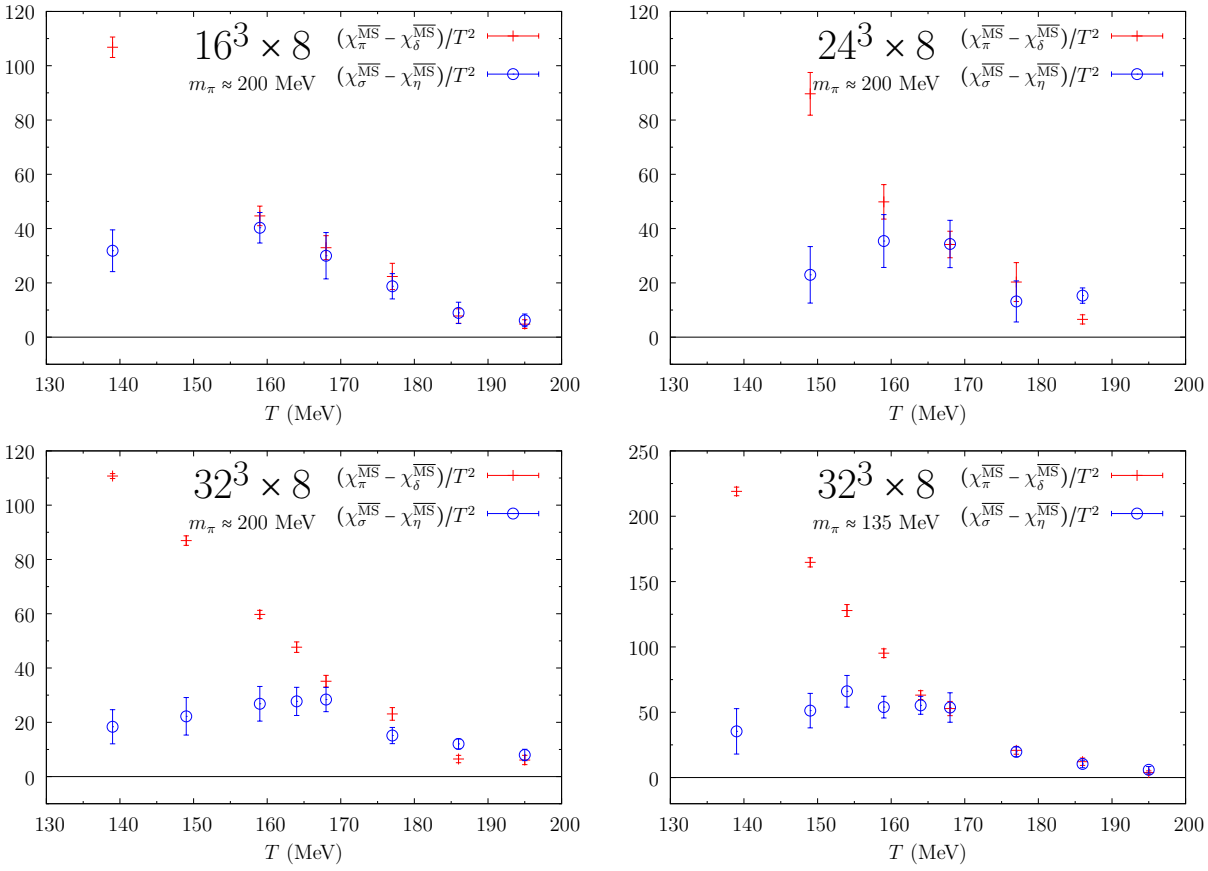

Figure 5.10: The two $U(1)_A$-violating susceptibility differences, $\chi_\pi - \chi_\delta$ and $\chi_\sigma - \chi_\eta$ plotted as a function of temperature for our three spatial volumes with $m_\pi \approx 200$ MeV and for $32^3 \times 8$ with $m_\pi \approx 135$ MeV. As expected these quantities are very different below T_c. However, even for temperatures of 159 MeV and above these quantities differ from zero by many standard deviations, providing clear evidence for anomalous symmetry breaking above T_c. The near equality of these two differences above T_c, which are related by $SU(2)_L \times SU(2)_R$ symmetry suggests that the effects of explicit chiral symmetry breaking are much smaller (as expected) than this anomalous symmetry breaking.

These two $U(1)_A$-breaking differences are plotted in Fig. 5.10. As can be seen, these

#	T (MeV)	$\chi_\pi^{\overline{\rm MS}}/T^2$	$\chi_\delta^{\overline{\rm MS}}/T^2$	$\chi_\sigma^{\overline{\rm MS}}/T^2$	$\chi_\eta^{\overline{\rm MS}}/T^2$	$\Delta_{\pi,\sigma}^{\overline{\rm MS}}/T^2$	$\Delta_{\eta,\delta}^{\overline{\rm MS}}/T^2$	$\Delta_{\pi,\delta}^{\overline{\rm MS}}/T^2$	$\Delta_{\sigma,\eta}^{\overline{\rm MS}}/T^2$
21	139	144.7(7)	34.0(3)	53(2)	35(6)	92(2)	1(6)	111(1)	18(6)
22	149	120.1(1.3)	33.1(6)	58(2)	36(6)	62(3)	3(6)	87(2)	22(7)
23	159	94.0(1.1)	34.3(5)	63(3)	36(6)	31(3)	2(5)	60(2)	27(6)
24	164	80.8(1.3)	33.2(8)	66(3)	39(4)	15(3)	5(4)	48(2)	28(5)
25	168	68.7(1.4)	33.6(9)	65(3)	37(4)	4(3)	3(4)	35(2)	28(4)
26	177	53.8(1.3)	30.8(1.1)	49(2)	34(2)	5(3)	3(2)	23(2)	15(3)
27	186	40.6(8)	34.1(6)	44(1)	32(1)	-4(1)	-2(1)	6(1)	12(2)
28	195	37.2(9)	31.1(8)	37(1)	29(1)	0.4(1.4)	-2(2)	6(2)	8(2)
16	149	122(6)	32(2)	61(4)	38(9)	61(8)	6(10)	90(8)	23(10)
17	159	87(5)	37(2)	66(4)	31(7)	20(8)	-6(8)	50(6)	35(10)
18	168	70(3)	36(2)	64(3)	30(7)	6(6)	-6(7)	34(5)	34(9)
19	177	52(4)	31(3)	47(4)	34(4)	4(7)	3(7)	20(7)	13(8)
20	186	40(1)	34(1)	44(1)	29(2)	-4(2)	-4(2)	7(2)	15(3)
8	139	140(2)	33(2)	66(3)	34(7)	74(4)	1(6)	107(4)	32(8)
9	149	111(2)	33(2)	73(2)	38(6)	39(4)	5(5)	78(4)	35(7)
11	159	83(2)	38(2)	75(3)	35(4)	8(3)	-3(3)	45(4)	40(6)
12	168	66(3)	33(2)	64(4)	34(5)	3(4)	0.3(4.7)	33(4)	30(9)
13	177	53(3)	31(2)	51(2)	33(3)	2(3)	2(3)	22(5)	19(5)
14	186	41(1)	34(1)	43(2)	34(2)	-1(1)	0.1(1.3)	8(3)	9(4)
15	195	36(1)	32(1)	37(1)	31(1)	-1(1)	-0.5(8)	5(2)	6(2)

Table 5.5: Results for the four independent susceptibilities χ_π, χ_δ, χ_σ and χ_η as well as the two pairs of differences, $\Delta_{\pi,\sigma} = \chi_\pi - \chi_\sigma$, $\Delta_{\eta,\delta} = \chi_\eta - \chi_\delta$ and $\Delta_{\pi,\delta} = \chi_\pi - \chi_\delta$, $\Delta_{\sigma,\eta} = \chi_\sigma - \chi_\eta$ which measure the degree of $SU(2)_L \times SU(2)_R$ and $U(1)_A$ symmetry, respectively for ensembles with $m_\pi \approx 200$ MeV. All of these susceptibilities are renormalized in the $\overline{\rm MS}(\mu = 2\ {\rm GeV})$ scheme using the renormalization factors listed in Table 6.4. Moving from top to bottom, the three sections correspond to the volumes $32^3 \times 8$, $24^3 \times 8$ and $16^3 \times 8$.

#	T (MeV)	$\chi_\pi^{s,\overline{\rm MS}}/T^2$	$\chi_\delta^{s,\overline{\rm MS}}/T^2$	$\chi_\sigma^{s,\overline{\rm MS}}/T^2$	$\chi_\eta^{s,\overline{\rm MS}}/T^2$	$\Delta_{\pi,\sigma}^{s,\overline{\rm MS}}/T^2$	$\Delta_{\eta,\delta}^{s,\overline{\rm MS}}/T^2$	$\Delta_{\pi,\delta}^{s,\overline{\rm MS}}/T^2$	$\Delta_{\sigma,\eta}^{s,\overline{\rm MS}}/T^2$
21	139	43.89(3)	31.50(2)	33.7(2)	42.9(4)	10.1(2)	11.4(4)	12.39(5)	-9.2(4)
22	149	41.96(3)	31.70(3)	33.8(2)	41.6(3)	8.2(2)	9.9(3)	10.26(5)	-7.9(4)
23	159	39.89(4)	31.71(3)	34.8(4)	39.0(3)	5.1(4)	7.3(3)	8.18(7)	-4.2(4)
24	164	38.77(5)	31.74(4)	35.6(4)	38.1(4)	3.2(4)	6.4(4)	7.02(8)	-2.6(5)
25	168	37.68(6)	31.67(3)	35.3(4)	37.1(3)	2.4(4)	5.4(3)	6.00(9)	-1.8(5)
26	177	35.65(5)	31.39(2)	33.4(3)	35.1(3)	2.2(3)	3.7(4)	4.26(6)	-1.7(5)
27	186	33.75(5)	30.83(3)	32.7(3)	33.4(3)	1.1(3)	2.5(3)	2.93(6)	-0.7(3)
28	195	32.37(4)	30.46(2)	31.7(1)	32.2(2)	0.7(1)	1.7(2)	1.91(4)	-0.5(3)
16	149	42.0(3)	31.57(16)	34.0(5)	41.5(5)	7.9(6)	10.0(5)	10.4(4)	-7.5(7)
17	159	39.7(3)	31.82(12)	34.4(3)	39.0(5)	5.3(4)	7.2(6)	7.9(4)	-4.6(6)
18	168	38.3(3)	31.73(11)	33.9(4)	37.7(4)	4.3(6)	5.9(4)	6.5(3)	-3.7(6)
19	177	35.7(2)	31.45(9)	33.5(2)	35.5(4)	2.2(3)	4.1(4)	4.2(3)	-2.0(5)
20	186	33.5(1)	30.84(7)	32.3(2)	32.9(3)	1.2(2)	2.0(3)	2.7(2)	-0.6(4)
8	139	43.95(7)	31.52(5)	33.8(2)	43.6(3)	10.2(2)	11.5(3)	12.44(11)	-9.3(4)
9	149	41.87(6)	31.79(5)	34.8(3)	41.1(4)	7.1(3)	9.4(4)	10.08(9)	-6.4(5)
11	159	39.81(8)	31.72(6)	34.6(3)	39.7(3)	5.2(3)	8.0(3)	8.09(13)	-5.1(4)
12	168	37.72(10)	31.68(6)	34.7(4)	38.0(4)	3.0(4)	6.4(4)	6.04(14)	-3.3(5)
13	177	35.58(9)	31.41(6)	33.9(2)	35.6(3)	1.6(2)	4.2(3)	4.18(13)	-1.7(3)
14	186	33.86(8)	30.87(4)	32.7(1)	34.0(2)	1.2(2)	3.1(2)	2.99(10)	-1.3(3)
15	195	32.41(6)	30.48(3)	31.8(1)	32.2(3)	0.6(1)	1.7(3)	1.92(5)	-0.3(3)

Table 5.6: The same quantities as tabulated in Table 5.5 but with the light quark replaced by the strange quark.

diminish rapidly with temperature but are many standard deviations from zero even at the temperatures of 177 and 186 MeV, well above T_c for ensembles with either pion mass. We expect that the effect of explicit chiral symmetry breaking, either from the non-zero input quark mass or finite-L_s, residual chiral symmetry breaking, on these differences will be much smaller.

5.3.1 Results from Ensembles with $m_\pi \approx 200$ MeV

With regard to ensembles with $m_\pi \approx 200$ MeV, we might estimate the contribution of explicit $U(1)_A$ breaking at $T > T_c$ to be of order $\widetilde{m}_l^2/T^2 \sim (0.004 \times 8)^2 = 0.001$ compared to results between 3 and 7 shown in Table 5.5. [1] Numerical evidence for the absence of explicit chiral symmetry breaking is provided by the near equality of the two differences $\chi_\pi - \chi_\delta$ and $\chi_\sigma - \chi_\eta$ which are related by $SU(2)_L \times SU(2)_R$ symmetry, a symmetry also explicitly broken by m_l and $m_{\rm res}$.

Strong evidence for the small size of possible explicit chiral symmetry breaking also comes from the results for $\chi_\pi - \chi_\delta$ computed for the strange quark. It is the explicit breaking of chiral symmetry by the valence propagators which can create a non-anomalous signal for $\chi_\pi - \chi_\delta$. As can be seen from Table 5.6 the results for $\chi_\pi - \chi_\delta$ are smaller for the strange than for the light quark. If the strange quark results are interpreted as coming entirely from explicit chiral symmetry breaking, the corresponding effects for the light quarks should be reduced by a factor of $(\widetilde{m}_l/\widetilde{m}_s)^2 \approx 0.008$. At $T = 177$ MeV, this approach gives explicit chiral symmetry breaking for the light quark quantity $\chi_\pi - \chi_\delta$ of order $4.26 \times 0.008 = 0.034$. This is larger than the 0.001 estimate above but only a fraction of a percent of the signal.

[1] This assumed quadratic dependence on $\widetilde{m}_l$ does not allow for a possible combined effect of explicit chiral symmetry breaking and the sort of non-analytic behavior above T_c that we are trying to study. We do not have sufficient numerical results to study such effects which we view as "second order" since they require both non-perturbative chiral breaking above T_c and $\widetilde{m}_l \neq 0$.

5.3.2 Results from Ensembles with $m_\pi \approx 135$ MeV

#	T (MeV)	$\chi_\pi^{\overline{\rm MS}}/T^2$	$\chi_\delta^{\overline{\rm MS}}/T^2$	$\chi_\sigma^{\overline{\rm MS}}/T^2$	$\chi_\eta^{\overline{\rm MS}}/T^2$	$\Delta_{\pi,\sigma}^{\overline{\rm MS}}/T^2$	$\Delta_{\eta,\delta}^{\overline{\rm MS}}/T^2$	$\Delta_{\pi,\delta}^{\overline{\rm MS}}/T^2$	$\Delta_{\sigma,\eta}^{\overline{\rm MS}}/T^2$
29	139	254(3)	35(1)	78(4)	42(17)	176(5)	7(17)	219(3)	35(17)
30	149	199(2)	32(1)	92(4)	41(12)	107(5)	7(11)	165(4)	51(13)
31	154	164(3)	40(2)	103(5)	37(10)	61(6)	1(10)	128(5)	66(12)
32	159	130(2)	39(1)	96(5)	42(6)	34(5)	8(6)	95(3)	54(8)
33	164	98(2)	38(1)	90(4)	35(5)	8(4)	0(5)	63(3)	55(7)
34	168	85(3)	28(3)	82(5)	28(8)	3(6)	-4(8)	53(5)	54(11)
35	177	55(2)	34(2)	53(2)	34(2)	1(3)	0(3)	21(3)	20(4)
36	186	44(1)	35(1)	42(1)	32(2)	2(2)	0(2)	12(3)	10(3)
37	195	36(1)	32(1)	39(2)	33(1)	-2(2)	0(2)	4(1)	6(3)

Table 5.7: The same quantities as tabulated in Table 5.5 for the $32^3 \times 8$ ensembles with $m_\pi \approx 135$ MeV.

For ensembles with $m_\pi \approx 135$ MeV, $\chi_\pi - \chi_\delta$ remains at approximately the same level as seen for $m_\pi \approx 200$ MeV (Table 5.7), in contrast to the explicit chiral symmetry breaking contribution which is expected to decrease with decreasing quark masses. A similar argument for the strange susceptibility and light susceptibility discussed in the previous subsection applies here as well. Moreover, the agreement between the two differences $\chi_\pi - \chi_\delta$ and $\chi_\sigma - \chi_\eta$ are remarkable for $T \geq 168$ MeV, providing strong support for the restoration of chiral symmetry.

In sum, we interpret the results for $\chi_\pi - \chi_\delta$ and $\chi_\sigma - \chi_\eta$ shown in Tables 5.5 and 5.7 and Fig. 5.10 as clear evidence for the anomalous breaking of $U(1)_A$ symmetry for $T > T_c$ with both $m_\pi \approx 200$ MeV and $m_\pi \approx 135$ MeV.

#	T (MeV)	$\chi_\pi^{s,\overline{\rm MS}}/T^2$	$\chi_\delta^{s,\overline{\rm MS}}/T^2$	$\chi_\sigma^{s,\overline{\rm MS}}/T^2$	$\chi_\eta^{s,\overline{\rm MS}}/T^2$	$\Delta_{\pi,\sigma}^{s,\overline{\rm MS}}/T^2$	$\Delta_{\eta,\delta}^{s,\overline{\rm MS}}/T^2$	$\Delta_{\pi,\delta}^{s,\overline{\rm MS}}/T^2$	$\Delta_{\sigma,\eta}^{s,\overline{\rm MS}}/T^2$
29	139	43.24(4)	31.19(2)	33.0(2)	42.4(6)	10.2(2)	11.2(6)	12.05(4)	-9.4(6)
30	149	41.30(3)	31.35(2)	33.9(2)	41.0(6)	7.4(2)	9.7(6)	9.95(4)	-7.1(6)
31	154	40.30(4)	31.36(2)	33.7(2)	40.4(5)	6.7(2)	9.1(5)	8.94(5)	-6.8(5)
32	159	39.26(3)	31.34(2)	33.6(2)	38.9(4)	5.7(2)	7.5(4)	7.92(4)	-5.3(5)
33	164	38.10(3)	31.41(2)	33.6(2)	38.1(4)	4.5(2)	6.6(4)	6.69(4)	-4.5(5)
34	168	37.29(4)	31.21(2)	33.5(3)	37.1(5)	3.8(3)	5.9(4)	6.08(5)	-3.6(6)
35	177	35.20(3)	30.90(2)	32.7(1)	35.2(4)	2.5(1)	4.3(4)	4.29(3)	-2.5(4)
36	186	33.44(2)	30.37(1)	31.9(1)	33.1(4)	1.5(1)	2.8(4)	3.07(3)	-1.2(4)
37	195	32.21(2)	30.03(1)	31.2(1)	32.7(3)	1.0(1)	2.7(3)	2.18(2)	-1.5(3)

Table 5.8: The same quantities as are tabulated in Table 5.7 but with the light quark replaced by the strange quark.

Chapter 6

Eigenvalue Distributions of the Dirac Operator

The spectrum of eigenvalues of the Hermitian Dirac operator provides important insights into the physics of QCD. The Dirac spectrum depends dramatically on the temperature and is fundamentally connected with both the spontaneous and the anomalous chiral symmetry breakings.

This chapter starts with an introduction to the connections between the Dirac eigenvalue spectrum and a variety of physical quantities that are closely related to the QCD phase transition. In Sec. 6.2, we explain how the continuum Dirac spectrum can be determined from the distribution of these eigenvalues. And in Sec. 6.3, we briefly describe how the eigenvalues on the five-dimensional lattice are collected with Ritz and Lanczos methods. The resulting DWF Dirac eigenvalue spectrum for the finite temperature DWF ensembles with $m_\pi \approx 200$ MeV, computed and normalized following these methods will be presented and analyzed in an effort to determine the temperature dependence and the origin of the chiral and the anomalous $U(1)_A$ symmetry breakings in the last three sections of this chapter.

6.1 Preliminaries

The most familiar relation between the Dirac spectrum and an important QCD observable is the spectral expression for the chiral condensate,

$$\Sigma_q = -\left\langle \overline{\psi}\psi \right\rangle_q = \int_0^\infty \mathrm{d}\lambda\, \rho(\widetilde{m}_l, \widetilde{m}_s, \lambda) \frac{2\widetilde{m}_q}{\widetilde{m}_q^2 + \lambda^2}, \qquad q = l, s. \tag{6.1}$$

Here we have used the symmetry $\rho(\lambda) = \rho(-\lambda)$, limiting the integral to non-negative values of λ and introducing the compensating factor of 2 in the numerator. In the infinite volume and chiral limits and applied to the light quark condensate, this equation becomes the well-known Banks-Casher relation [127]:

$$-\lim_{\widetilde{m}_l \to 0} \lim_{V \to \infty} \left\langle \overline{\psi}\psi \right\rangle_l = \lim_{\lambda \to 0} \lim_{\widetilde{m}_l \to 0} \lim_{V \to \infty} \pi \rho(\widetilde{m}_l, \widetilde{m}_s, \lambda). \tag{6.2}$$

Therefore, if the eigenvalue density $\rho(\widetilde{m}, \lambda)$ is non-vanishing in infinite volume at λ and $\widetilde{m}$ approaches zero, chiral symmetry will be broken by a non-vanishing quark condensate.

While we have used the lattice variable $\widetilde{m}_q$ to represent the quark mass in this equation, it should be emphasized that this is an equation derived in continuum field theory. The equivalent expression, derived for DWF in a lattice theory will be quite different. For example, a spectral expression for Σ_q derived from an eigenmode expansion of the DWF lattice propagator will involve wave functions for the five-dimensional modes evaluated on and integrated over the two $s = 0$ and $s = L_s - 1$, four-dimensional faces, yielding an expression significantly more complex than that given in Eq. (6.1) [116]. However, when appropriately renormalized, the eigenvalue density $\rho(\widetilde{m}, \lambda)$ is a physical quantity that can be computed using lattice methods [128]. How we collect the eigenvalues of the lattice Dirac operator and how we renormalize the eigenvalue distributions will be discussed in detail in Sec. 6.3 and Sec. 6.2 respectively.

Since in a lattice calculation the Banks-Casher limit of infinite volume and vanishing quark mass cannot be easily evaluated, we would like to use Eq. (6.2) for the case of finite volume and non-zero quark mass. However, in that case the integral over λ diverges

quadratically. As a result, this equation is dominated by the region of large λ where the DWF lattice and continuum formalisms should not agree. This region is also well outside the limited range of the 100 lowest eigenvalues which we have computed. However, much can be learned from Eq. (6.2) if we use it to evaluate the difference $\Delta_{l,s}$, subtracting the light and strange quark equations. This difference will be studied in Sec. 6.6, comparing the subtracted spectral integral with both the simple difference of condensates, $\Delta_{l,s}$ and the improved quantity $\widetilde{\Delta}_{l,s}$ defined in Eqs. (5.4) and (5.34) respectively.

In a similar manner, the difference between the connected pseudoscalar and scalar light-quark susceptibilities, $\chi_\pi - \chi_\delta$, which serves as a good indicator of $U(1)_A$ symmetry breaking, can be expressed as a spectral integral [129]:

$$\Delta_{\pi,\delta} \equiv \chi_\pi - \chi_\delta = \int_0^\infty \mathrm{d}\lambda\, \rho(\widetilde{m}_l, \lambda) \frac{4\widetilde{m}_l^2}{(\widetilde{m}_l^2 + \lambda^2)^2}, \tag{6.3}$$

where again this is a continuum equation which requires that all of the quantities which appear are renormalized in a consistent scheme. In contrast to Eq. (6.2), this expression is only logarithmically divergent and for our values of the lattice spacing and quark masses, is dominated by the region where λ is small – the region in which we have measured the spectrum and in which the lattice and continuum spectral functions should agree, except for the usual $O(a^2)$ errors inherent in a calculation at non-zero lattice spacing.

In order to distinguish and to better understand the effects of different possible behaviors of $\rho(\widetilde{m}_l, \lambda)$ we will also make use of the small λ and small $\widetilde{m}$ parametrization for $\rho(\widetilde{m}_l, \lambda)$,

$$\rho(\widetilde{m}, \lambda) = c_0 \widetilde{m}^2 \delta(\lambda) + c_1 |\lambda| + c_2 \widetilde{m} + \cdots, \tag{6.4}$$

appropriate for $T \geq T_c$ and introduced in Ref. [35]. Each term provides an ansätz for a possible behavior of $\rho(\widetilde{m}_l, \lambda)$ and results in a different contribution to the susceptibility difference. In particular, $\Delta_{\pi,\delta}$ will receive three corresponding contributions:

$$\Delta_{\pi,\delta} \approx 2c_0 + 2c_1 + \pi c_2 \equiv \Delta^0_{\pi,\delta} + \Delta^1_{\pi,\delta} + \Delta^2_{\pi,\delta}. \tag{6.5}$$

Once the eigenvalue density has been computed and fit to the form assumed in Eq. (6.4), the resulting coefficients can be used to calculate $\Delta_{\pi,\delta}$ and discover which of these three behaviors gives the dominant contribution to the spectral integral.

In addition to allowing a quantitative measure of the relative importance of these three possible behaviors, the use of the analytic expression in Eq. (6.4) also allows us to potentially correct finite-lattice spacing errors which may be important for small λ in our DWF formulation with finite L_s. Although much more accurate, the Hermitian DWF spectrum, like the Wilson spectrum, does not have the continuum form $\Lambda = \pm\sqrt{\lambda^2 + \widetilde{m}_l^2}$ where $\widetilde{m}_l = m_l + m_{\text{res}}$, at least for finite volume, finite L_s and non-zero lattice spacing. For eigenvalues Λ of D_H on the order of m_{res}, *i.e.* $\Lambda \lessapprox 10$ MeV, we expect deviations from the continuum $\pm\sqrt{\lambda^2 + \widetilde{m}_l^2}$ form because of residual chiral symmetry breaking. These effects do not occur if we use $\rho(\lambda)$ given by Eq. (6.4). In fact, comparing results obtained by direct summation over the measured spectrum with those obtained using Eq. (6.4) provides an estimate of the importance of these finite lattice spacing errors.

Each of the three terms in Eq. (6.4) corresponds to potentially interesting behavior. The λ-independent $c_2\widetilde{m}$ term is expected to dominate the behavior below T_c and should describe the Banks-Casher contribution to the chiral condensate Σ_l. For $T < T_c$ the factor of $\widetilde{m}$ should not appear but has been introduced here because above T_c the condensate should vanish in the limit $\widetilde{m} \to 0$. As can be seen in Eq. (6.5), this $c_2\widetilde{m}$ term will result in $\Delta_{l,s} \neq 0$ and anomalous symmetry breaking. Likewise, the linear c_1 term provides a possible mechanism for $U(1)_A$ symmetry breaking above T_c. Both the c_1 and c_2 terms are sufficiently regular as λ and $\widetilde{m}$ approach 0 that they do not result in an explicit $SU(2)_L \times SU(2)_R$ symmetry breaking chiral condensate but have sufficient infra-red singularity that the presence of either does result in a non-zero value for $\chi_\pi - \chi_\delta$. Thus, either term in $\rho(\lambda)$ could describe the behavior we see for $T > T_c$ where Σ_l should vanish as $\widetilde{m}_l \to 0$ but $\chi_\pi - \chi_\delta$ is non-zero. As we will see, neither term appears to be present with a sufficient magnitude to describe $\chi_\pi - \chi_\delta$

for $T > T_c$.

As is discussed below, the c_0 term has the greatest relevance. This term represents the Dirac spectrum that results from the dilute instanton gas approximation (DIGA) [104]. Asymptotic freedom implies that at sufficiently high temperature, the QCD partition function will be governed by weak-coupling phenomena. These should include a "dilute gas" of instantons and anti-instantons of radius $\approx 1/T$ and density $\propto \widetilde{m}_l^2 \exp\{-8\pi^2/g^2(T)\}$ decreasing with increasing temperature, where $g(T)$ is the running QCD coupling constant evaluated at the energy scale T. The number of such instantons and anti-instantons is proportional to the volume and each will induce a near-zero mode in the Dirac eigenvalue spectrum. (These eigenvalues will not be exactly zero because of the overlap of the "zero-mode" wave functions associated with neighboring instantons.) The factor of $\widetilde{m}^2$ in the instanton density arises from the fermion determinant for two light flavors of quarks. The contribution of such a dilute gas of instantons and anti-instantons to the Dirac spectrum will be accurately described by the c_0 term in Eq. (6.4), at least for sufficiently high temperatures. As can be seen from Eq. (6.5), such a term will result in a non-zero value for the difference $\chi_\pi - \chi_\delta$ even in the chiral limit, $\widetilde{m}_l \to 0$. The expected presence of such effects leads to the phrase "effective restoration of $U(1)_A$ symmetry", since these effects, which should appear as T becomes very large, will lead to a possibly very small but non-vanishing result of $\chi_\pi - \chi_\delta$.

As we will demonstrate in Sec. 6.7 we find a significant cluster of near-zero modes in the Dirac spectrum whose number is proportional to the volume with the characteristics expected from the DIGA. We conclude that the non-zero value of $\chi_\pi - \chi_\delta$ in the region just above T_c is explained by the DIGA and that this is the dominant mechanism for our observed, non-zero breaking of $U(1)_A$ just above T_c.

6.2 Renormalization of the Domain Wall Eigenvalue Distribution

6.2.1 Relating the Continuum and DWF Dirac Spectrum

The domain wall fermion formulation can be viewed as a five-dimensional theory whose low energy properties accurately reproduce four-dimensional QCD. All low energy Green's functions and matrix elements are expected to agree with those of a four-dimensional theory and it is only at high momenta or short distances that the five dimensional character of the theory becomes visible. This perspective applies also to the five-dimensional DWF Dirac operator whose small eigenvalues and corresponding eigenstates should closely approximate those of a continuum four-dimensional theory. This can be shown explicitly for the free theory, order-by-order in perturbation theory and by direct numerical evaluation in lattice QCD. With the exception of gauge configurations which represent changing topology, the modes with small eigenvalues are literally four-dimensional with support concentrated on the four-dimensional left and right walls of the original five-dimensional space.

Thus, we can learn about the continuum Dirac eigenvalue spectrum by directly studying that of the DWF Dirac operator, D_{DWF}, as defined by Eqs. (2.31) and (2.32) in Chap. 2. Of course, just as with other regulated versions of the continuum theory, explicit renormalization is needed to convert from a bare to a renormalized eigenvalue density. Because the continuum Dirac operator, $\not{D} + m$, is linear in the quark mass, we should expect the Dirac eigenvalues to be related between different renormalization schemes by the same factor Z_m that connects the masses. If we have two regularized theories which describe the same long distance physics with bare masses m and $m' = Z_{m\to m'} m$, then we should expect that their eigenvalue densities would be related by:

$$\rho'(\lambda') = \frac{1}{Z_{m\to m'}} \rho\left(\lambda'/Z_{m\to m'}\right). \tag{6.6}$$

Note this expectation is consistent with the form of the Banks-Casher relation, $\langle\overline{\psi}\psi\rangle = \pi\rho(0)$,

as the equality of the mass term in equivalent theories requires $\langle \overline{\psi}' \psi' \rangle = \langle \overline{\psi}\psi \rangle / Z_{m \to m'}$.

The renormalization of the bare input quark mass, m_f, for DWF has been extensively studied and the factor $Z_{m_f \to \overline{\rm MS}}(\mu^2)$ needed to convert this input bare mass to a continuum, $\overline{\rm MS}$ value at the scale μ is accurately known [112] and will be summarized later in Sec. 6.2.3. However, in contrast to the continuum theory or staggered or Wilson lattice fermions, the input quark mass for DWF does not enter as an additive constant but instead appears as a coupling strength between the two four-dimensional walls. Thus, for DWF the Dirac spectrum and the quark mass will in general be related to their continuum counterparts by *different* renormalization factors. To properly renormalize the DWF Dirac spectrum we should begin with the Hermitian operator $\gamma_5 R_5 D_{\rm DWF}$ and then add a multiple of the identity:

$$\gamma_5 R_5 D_{\rm DWF} + m_{\rm tw} = \gamma_5 R_5 \left(D_{\rm DWF} + \gamma_5 R_5 m_{\rm tw} \right), \tag{6.7}$$

where R_5 is the fifth dimension reflection operator introduced in the previous section. The renormalization factor, $Z_{\rm tw \to \overline{\rm MS}}$, needed to convert the DWF spectrum to the continuum, $\overline{\rm MS}$ spectrum then relates this new DWF pseudoscalar operator to the corresponding $\overline{\rm MS}$ continuum operator:

$$\left(\overline{\psi}(x) \gamma_5 \psi(x) \right)^{\overline{\rm MS}} \approx \frac{1}{Z_{\rm tw \to \overline{\rm MS}}} \sum_{s=0}^{L_s - 1} \overline{\Psi}(x, s) \gamma_5 \Psi(x, L_s - 1 - s), \tag{6.8}$$

where $\Psi(x, s)$ is the five-dimensional DWF field. These two operators, which appear in different theories, are equated in Eq. (6.8) in the sense that they give the same matrix elements when inserted in corresponding long-distance Green's functions.

It is convenient to determine the renormalization constant $Z_{\rm tw \to \overline{\rm MS}}$ in two steps. In the first we determine the constant $Z_{\rm tw \to m_f}$ which relates this reflected pseudoscalar term and the standard pseudoscalar term belonging to the same chiral representation as the usual DWF mass term $\overline{\psi}\psi$:

$$\overline{\psi}(x) \gamma_5 \psi(x) = \frac{1}{Z_{\rm tw \to m_f}} \overline{\Psi}(x) R_5 \gamma_5 \Psi(x), \tag{6.9}$$

where the operator on the right-hand side is the same as that in the right-hand side of Eq. (6.8) with the explicit sum over the s coordinate suppressed.

Then in the second step we perform the well-understood conversion between the standard DWF mass operator and a continuum, $\overline{\text{MS}}$ normalized mass operator using $Z_{m_f\to\overline{\text{MS}}}$:

$$Z_{\text{tw}\to\overline{\text{MS}}} = Z_{m_f\to\overline{\text{MS}}} Z_{\text{tw}\to m_f}. \tag{6.10}$$

After the first step, we can compare the eigenvalue density $\rho(\lambda)$ for the lattice DWF operator with the usual lattice result for the chiral condensate using the Banks-Casher relation,

$$\langle\overline{\psi}\psi\rangle = \frac{\pi}{Z_{\text{tw}\to m_f}}\rho(0), \tag{6.11}$$

since both the left- and right-hand sides now use the same bare normalization conventions. In the second step we are simply dividing both sides of Eq. (6.11) by the common factor $Z_{m_f\to\overline{\text{MS}}}$ to convert from lattice to $\overline{\text{MS}}$ normalization.

6.2.2 Calculation of $Z_{\text{tw}\to m_f}$

Because the operators $\overline{\psi}(x)\gamma_5\psi(x)$ and $\overline{\Psi}(x)R_5\gamma_5\Psi(x)/Z_{\text{tw}\to m_f}$ are supposed to be equivalent at long distances, we can determine the needed factor $Z_{\text{tw}\to m_f}$ by simply taking the ratio of equivalent Green's functions, evaluated at distances greater than the lattice spacing a, containing these two operators:

$$Z_{\text{tw}\to m_f} = \frac{\left\langle O_1 \ldots O_n \overline{\Psi}(x) R_5\gamma_5\Psi(x)\right\rangle}{\left\langle O_1 \ldots O_n \overline{\psi}(x)\gamma_5\psi(x)\right\rangle}, \tag{6.12}$$

where the numerator and denominator in this expression are intended to represent identical Green's functions except for the choice of pseudoscalar vertex.

We will now determine $Z_{\text{tw}\to m_f}$ and test the accuracy to which the ratio given in Eq. (6.12) defines a unique constant by studying the ratio of two types of matrix elements. In the first we examine simple two-point correlators between each of the pseudoscalar densities in Eq. (6.12)

and the operator $O_\pi(t)$ which creates a pion from a Coulomb gauge fixed wall source located at the time t:

$$\mathcal{R}_\pi(t) = \frac{\left\langle \sum_{\vec{x}} \overline{\Psi}(\vec{x},t) R_5 \gamma_5 \Psi(\vec{x},t) O_\pi(0) \right\rangle}{\left\langle \sum_{\vec{x}} \overline{\psi}(\vec{x},t) \gamma_5 \psi(\vec{x},t) O_\pi(0) \right\rangle}, \tag{6.13}$$

which for large t is the ratio of matrix elements of our two pseudoscalar operators between a pion state and the vacuum. Results are presented in Table 6.1.

#	β	T (MeV)	$\mathcal{R}_\pi$
2	1.70	0	1.774(5)
3	1.75	0	1.570(4)
7	1.82	0	1.397(2)
9	1.671	149	1.905(6)
10	1.671	149	1.980(7)
11	1.707	159	1.725(8)
12	1.740	168	1.631(11)
13	1.771	177	1.476(4)
14	1.801	186	1.439(3)
15	1.829	195	1.365(3)

Table 6.1: Values for the renormalization factor $Z_{\mathrm{tw}\to m_f}$ obtained from the ratio of pseudoscalar correlators $\mathcal{R}_\pi$ defined in Eq. (6.13).

Second we examine off-shell, three-point Green's functions evaluated in Landau gauge which again contain each of the pseudoscalar densities being compared and a quark and an anti-quark field carrying momenta p_1 and p_2, allowing us to see the degree to which the ratio in Eq. (6.12) does not depend on the small external momenta p_1 and p_2.

$$\mathcal{R}_{\mathrm{MOM}}(p_1,p_2) = \frac{\mathrm{Tr}\left\langle \sum_{x_2,x_1} e^{i(p_2 x_2 - p_1 x_1)} \psi(x_2) \overline{\Psi}(0) R_5 \gamma_5 \Psi(0) \overline{\psi}(x_1) \right\rangle}{\mathrm{Tr}\left\langle \sum_{x_1,x_2} e^{i(p_2 x_2 - p_1 x_1)} \psi(x_2) \overline{\psi}(0) \gamma_5 \psi(0), \overline{\psi}(x_1) \right\rangle}. \tag{6.14}$$

Here we are using the well-studied methods of Rome/Southampton non-perturbative renormalization [130] to compare the normalizations of the operators $\overline{\Psi} R_5 \gamma_5 \Psi$ and $\overline{\psi}\gamma_5\psi$. For a recent application of this method to other operators in a DWF context see Ref. [131]. For both Eqs. (6.13) and (6.14), we expect the ratio to be independent of t and of p_1 and p_2 and to yield the same value $Z_{\mathrm{tw}\to m_f}$.

When evaluating the momentum space Green's functions in Eq. (6.14) we generate the needed quark propagators using a series of volume sources [132]. For each specific four-momentum p we evaluate twelve propagators, one for each spin and color, using the sources

$$\eta(x,p)_{\alpha,a;\beta,b} = e^{ip\cdot x}\delta_{\alpha\beta}\delta_{ab}, \tag{6.15}$$

where α and a are the spin and color indices of the source η while β and b label the spins and colors of the twelve sources evaluated for each four-momentum p. We perform our calculation using both non-exceptional kinematics, $p_1^2 = p_2^2 = (p_1 - p_2)^2$, and exceptional kinematics, $p_1 = p_2$. Results for the ratios $\mathcal{R}^{\text{non-ex}}_{\text{MOM}}(p_1,p_2)$ and $\mathcal{R}^{\text{ex}}_{\text{MOM}}(p_1,p_2)$ for the three zero-temperature ensembles are presented in Table 6.3 and Fig. 6.1. The specific momentum components used to construct p_1 and p_2 are listed in Table 6.2.

The ratios presented in Tables 6.1 and 6.3 and plotted in Fig. 6.1 at a given value of β are all expected to equal the common renormalization factor $Z_{\mathrm{tw}\to m_f}$. However, as is evident from these tables and figure this expectation is realized at only the 20% level, suggesting the presence of significant $O\left((pa)^2\right)$ errors and implying a similar uncertainty in extracting a consistent value for the important quantity $Z_{\mathrm{tw}\to m_f}$. In fact, the behavior of these results is consistent with an $O\left((pa)^2\right)$ origin for these discrepancies. The larger dependence on momentum of the non-exceptional ratio $\mathcal{R}^{\text{non-ex}}_{\text{MOM}}(p_1,p_2)$ than seen in $\mathcal{R}^{\text{ex}}_{\text{MOM}}(p_1,p_2)$ and its larger deviation from the more consistent quantities $\mathcal{R}^{\text{ex}}_{\text{MOM}}(p_1,p_2)$ and $\mathcal{R}_\pi$ is reasonable since the non-exceptional kinematics were originally introduced to ensure that large momenta flow everywhere in the corresponding Green's function [131]. The better agreement between the quantities $\mathcal{R}^{\text{ex}}_{\text{MOM}}(p_1,p_2)$ and $\mathcal{R}_\pi$ and the smaller momentum dependence of $\mathcal{R}^{\text{ex}}_{\text{MOM}}(p_1,p_2)$ is

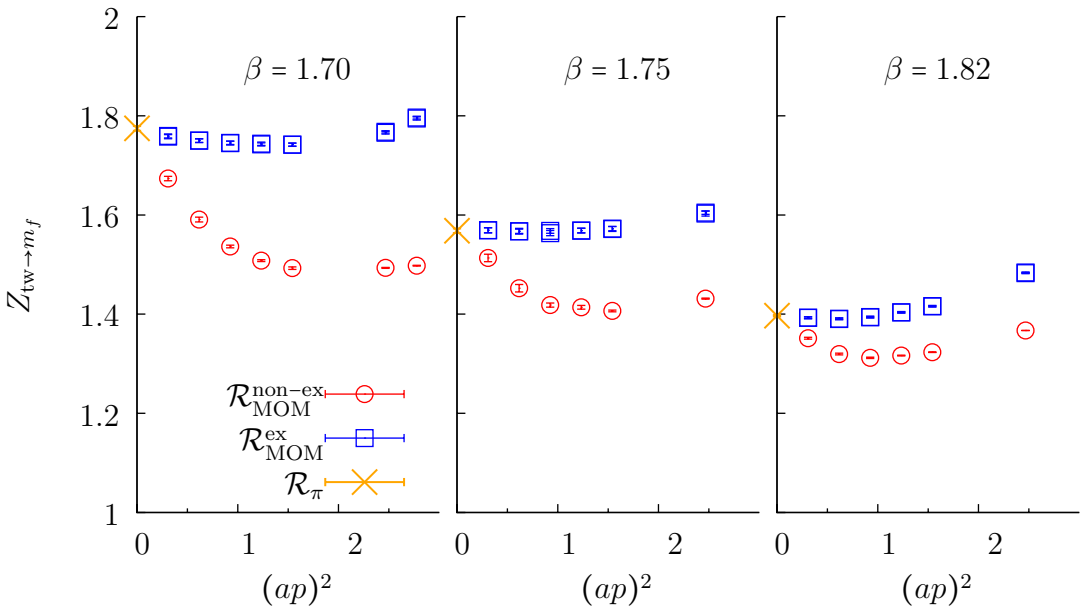

Figure 6.1: Plots of the results for the quantity $Z_{\mathrm{tw}\to m_f}$ given in Tables 6.1 and 6.3 for each of the three values of β that were studied at zero temperature. The single value of $\mathcal{R}_\pi$ is plotted as an "×" in each panel and given the value $(pa)^2 = 0$. (The scale on the left-most y-axis applies to all three plots.) As discussed in the text, the discrepancies between $\mathcal{R}_{\mathrm{MOM}}^{\text{non-ex}}$ and $\mathcal{R}_{\mathrm{MOM}}^{\text{non-ex}}$ are indicative of $O\left((pa)^2\right)$ errors, so we use the value of $\mathcal{R}_\pi$ for $Z_{\mathrm{tw}\to m_f}$.

$(pa)^2$	$p_A L/2\pi$	$p_B L/2\pi$
0.308	(1,1,0,0)	(0,1,1,0)
0.671	(1,1,1,1)	(1,1,1,-1)
0.925	(2,1,1,0)	(2,0,-1,1)
1.234	(2,2,0,0)	(0,2,2,0)
1.542	(2,2,1,1)	(2,-1,2,1)
2.467	(2,2,2,2)	(2,2,2,-2)
2.776	(3,2,2,1)	(3,2,-1,-2)

Table 6.2: The components of the two momentum four-vectors p_A and p_B used to compute the quantities $\mathcal{R}_{\rm MOM}(p_1, p_2)$ given in Table 6.3. For non-exceptional momenta, we use $p_1 = p_A$ and $p_2 = p_B$, while for exceptional momenta, only a single momentum, either $p_1 = p_2 = p_A$ or $p_1 = p_2 = p_B$ is used. Here $L = 16$ is the spatial size of the lattice.

also consistent with the smaller internal momenta expected in these Green's functions with exceptional kinematics. Finally the decreasing differences between these three quantities as β increases from 1.70 to 1.82 with the corresponding decrease in a is also consistent with these violations of universality arising from finite lattice spacing errors.

We therefore adopt the hypothesis that the discrepancies between these different determinations of $Z_{\rm tw\to m_f}$ arise from finite lattice spacing effects and that the most reliable value for $Z_{\rm tw\to m_f}$ will be obtained at smallest momentum. Hence, we use the ratio $\mathcal{R}_\pi$ to provide values for $Z_{\rm tw\to m_f}$. This choice has the additional benefit that we have evaluated this ratio on the finite temperature ensembles allowing us to use $\mathcal{R}_\pi$ to provide values of $Z_{\rm tw\to m_f}$ for each of our values of β, avoiding extrapolation. Note that the discrepancy between the finite and zero temperature results for $\mathcal{R}_\pi$ shown in Table 6.1 for the near-by β values $\beta = 1.700, 1.707$ and $\beta = 1.820, 1.829$ indicate remaining systematic a^2 errors in our determination of $Z_{\rm tw\to m_f}$ that are on the order of 5%.

	$\beta = 1.70$		$\beta = 1.75$		$\beta = 1.82$	
$(pa)^2$	$\mathcal{R}^{\text{non-ex}}_{\text{MOM}}$	$\mathcal{R}^{\text{ex}}_{\text{MOM}}$	$\mathcal{R}^{\text{non-ex}}_{\text{MOM}}$	$\mathcal{R}^{\text{ex}}_{\text{MOM}}$	$\mathcal{R}^{\text{non-ex}}_{\text{MOM}}$	$\mathcal{R}^{\text{ex}}_{\text{MOM}}$
0.308	1.673(5)	1.759(4)	1.507(5)	1.566(4)	1.352(2)	1.393(2)
0.617	1.591(5)	1.745(4)	1.450(5)	1.562(4)	1.320(2)	1.390(2)
0.925	1.536(3)	1.745(3)	1.418(3)	1.562(4)	1.312(1)	1.394(2)
1.234	1.508(2)	1.744(3)	1.412(2)	1.564(4)	1.3165(7)	1.404(1)
1.542	1.493(2)	1.742(3)	1.406(1)	1.570(4)	1.3233(6)	1.416(1)
2.467	1.4933(10)	1.766(3)	1.4313(7)	1.613(3)	1.3670(4)	1.484(1)
2.776	1.4977(8)	1.796(3)	-	-	-	-

Table 6.3: Values for the ratio $\mathcal{R}_{\text{MOM}}(p_1, p_2)$ defined in Eq. (6.14). For non-exceptional momenta, the quantity $\mathcal{R}^{\text{non-ex}}_{\text{MOM}}(p_1 = p_A, p_2 = p_B)$ is shown. For exceptional momenta, the average of $\mathcal{R}^{\text{non-ex}}_{\text{MOM}}(p_1 = p_2 = p_A)$ and $\mathcal{R}^{\text{non-ex}}_{\text{MOM}}(p_1 = p_2 = p_B)$ is shown. The first column shows the value of $(p_1 a)^2 = (p_2 a)^2 = (pa)^2$. Results from 12, 20 and 21 configurations have been averaged to give the values for $\beta = 1.70, 1.75$ and 1.82, respectively. The quark mass values and lattice sizes used for these results are given in Table 6.1. The significant variation among the results for a given value of β indicate large $O\left((pa)^2\right)$ errors.

6.2.3 Normalization Conventions

Using the methods described above, we can convert our results for the quark mass, chiral condensate, and Dirac spectrum into a single normalization scheme, allowing a meaningful comparison between the eigenvalues in the Dirac spectrum and the corresponding quark mass. We adopt the commonly-used $\overline{\text{MS}}$ scheme, normalized at a scale $\mu = 2$ GeV.

We use the DWF results for the continuum, $\mu = 2$ GeV, $\overline{\text{MS}}$ quark masses determined in Ref. [112], $m_s^{\overline{\text{MS}}}(2\text{ GeV}) = (96.2 \pm 2.7)$ MeV and $m_{ud}^{\overline{\text{MS}}}(2\text{ GeV}) = (3.59 \pm 0.21)$ MeV and the accurate linear dependence of m_π^2 and m_K^2 on the quark masses in the region studied to convert a lattice light quark mass, $\widetilde{m}_l = m_f + m_{\text{res}}$ corresponding to a pion mass $m_\pi(\widetilde{m}_l)$ into this same $\overline{\text{MS}}$ scheme using the relation:

$$m_l^{\overline{\text{MS}}}(2\text{ GeV}) = (3.59 + 96.2)\text{ MeV}\frac{\Big(m_\pi(\widetilde{m}_l)\Big)^2}{2(m_K)^2}, \tag{6.16}$$

where $m_K = 495$ MeV denotes the physical value of the Kaon mass. The renormalization factor is then given by:

$$Z_{m_f \to \overline{\text{MS}}} = \frac{99.79\text{ MeV}}{2\widetilde{m}}\left(\frac{m_\pi(\widetilde{m}_l)}{495\text{ MeV}}\right)^2 \tag{6.17}$$

for each of our ensembles. Note the lattice quark mass, $\widetilde{m}$, substituted in Eq. (6.17) must be expressed in units of MeV to define a conventional, dimensionless value for $Z_{m_f \to \overline{\text{MS}}}$. The resulting $Z_{m_f \to \overline{\text{MS}}}$ factors for each β value and the associated ensembles are given in Table 6.4.

The factors given in Table 6.4 will also be used to convert values of the chiral condensate $\overline{\psi}\psi$ (when constructed from the usual 4-D surface, lattice operators), a variety of susceptibilities and Dirac spectrum (when normalized with the same conventions as $\overline{\psi}\psi$) into $\mu = 2$

#	T (MeV)	$Z_{m_f\to\overline{\rm MS}}(2\text{ GeV})$
8, 21, 29, ...	139	1.47(14)
10, 22, 30, ...	149	1.49(10)
31, ...	154	1.50(9)
11, 23, 32, ...	159	1.51(7)
24, 33, ...	164	1.52(7)
12, 25, 34, ...	168	1.53(6)
13, 26, 35, ...	177	1.55(6)
14, 27, 36, ...	186	1.57(7)
15, 28, 37, ...	195	1.58(9)

Table 6.4: Results for the factors $Z_{m_f\to\overline{\rm MS}}(2\text{ GeV})$ which convert a lattice quark mass, $\widetilde{m}$ into a mass normalized in the $\overline{\rm MS}$ conventions at $\mu = 2$ GeV.

GeV, $\overline{\rm MS}$ values according to the relations:

$$(\overline{\psi}\psi)^{\overline{\rm MS}} = \frac{(\overline{\psi}\psi)^{\rm lat}}{Z_{m_f\to\overline{\rm MS}}} \tag{6.18}$$

$$\chi^{\overline{\rm MS}} = \frac{\chi^{\rm lat}}{Z^2_{m_f\to\overline{\rm MS}}} \tag{6.19}$$

$$\rho(\lambda)^{\overline{\rm MS}} = \frac{\rho^{\rm lat}(\lambda/Z_{m_f\to\overline{\rm MS}})}{Z_{m_f\to\overline{\rm MS}}}. \tag{6.20}$$

Of course, because the quark masses and lattices scales that we use are interpolated and extrapolated from only three zero temperature ensembles, there is significant uncertainty in our determination of the renormalization factors. And it is strongly correlated with the lattice scale when we determine the line of constant physics in Eq. (4.1) in Chap .4. However, since this renormalization factor $Z_{m_f\to\overline{\rm MS}}$ is a smooth uniform value within the region under our investigation, we believe that these renormalization factors in Table 6.4 have sufficient accuracy for the purposes of the present report.

6.3 Computation of the Low-lying Eigenvalue Distribution of the DWF

As much information concerning the symmetry breaking and restoration for the QCD phase transition is contained in the low-lying part of the eigenvalue spectrum of the Dirac operator, we will be focusing on collecting the lowest $N_{\text{eig}} = 100$ eigenvalues of the 5-d Hermitian DWF Dirac operator $D_H = R_5\gamma_5 D_{\text{DWF}}$. Here R_5 performs a simple reflection in the fifth dimension, taking the point (x, s) to the point $(x, L_s - 1 - s)$, where x is the space-time coordinate and $0 \le s \le L_s - 1$ the coordinate in the fifth dimension. The input light quark mass we used in the eigenvalue calculation is the same as that was used in the ensemble evolution.

The Dirac operator is a vast sparse matrix. To utilize and preserve the structure of the Dirac matrix, the class of Krylov space solvers is preferred for calculating the eigenvalues. In this work, we adopt the following two diagonalization methods in our eigenvalue finding tasks:

1. An improved Ritz method proposed by Kalkreuter and Simma [133]. We accomplished most of our computations for eigenvalues with this method.

2. An implicitly restarted Lanczos algorithm proposed in [134, 135] and implemented by our UK colleagues [136, 137].

6.3.1 Ritz and Kalkreuter-Simma Method

Ritz algorithm computes one by one the low-lying eigenvalues by minimizing the Ritz functional

$$\mu(\Psi) = \frac{\langle\Psi|D_H^2|\Psi\rangle}{\langle\Psi|\Psi\rangle} \tag{6.21}$$

with a conjugate gradient method in a sequence of subspaces orthogonal to the space spanned by the eigenvectors that have already been identified. Here the positive-definite operator D_H^2 is used as the kernel instead of D_H to ensure the convergence. Theoretically, if the minimization and the projection operations are exact for every eigenvector, a single iteration of the algorithm would give accurate results.

Nevertheless, in practical numerical calculations, small imprecision in the early steps can finally lead to a large deviation or even incorrect results. The final convergence of N_{eig} eigenvectors usually requires too high a precision when N_{eig} is large. Kalkreuter and Simma [133] proposed to alternate the CG searches for eigenvectors with an intermediate diagonalization for the $N_{\text{eig}} \times N_{\text{eig}}$ Hermitian matrix

$$\langle \Psi_i | D_H^2 | \Psi_j \rangle , \qquad i, j = 1, 2, 3, \ldots, N_{\text{eig}}. \tag{6.22}$$

This is a dense matrix and its diagonalization is realized with iterations of Jacobi transformations. The transformed N_{eig} trial eigenvectors are then sent back to another sequence of CG minimization. Kalkreuter and Simma proved that the alternate minimization in the global space and diagonalization in the subspace will accelerate the overall convergence of the algorithm, and a rigorous bound can be derived from the last CG iteration.

The kernel in the minimization, D_H^2, however, introduces extra degeneracies. An eigenvector of D_H^2 is not necessarily the eigenvector of D_H, but could be a linear combination of two almost degenerate eigenvectors with eigenvalues of opposite signs.

Replacing D_H^2 with D_H in the Jacobi diagonalization step would resolve the degeneracy if the whole degenerate subspace is within the $N_{\text{eig}} \times N_{\text{eig}}$ subspace. However, a "spurious eigenmode" problem may arise if only one of the paired eigenvectors is included in the solved subspace. We can resolve this problem by applying D_H to the problematic vector and project out one of the unnecessary component. The coefficient in the projection can be determined if we know the corresponding eigenvalue of D_H, for which we use the square-root of the corresponding eigenvalue for D_H^2 as a proxy. However, this remedy is not precise.

Fortunately, these spurious modes are always at the high-energy end and the number of these spurious modes is bounded by the degeneracy and is thus usually much smaller than N_{eig}. Therefore we are able tolerate the inaccuracy caused by the spurious modes.

Because the intermediate Jacobi transformations on the dense matrix is inefficient and cannot be easily parallelized, the Kalkreuter and Simma Ritz algorithm suffers from a severe performance loss when N_{eig} is large. We later switched to the implicit restarted Lanczos algorithm as we adopted the bagel/bfm package and our major computation resource changed to BG/Q from QCDOC and BG/L.

6.3.2 Implicitly Restarted Lanczos Algorithm

This Lanczos algorithm is a simplified version for Arnoldi algorithm [138] in that it applies for a Hermitian matrix H. Through iterations involving matrix multiplication and linear algebra, it transforms H to a truncated tridiagonal matrix T_K,

$$T_K = V_K^\dagger H V_K, \tag{6.23}$$

whose eigenvalues are approximates for those of H. Since T_K is usually of a much smaller size $(K \times K)$ than H, it can be diagonalized using the QR algorithm or other algorithms that are suitable for a small dense matrix.

Generally speaking, the Lanczos algorithm is much more efficient than the Ritz algorithm. However, due to loss of orthogonality during the iteration process, it is very likely to produce "spurious modes" in numerical calculations. Usually, one should restart the iteration after some steps by using a new starting vector, which removes or reduces the components in the eigen-space that has already been obtained. But it may lose the information contained in the residual vector. Refs. [134, 135] proposed a scheme that corrects for the loss of orthogonality without explicitly constructing a restarting vector.

The details of the properties and the implementation of the implicitly restarted Lanczos algorithm is described in depth in Refs. [135, 136] together with some improvements. We

will not repeat them here.

6.3.3 Summary of the Results

In Table 6.5, we summarize the number of configurations we used in the calculation of the eigenvalue spectrum for each finite temperature ensemble with volume $16^3 \times 8$ and $32^3 \times 8$ as well as a 16^4 zero temperature ensemble.

Also presented in this table is the $\mathcal{R}_\pi \overline{\Lambda}_0$, the average smallest renormalized eigenvalue. Here, Λ denotes an eigenvalue of the full Hermitian DWF Dirac operator. These eigenvalues include the effect of the quark mass and in the continuum limit would have the form:

$$\Lambda = \sqrt{\lambda^2 + \widetilde{m}_l^2}. \tag{6.24}$$

In the continuum theory the mass is conventionally removed from the Dirac operator before its eigenvalues are determined so that the usual eigenvalue distribution is given for the quantity λ in Eq. (6.24). In our case, the transformation to this more usual eigenvalue distribution requires converting each eigenvalue Λ_n into a corresponding $\lambda_n = \sqrt{\Lambda_n^2 - \widetilde{m}_l^2}$. Unfortunately, this step is vulnerable to finite lattice spacing effects which allow an occasional value of Λ_n to be smaller than $\widetilde{m}_l$, leading to an unphysical, imaginary result for λ_n. This should become increasingly rare in the limit $a \to 0$ of vanishing lattice spacing. In this limit, the quantity $\widetilde{m}_l$ accurately corresponds to the light quark mass describing the long distance physics determined by our lattice theory. Likewise, the arguments following Ref. [128] given in the appendix of Ref. [35] imply that in this limit, the spectral density $\rho(\Lambda)$ also approaches a continuum limit which requires $\Lambda \geq \widetilde{m}_l$.

On the othere hand, the total number modes is proportional to the lattice volume. Therefore, with fluctuations, the number of the "unphysical" modes are also proportional to the volume. This is represented by a much lower $\mathcal{R}\overline{\Lambda}_0$ at a larger volume in Table 6.5. For $T \leq 168$ MeV with $32^3 \times 8$ volume, $\mathcal{R}\overline{\Lambda}_0 \lessapprox \widetilde{m}_l$, indicating an appreciable amount of un-

physical modes. In the following section, we will introduce an graphical illustration that accommodates these modes.

		16^3			32^3		
T (MeV)	$\widetilde{m}_l$	#	$N_{\rm cfg}$	$\mathcal{R}_\pi\overline{\Lambda}_0$	#	$N_{\rm cfg}$	$\mathcal{R}_\pi\overline{\Lambda}_0$
149	0.00464	9	340	0.00632	22	158	0.00361
149	0.00469	10	340	0.00606			
159	0.004211	11	408	0.00828	23	109	0.00366
168	0.00395	12	239	0.01334	25	83	0.00409
177	0.00367	13	246	0.02170	26	170	0.00483
186	0.00341	14	374	0.03131	27	171	0.01126
195	0.00314	15	1140	0.03837	28	76	0.01457
-	0.00488	3	252	0.00489			

Table 6.5: List of the number of configurations used in the Dirac spectrum calculation for both the $16^3 \times 8$ and $32^3 \times 8$ ensembles, as well as the results for the average smallest normalized eigenvalue ($\mathcal{R}\overline{\Lambda}_0$). Here $N_{\rm cfg}$ gives the total number of configurations on which the spectrum was determined. The first row of T = 149 MeV represents data from L_s = 32 ensembles while the second from L_s = 48. The last row summarize the data from the zero temperature lattice with volume $16^3 \times 16$.

6.4 Normalized Spectral Density: A Showcase at $T = 0$

The results for the Dirac spectrum at finite temperature obtained using these methods will be presented and analyzed in Sec. 6.5, 6.6 and 6.7, where the restorations of chiral and $U_A(1)$ symmetries are studied. In this section we examine the Dirac spectrum obtained on the zero temperature ensemble labeled # 3, with volume 16^4 and β = 1.75.

The discussion in the present section has three objectives. First we explicitly apply the normalization factors to convert the bare eigenvalues of the DWF Dirac operator into the $\overline{\text{MS}}$ scheme. The resulting spectral density is expressed in physical units and can easily be compared with both physical and simulated $\overline{\text{MS}}$ values of the quark masses as well as with the QCD scale, $\Lambda_{QCD} \sim 300$ MeV. Second, we convert the spectrum of the Hermitian DWF Dirac operator, which includes the effects of the non-zero quark masses to the more conventional spectrum from which the mass has been removed, a step which depends critically on the normalization procedure and is sensitive to finite lattice spacing errors. Finally we examine the Banks-Casher relation between the resulting spectrum and the chiral condensate.

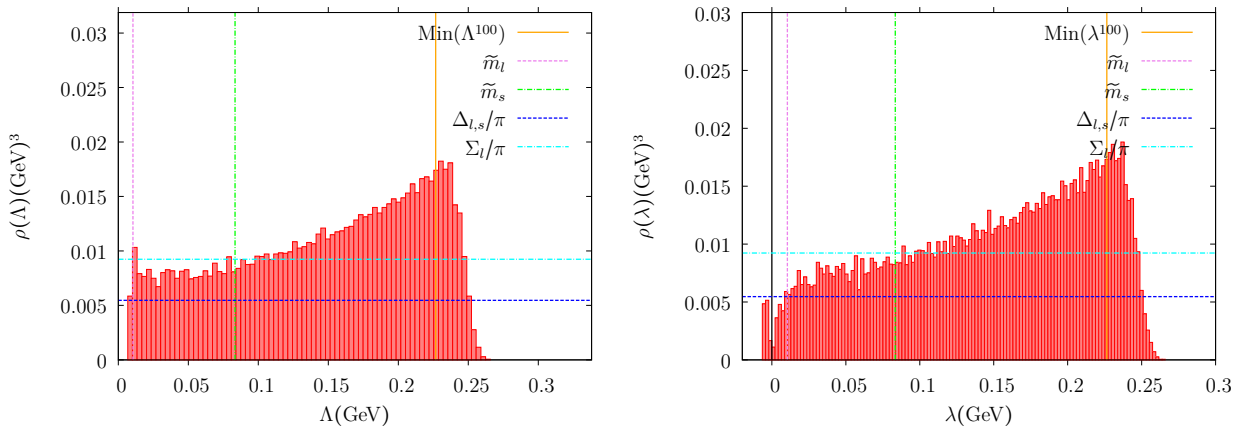

Figure 6.2: Histogram of the spectrum of eigenvalues Λ of the Hermitian DWF Dirac operator normalized in the $\overline{\text{MS}}$ scheme at the scale $\mu = 2$ GeV (left). These eigenvalues are calculated on the zero-temperature ensemble run # 3. The right hand panel shows a histogram of the eigenvalues $\lambda = \sqrt{\Lambda^2 - \widetilde{m}_l^2}$ from which the quark mass has been removed. In this panel, the region $\lambda > 0$ shows those values for which $\Lambda^2 > \widetilde{m}_l^2$, *i.e.*, λ is purely real, a condition that should be obeyed in the continuum limit. The region $\lambda < 0$ shows those eigenvalues with $\Lambda^2 < \widetilde{m}_l^2$, *i.e.*, λ pure imaginary, plotted on the negative part of the x-axis as $\lambda = -|\sqrt{\Lambda^2 - \widetilde{m}_l^2}|$. These unphysical values give a visible measure of the finite lattice spacing distortions to the region of small $\lambda > 0$.

Fig. 6.2 shows histograms of the Dirac eigenvalues measured on 252 configurations from the zero-temperature, 16^4 ensemble run # 3 in Table 6.5. In the left-hand panel of this figure, the histogram of eigenvalues Λ is obtained by converting the eigenvalues of the lattice DWF Dirac operator, as described above, to the $\overline{\rm MS}$ scheme with $\mu = 2$ GeV. On each configuration the 100 eigenvalues of smallest magnitude have been determined. Fig. 6.2 shows histograms of these 25,200 eigenvalues. The rightmost vertical line in both panels identifies the minimum value from the set of the 100th largest eigenvalues on each of the 252 configurations. For eigenvalues less than this "minmax" value the histogram accurately represents the complete spectrum, undistorted by our cutoff of 100 eigenvalues per configuration.

The left-hand panel of Fig. 6.2 demonstrates the effect of using a consistent normalization scheme for the quark masses. The two left-most vertical lines in that plot correspond to the simulated light and strange quark masses, $\widetilde{m}_l$ and $\widetilde{m}_s$, in the same $\overline{\rm MS}$ normalization. The expected coincidence between the peak in the Λ distribution at the smallest eigenvalues and the vertical line representing the light quark mass occurs only after the relative normalization $\mathcal{R} = 1.570$ from Table 6.1 between the DWF operator and the conventional input quark mass discussed above has been applied.

As has been discussed in the previous section, in the calculation presented here the lattice spacing a is relatively large and deviations from the inequality $\Lambda \geq \widetilde{m}_l$ should be expected. In order to present the more conventional eigenvalue distribution $\rho(\lambda)$ while at the same time displaying the imperfections arising from finite a, we choose to plot the eigenvalue histograms in a hybrid form. For each of the original eigenvalues Λ we compute the derived eigenvalue $\lambda_n = \sqrt{\Lambda^2 - \widetilde{m}_l^2}$. If λ_n is real, it is included in the histogram in the normal way, along the positive x-axis. However, if λ_n is imaginary it is displayed in the same histogram along the negative x-axis in a bin corresponding to $-|\lambda|$.

This has been done in the right-hand panel of Fig. 6.2. The histogram for $\lambda > 0$ is the conventional eigenvalue distribution, normalized in the $\mu = 2$ GeV, $\overline{\rm MS}$ scheme. The

histogram bins for $\lambda < 0$ are unphysical and directly result from finite lattice spacing artifacts. By showing both on the same plot, we make it easy to recognize the magnitude of the errors inherent in $\rho(\lambda), \lambda > 0$ introduced by lattice artifacts. For example, it is likely that a majority of the gap in $\rho(\lambda)$ for λ positive but near zero in the right-hand panel of Fig. 6.2 would be filled in as $a \to 0$ by the imaginary values of λ plotted as $-|\lambda| < 0$, and should not be attributed to the effects of finite volume.

An interesting test of these methods can be made by comparing the spectrum shown in the right-hand panel of Fig. 6.2 with the predictions of the Banks-Casher formula which relates the eigenvalue density $\rho(\lambda)$ at $\lambda = 0$ and the chiral condensate Σ_l when both are evaluated in the limit of infinite volume and vanishing quark mass, as in Eq. (6.1) or abbreviated as follows

$$\Sigma_l = \pi\rho(0). \tag{6.25}$$

The right- and left-hand sides of Eq. (6.25) can be compared by examining the right-hand panel of Fig. 6.2 where we have superimposed the quantity Σ_l/π as horizontal lines on the histogram. Also shown is the subtracted chiral condensate $\Delta_{l,s}$ defined in Eq. (5.4), which attempts to partially remove the ultraviolet divergent contribution to the chiral condensate in proportion to m/a^2. The right panel of Fig. 6.2 shows that $\rho(0)$ tends to agree well with $\Delta_{l,s}$ if we take a linear extrapolation for the $\rho(\lambda)$ as $\lambda \to 0$. Although neither the infinite volume nor the chiral limits are taken, and $\Delta_{l,s}$ does not perfectly eliminate the large term proportional to m, this agreement still serves as a good indication for our success in renormalizing the eigenvalue spectrum. More about the Banks-Casher relation reflected in the low-lying eigenvalue distribution will be touched on in a quantitative way in Sec. 6.6.

6.5 Renormalized Eigenvalue Distributions at Finite Temperature

Fig. 6.3 shows the distributions, renormalized in the $\overline{\rm MS}$ scheme at the scale $\mu = 2$ GeV, determined from the lowest 100 eigenvalues (λ) for six ensembles at temperatures from 149 MeV to 195 MeV. The eigenvalue densities for the $32^3 \times 8$ space-time volumes are plotted as solid histograms, while the $16^3 \times 8$ results are plotted as black, solid lines. The aforementioned imaginary, "unphysical" modes are plotted as $-\sqrt{|\Lambda^2 - \widetilde{m}_l^2|}$ on the negative axis. The values for the total mass of light and strange quarks, $\widetilde{m}_l^{\overline{\rm MS}}$ and $\widetilde{m}_s^{\overline{\rm MS}}$, are indicated by vertical dashed lines, which give a physical scale for the eigenvalue distribution. Since we have determined only a fixed number of eigenvalues, the spectral distributions will be distorted at their upper ends. The third vertical dashed line in these plots, which appears with various x-coordinates, locates the smallest value for λ_{100} found for each ensemble. The spectrum shown to the left of this line will then be undistorted by our failure to include larger eigenvalues in the figure.

Since the number of eigenmodes is proportional to the space-time volume, a fixed number of the lowest modes will become more concentrated at the lower-end of the spectrum as the volume increases. This phenomena can be easily seen in Fig. 6.3 where the range of eigenvalues studied decreases dramatically as the space-time volume is increased from $16^3 \times 8$ to $32^3 \times 8$. However, while the range of eigenvalues covered by the larger $32^3 \times 8$ volume is reduced, this larger volume provides a better sampling and more convincing view of the spectrum near zero, the region of greatest interest.

For $T = 149$ and 159 MeV, the eigenvalue distributions can be characterized as a linear function with a non-vanishing intercept for eigenvalues of order 10 MeV or larger. Below 10 MeV the spectrum is distorted by a combination of finite volume and residual chiral symmetry breaking effects. The non-vanishing intercept, interpreted through the Banks-Casher relation, is consistent with the non-vanishing chiral condensate and vacuum chiral symmetry

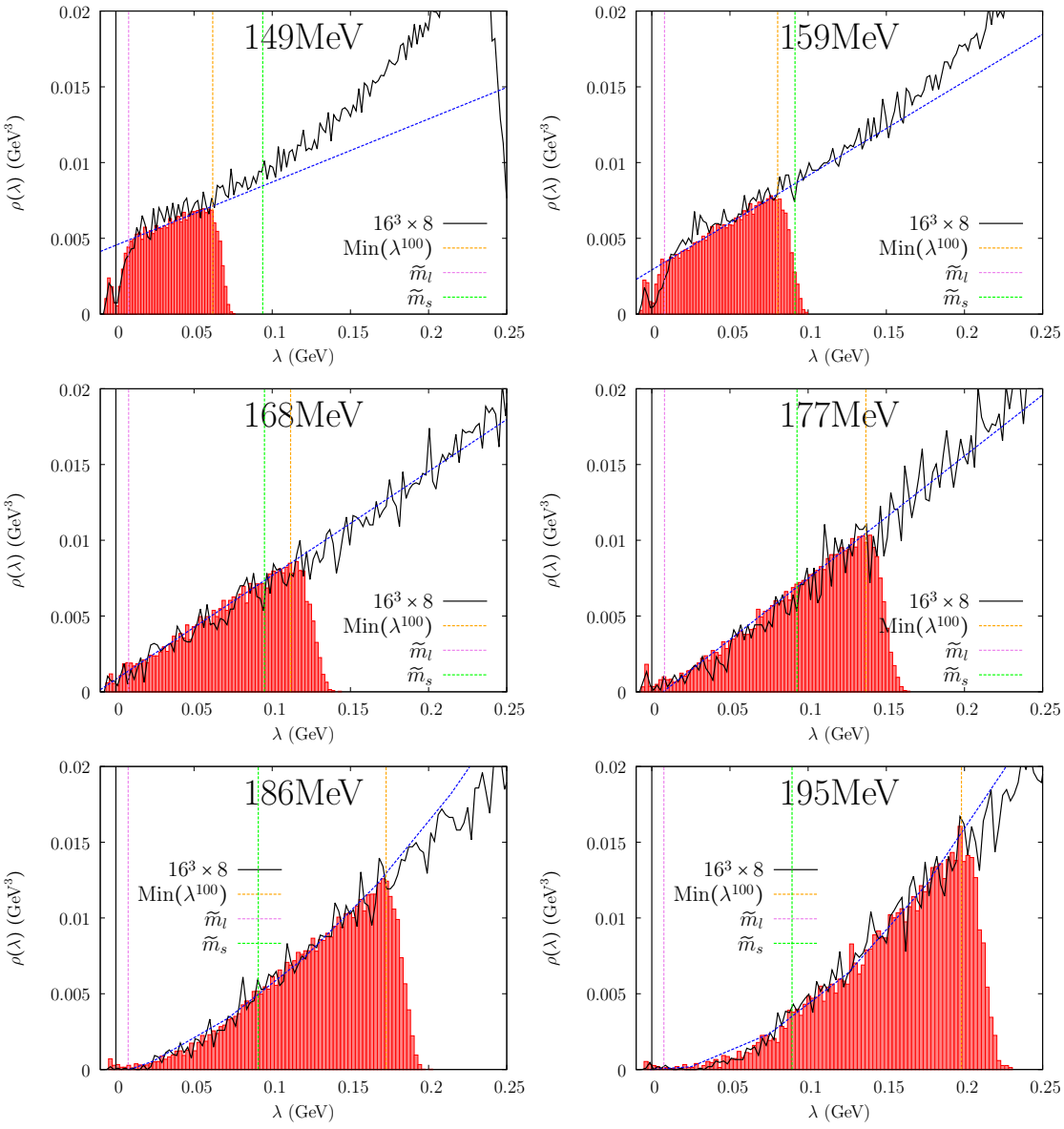

Figure 6.3: The eigenvalue spectrum for $T = 149 - 195$ MeV, expressed in the $\overline{\text{MS}}$ scheme at the scale $\mu = 2$ GeV. The imaginary, "unphysical" eigenvalues are plotted as $-\sqrt{|\Lambda^2 - \widetilde{m}_l^2|}$. The spectra from the $32^3 \times 8$ ensembles are plotted as histograms and fit with a linear ($T = 149 - 178$ MeV) or a quadratic ($T = 186 - 195$ MeV) function (blue dashed line). The spectrum from each of the $16^3 \times 8$ ensembles is plotted as a black solid line.

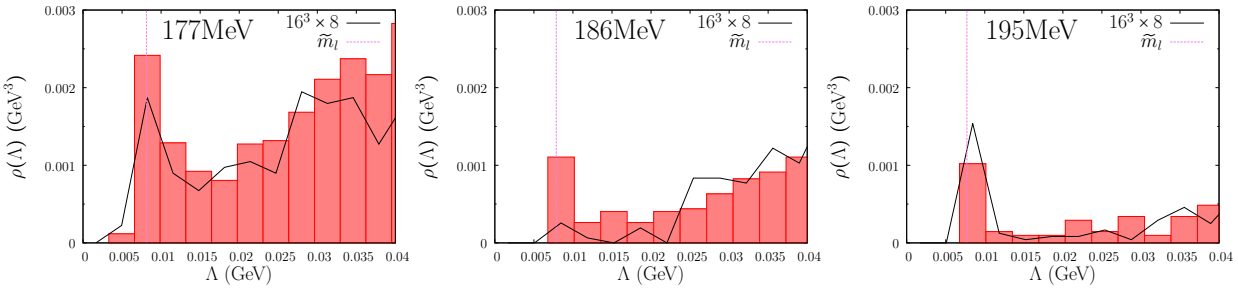

Figure 6.4: (Left to right) The renormalized eigenvalue spectrum for T = 177 – 195 MeV without the removal of the bare quark mass. The statistics are likely insufficient for 186 MeV on the $16^3 \times 8$ ensemble; only 5 instances of "near-zero modes" are collected.

breaking observed at these temperatures which lie below the pseudo-critical temperature.

For T = 168 MeV, the linear behavior continues to be visible, but the intercept has essentially vanished, suggesting that 168 MeV is close to the pseudo-critical temperature for $m_\pi \approx 200$ MeV, consistent with the temperature dependence of the $SU(2)_L \times SU(2)_R$-breaking susceptibility difference $\chi_\pi - \chi_\sigma$ shown in Fig. 5.6.

For T = 177 MeV, a small peak in $\rho(\lambda)$ near the origin emerges as a cluster of near-zero modes. Such a cluster of near-zero modes might result from the Atiyah-Singer theorem and non-vanishing topological charge or from the dilute instanton gas approximation (DIGA). As is discussed below, the volume dependence of this peak and the distribution of the chirality of these modes is consistent with the DIGA and inconsistent with their arising from non-zero global topology. This small eigenvalue region can be best seen in the expanded view given in Fig. 6.4.

For T = 186 and 195 MeV, this small peak survives although it diminishes in size with increasing temperature. In addition, the peak becomes increasingly separated from the rest of the spectrum by a gap containing few eigenvalues. As a result the remainder of the spectrum, excluding this peak, can no longer be fit using a linear function. A quadratic fit is possible at T = 186 but an even higher power may be needed to describe the 195 MeV

spectrum.

Fig. 6.5 shows the comparison of renormalized eigenvalue distributions at $T = 149$ MeV with $L_s = 32$ (left) and $L_s = 48$ (right) for the $16^3 \times 8$ ensembles. The consistency of the two distribution is another proof for the equivalence of these two ensembles and the validity of a mild negative input quark mass.

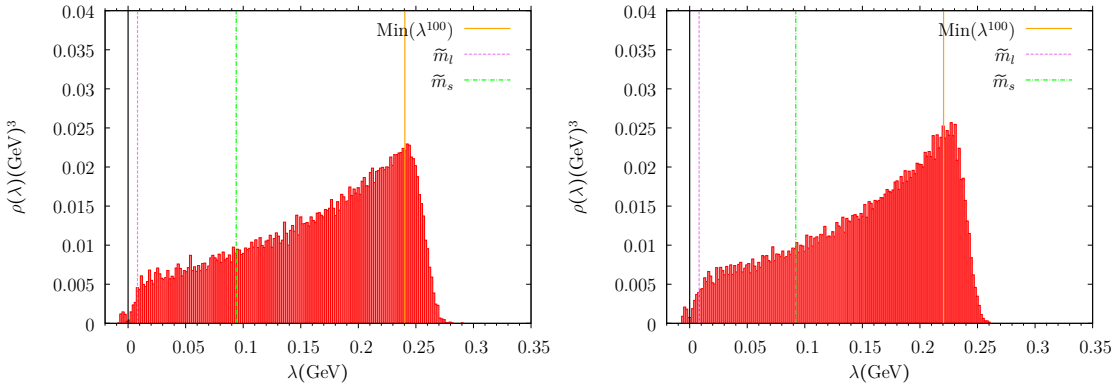

Figure 6.5: The eigenvalue spectrum at $T = 149$ MeV with $L_s = 32$ (left) and $L_s = 48$ (right) for volume $16^3 \times 8$, expressed in the $\overline{\text{MS}}$ scheme at the scale $\mu = 2$ GeV. The imaginary, "unphysical" eigenvalues are plotted as $-\sqrt{|\Lambda^2 - \widetilde{m}_l^2|}$.

6.6 Subtracted Chiral Condensate

It is not difficult to see very approximate agreement between the intercept of the spectral density at $\lambda = 0$ (ignoring obvious distortions to the spectrum near $\lambda = 0$) and the measured value of Σ_l implied by the Banks-Casher relation. However, a careful, quantitative test of Eq. (6.1) must overcome two obstacles: both the finite volume suppression of $\rho(\lambda)$ as $\lambda \to 0$ and the quadratic divergence present in Σ_q for non-zero quark mass. For a DWF calculation such a test is further complicated by the quite different contributions of residual chiral symmetry breaking to Σ_q and to $\rho(\lambda)$ for small λ. As suggested above, all of these

difficulties can be overcome. The first step is to consider the subtracted chiral condensate, $\Delta_{l,s}$ defined in Eq. (5.4). If Eq. (6.1) is used to express $\Delta_{l,s}$ in terms of the spectral density, we obtain the more convergent result:

$$\Delta_{l,s} = \int_0^\infty \mathrm{d}\lambda \rho(\lambda) \frac{2\widetilde{m}_l(\widetilde{m}_s^2 - \widetilde{m}_l^2)}{(\lambda^2 + \widetilde{m}_l^2)(\lambda^2 + \widetilde{m}_s^2)}. \tag{6.26}$$

While this expression still receives a contribution from large eigenvalues, well above the group of low modes studied here, this high-mode contribution is expected to be of order $m_l m_s^2 \ln(m_s a)$ which is possibly 1% of the $(250\ \mathrm{MeV})^3$ value of the zero temperature chiral condensate. Thus, we expect that for our present quark masses and lattice spacing, we can evaluate the right hand side of Eq. (6.26) using our 100 low modes to at least a few percent accuracy, at least for $T \le T_c$.

We can evaluate the integral in Eq. (6.26) using our measured eigenvalues in two ways. First for each measured configuration we can replace the integral over λ on the right hand side of Eq. (6.26) by a sum over the measured eigenvalues. In addition we can express the integrand in Eq. (6.26) in terms of the directly measured eigenvalues Λ_n so that the uncertainties associated with those values of Λ_n lying below $\widetilde{m}_l$ are avoided. The resulting expression for $\Delta_{l,s}$ becomes

$$\Delta_{l,s}^{\mathrm{ms}} = \frac{1}{N_\sigma^3 N_\tau} \left\langle \sum_{n=1}^{100} \frac{\widetilde{m}_l(\widetilde{m}_s^2 - \widetilde{m}_l^2)}{\Lambda_n^2(\Lambda_n^2 + \widetilde{m}_s^2 - \widetilde{m}_l^2)} \right\rangle, \tag{6.27}$$

where $\langle \ldots \rangle$ indicates an average over configurations and we use the notation "ms" (mode sum) to identify the result obtained from this summation over modes.

In the second approach to Eq. (6.26) we replace the spectral density $\rho(\lambda)$ by the fitted expression given in Eq. (6.4) and then perform the integration over λ analytically with the result:

$$\Delta_{l,s}^{\mathrm{eig}} \equiv c_0 \widetilde{m}_l + c_1 \widetilde{m}_l \ln\left(\frac{\widetilde{m}_s^2}{\widetilde{m}_l^2}\right) + c_2 \pi \widetilde{m}_l, \tag{6.28}$$

where terms of order $\widetilde{m}_l/\widetilde{m}_s$ have been neglected and the label "eig" has been introduced to distinguish this expression from those resulting from the three other approaches to the

calculation of this quantity.

In Table 6.6 we compare these two spectral methods for computing $\Delta_{l,s}$ (Eq. (5.4)) with the results from both the direct subtraction of the measured condensates (which we continue to label as $\Delta_{l,s}$) and the improved quantity $\widetilde{\Delta}_{l,s}$ (Eq. (5.34)) which is less contaminated by residual DWF chiral symmetry breaking effects. As can be seen from the table, for the temperatures at which the fit form given in Eq. (6.4) provides a good description of the eigenvalue distribution, 139 MeV $\leq T \leq$ 168 MeV, analytic integration of this three-parameter function and the direct sum over the lowest 100 modes agree reasonably well. This supports the use of the three-parameter function to provide an interpretation of our results. This agreement also suggests that the region $|\Lambda| \lessapprox 10$ MeV, which is distorted in our computed Dirac eigenvalue spectrum by finite volume and residual chiral symmetry breaking effects but treated in a fashion consistent with infinite volume, continuum expectations by the fitting function, does not play a large role in these results. The difference between $\Delta_{l,s}^{\rm eig}$ and $\Delta_{l,s}^{\rm ms}$ can serve as an estimate for the systematic error in the fit coefficients, a difference which at its largest is about 15%.

A second observation that can be drawn from the data in Table 6.6 is that the quantity $\widetilde{\Delta}_{l,s}$ agrees reasonably well with the result obtained directly from the Dirac spectrum over the full temperature range. This suggests that a good representation for the chiral condensate can be obtained by performing the subtraction of light and strange quark Green's functions and that in the case of DWF it is best to use the GMOR relation and subtract connected pseudoscalar susceptibilities rather than the condensates themselves which contain relatively large, uncontrolled residual chiral symmetry breaking effects. We would like to emphasize that our use of the continuum spectral Eq. (6.4) combined with the renormalized DWF spectrum makes strong assumptions about the validity of continuum methods in our lattice calculation at reasonably strong coupling. It is impressive that on the larger 32^3 volume, where the statistical errors are likely most reliable, Table 6.6 shows agreement between $\Delta_{l,s}^{\rm ms}$

and $\widetilde{\Delta}_{l,s}$ consistently at the 1 sigma level, which in some cases represent an accuracy of 4% or less.

#	T (MeV)	N_σ	L_s	$\widetilde{m}_l$	$\widetilde{m}_s$	$\Delta^{\rm eig}_{l,s}/T^3$	$\Delta^{\rm ms}_{l,s}/T^3$	$\Delta_{l,s}/T^3$	$\widetilde{\Delta}_{l,s}/T^3$
9	149	16	32	0.00464	0.05293	6.72	6.00	3.07(12)	5.7(2)
10	149	16	48	0.00468	0.05295	6.85	5.65	5.00(10)	6.3(1)
10	149	16	64	0.00459	0.05289	-	-	5.57(10)	6.2(1)
22	149	32	32	0.00464	0.05293	6.45	6.39	3.84(5)	6.4(1)
23	159	32	32	0.00421	0.04856	3.86	4.28	2.83(6)	4.2(1)
25	168	32	32	0.00395	0.04490	1.64	2.19	1.46(7)	2.3(1)
26	177	32	32	0.00367	0.04165	-	1.21	0.71(5)	1.3(1)
27	186	32	32	0.00341	0.03873	-	0.42	0.22(4)	0.46(5)
28	195	32	32	0.00314	0.03619	-	0.25	0.14(3)	0.30(6)

Table 6.6: Comparison of the unrenormalized results for $\Delta_{l,s}$ computed using four different methods at various temperatures and values of L_s. The data in the $16^3 \times 8$, $L_s = 64$ row results from a valence calculation performed on the $L_s = 48$, $\beta = 1.671$ (run # 10) ensemble. (While these quantities are all expressed in the scheme defined by the bare lattice mass, m_q, this is not the scheme in which the eigenvalues of the 5-dimensional DWF Dirac operator are defined and renormalization using the factor $Z_{\rm tw\to m_f}$ defined in Table 6.4 has been carried out.)

Finally we examine the results at $T = 149$ MeV where multiple ensembles with different values of L_s are available, shown in the first four lines of Table 6.6. Here results are shown for three values of L_s: 32, 48 and 64. As expected, the simple difference $\Delta_{l,s}$ shows a very strong dependence on L_s. While there should be substantial cancellation between the large, continuum-like modes in this difference, at the very highest energies this cancellation will be distorted by residual chiral symmetry breaking effects. The use of the factor $(m_l+m_{\rm res})/(m_s+m_{\rm res})$ in the subtracted strange condensate will not, in general, cause these effects to cancel.

However, this argument suggests that as L_s increases and these residual chiral symmetry breaking effects are suppressed, $\Delta_{l,s}$ should approach $\widetilde{\Delta}_{l,s}$, behavior that can be seen in Table 6.6. Less consistent is the apparent increase in the value of $\widetilde{\Delta}_{l,s}/T^3$ with increasing L_s seen on the 16^3 volume, where an increase by more than two standard deviation from 5.7(2) to 6.2(1) is seen as L_s grows from 32 to 64. Since $\widetilde{\Delta}_{l,s}$ is supposed to already be close to its $L_s = \infty$ value such L_s dependence is not expected and we attribute this discrepancy to the under estimation of statistical errors for this small, 16^3 volume.

6.7 Near-Zero Modes and $U(1)_A$ Symmetry

We now turn to one of the central questions addressed in this report, the origin of the observed $U(1)_A$ symmetry breaking above T_c. We will focus on the quantity $\Delta_{\pi,\delta} = \chi_\pi - \chi_\delta$ since this difference of susceptibilities can be expressed in terms of the spectral density using Eq. (6.3). Table 6.7 shows this difference at six temperatures as determined from the integrated connected Green's functions. This difference contains only a very small logarithmic singularity after multiplicative renormalization by $1/Z^2_{m_f \to \overline{\text{MS}}}$ in the continuum, $\sim (m_l + m_{\text{res}})^2 \ln m_l a$, where the sum $m_l + m_{\text{res}}$ represents schematically the effects of both the input quark mass and DWF residual chiral symmetry breaking. This controlled high-energy behavior is realized by the convergence of the integral in Eq. (6.3), even when $\rho(\lambda)$ increases linearly or quadratically with λ.

Therefore, in Table 6.7 we also show the contributions to the spectral integral in Eq. (6.3) of each of the three separate ansätze in Eq. (6.4), given in Eq. (6.5). Some cells are left blank because the corresponding behavior cannot be seen in the spectral data. For example, at $T \leq 168$ MeV, there is no visible accumulation of near-zero modes that might be described by a $\delta(\lambda)$ term in $\rho(\lambda)$. However, at $T \geq 177$ MeV and above we can count a number of near-zero modes that form a small but visible peak in $\rho(\lambda)$ near $\lambda = 0$. Assuming a Poisson distribution, we take the square root of the total number of these near-zero modes as a rough

estimate of errors for the corresponding contribution. Similarly the constant contribution or intercept has vanished for $T \geq 177$ MeV and above $T = 177$ MeV the linear term is also difficult to determine and the eigenvalue density is dominated by what appears to be quadratic behavior.

We can also determine the susceptibility difference $\Delta_{\pi,\delta}$ by using a direct sum over modes as was done for $\Delta_{l,s}$ in Eq. (6.27) and tabulated as $\Delta^{\rm ms}_{l,s}$ in Table 6.6. Examining the continuum spectral Eq. (6.3), we can write an expression for $\Delta_{\pi,\delta}$ analogous to that in Eq. (6.27) for $\Delta_{l,s}$:

$$\Delta^{\rm ms}_{\pi,\delta} = \frac{1}{N_\sigma^3 N_\tau} \left\langle \sum_{n=1}^{100} \frac{2\widetilde{m}_l^2}{\Lambda_n^4} \right\rangle . \tag{6.29}$$

The results from this mode sum are shown in the second column from the right in Table 6.7 where very good agreement is seen with the explicit difference of correlation functions. This substitution of our renormalized DWF eigenvalue spectrum directly into the continuum equation for $\Delta_{\pi,\delta}$ is a stringent test of that spectrum. The infra-red singular factor $1/\Lambda_n^4$ appearing in Eq. (6.29) might have shown large, unphysical fluctuations associated with configuration-by-configuration fluctuations in residual chiral symmetry breaking. In fact, it is possible that the larger values shown in Table 6.7 for $\Delta^{\rm ms}_{\pi,\delta}$ relative to the actual correlator difference $\Delta_{\pi,\delta}$ at the two lowest temperatures are a result of this effect. However, overall the agreement between $\Delta^{\rm ms}_{\pi,\delta}$ and $\Delta_{\pi,\delta}$ is remarkably good.

The separate contributions to $\Delta_{\pi,\delta}$ presented in Table 6.7 give a clear, quantitative description of how the contribution of each piece evolves as the temperature increases. For $T \leq T_c$, the constant, or Banks-Casher term, gives the major contribution to $\Delta_{\pi,\delta}$. In contrast, in the region above the pseudo-critical temperature, the delta function term dominates and its contribution alone agrees well with the result from the difference of integrated correlators. We conclude that the non-zero $U(1)_A$ symmetry breaking that we observe above T_c in the correlator difference $\chi_\pi - \chi_\delta$ results from this small cluster of near-zero modes which can be seen in the spectral distributions shown in Fig. 6.3 for $T = 177$, 186 and 195 MeV and

more easily in the expanded plots in Fig. 6.4.

It is possible that these near-zero modes become exact zero modes in the continuum limit and are a result of non-zero global topology and the Atiyah-Singer theorem. If this is the case, the number of these zero modes should increase in proportion to $\sqrt{V}$ with increasing space-time volume. Thus, for zero modes resulting from non-zero global topology we expect the corresponding density per space-time volume to be proportional to $1/\sqrt{V}$. Were such exact zero modes the only contribution to $U(1)_A$ symmetry breaking then we would conclude that $U(1)_A$ symmetry will be restored in the limit of infinite volume.

However if we compare the results for 32^3 (solid red histograms) and 16^3 (black lines) in the expanded view of these peaks shown in Fig. 6.4 [1] for $T = 177$, 186 and 195 MeV, we easily see that the density is volume independent, instead of shrinking by a factor of $\sqrt{8}$ as the volume is increased from 16^3 to 32^3. Thus, the volume dependence of these near-zero modes corresponds to what is expected if they result from a relatively dilute gas of instantons and anti-instantons whose number, and whose corresponding near-zero modes, will grow proportional to the volume.

We have also examined the chirality of these near-zero modes. In particular, if these modes are the result of non-zero global topology, then, for a single configuration, all these modes should be of the same chirality, that of the global topological charge ν. If ν is positive then each of the zero modes should be right-handed and in our DWF case have support primarily on the right-hand, $s = L_s - 1$ boundary. If ν is negative then all modes should be left-handed and their wave functions should be largest on the left-hand, $s = 0$ boundary. In contrast, if these modes arise from a dilute instanton gas, they are produced by a mixture of instantons and anti-instantons and the chirality of each mode should have an equal probability to be either positive or negative within a single configuration.

We choose the $T = 177$ MeV ensemble to study the chirality of the near-zero modes since

[1] Here we use the distributions of Λ instead of λ near the origin, since it allows us to ignore the large relative fluctuations in these small eigenvalues below $\widetilde{m}_l$.

it has the most near-zero modes among the three highest temperature ensembles, where these modes are seen. We did not save the full five-dimensional eigenfunctions when computing the lowest 100 modes and have available only values for the squared modulus of the five-dimensional wave function, integrated over the left- and right- hand wall for each mode. Therefore we define the chirality of the n^{th} mode as

$$\chi_n = \frac{\int \mathrm{d}^4x \overline{\Psi}_n(x,0)(1+\gamma_5)\Psi_n(x,0) - \int \mathrm{d}^4x \overline{\Psi}_n(x,L_s-1)(1-\gamma_5)\Psi(x,L_s-1)}{\int \mathrm{d}^4x \overline{\Psi}_n(x,0)(1+\gamma_5)\Psi(x,0) + \int \mathrm{d}^4x \overline{\Psi}_n(x,L_s-1)(1-\gamma_5)\Psi(x,L_s-1)} \tag{6.30}$$

which compensates for the fact that even for a chirality eigenstate, the five-dimensional wave function will not be localized solely on one of the four-dimensional walls but will spread into the fifth dimension. If we examine the zero modes, we find that some of them have chiralilty near zero. This might be expected for a not-too-dilute instanton gas where the two modes of a nearby instanton-anti-instanton pair will mix so that neither have a definite chirality, However, such behavior could also be the result of our strong coupling and gauge configurations with changing topology producing zero modes of uncertain chirality. As a result we choose to examine only those near-zero modes whose chirality is greater than 0.7 in magnitude. The effects of this choice choice can be seen in Fig. 6.6 where we plot the histogram of the near-zero modes for T = 177, 186 and 195 MeV. It appears that at these temperatures, almost all of the near-zero modes are localized on one of the two four-dimensional walls and thus have a chirality very close to +1 or -1. Our restriction that the magnitude of the chirality is greater than 0.7 captures approximately 95% of the near-zero modes. Fig. 6.6 suggests that this concentration of chirality at ±1 increases with increasing temperature. Determining whether this apparent trend is the result of i) limited statistics at the higher temperatures, ii) increasing spatial localization of the zero modes and therefore less mixing as T increases or iii) better defined gauge field topology at weaker coupling requires further study.

Table 6.8 lists the number of configurations which have N_0 near-zero modes, N_+ of which have positive chirality. Those modes included in the counts presented in Table 6.8 must lie

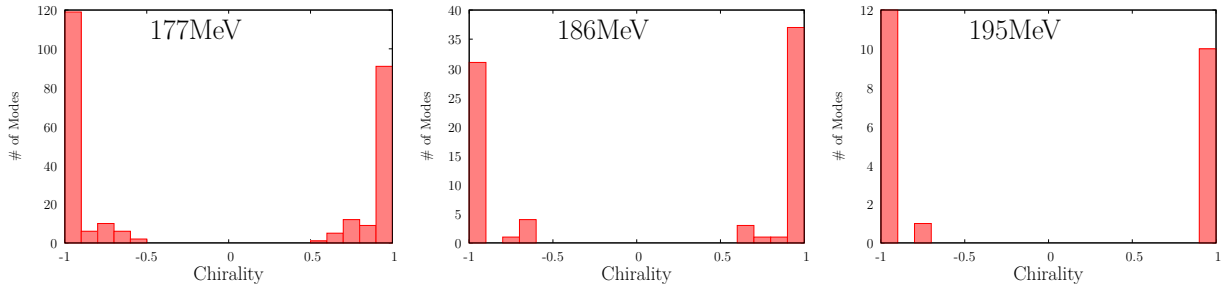

Figure 6.6: (Left to right) The distribution of chiralities for the near-zero modes at the three temperatures T = 177, 186 and 195 MeV and the $32^3 \times 8$ volume. Here we only use modes lying in the first four histogram bins in Fig. 6.4 which corresponds to $\Lambda \lesssim 12.5$ MeV.

in the peak region (first four bins) shown in Fig. 6.4, with Λ at or below approximately 12.5 MeV and with a chirality of magnitude 0.7 or greater. A binomial distribution consistent with the DIGA describes the data in a more convincing way than the bimodal distribution that would be seen for the exact zero modes resulting from non-zero global topology.

We conclude that the agreement between the value of $\Delta_{\pi,\delta}$ measured from the difference of correlators and the delta-function contribution $\Delta^0_{\pi,\delta}$ shown in Table 6.7 implies that the anomalous breaking of chiral symmetry for $T > T_c$ results from these near-zero modes. Further, the volume dependence and chirality distribution of the modes making up this delta-function contribution gives strong evidence that the non-zero anomalous symmetry breaking found above T_c is the result of a dilute gas of instantons and anti-instantons and that no new mechanism of anomalous symmetry breaking is needed.

#	T (MeV)	β	$\widetilde{m}_l$	$\Delta^0_{\pi,\delta}/T^2$	$\Delta^1_{\pi,\delta}/T^2$	$\Delta^2_{\pi,\delta}/T^2$	$\Delta^{\rm ms}_{\pi,\delta}/T^2$	$\Delta_{\pi,\delta}/T^2$
22	149	1.671	0.00464	-	3.7(3)	76(2)	109	87(2)
23	159	1.707	0.00421	-	4.6(1)	42(1)	70	60(2)
25	168	1.740	0.00395	-	4.9(1)	11(1)	35	35(2)
26	177	1.771	0.00367	23(1)	5.0(1)	-	25	23(2)
27	186	1.801	0.00341	8(1)	-	-	8	6(1)
28	195	1.829	0.00314	7(1)	-	-	6	6(2)

Table 6.7: A comparison of $\Delta_{\pi,\delta}$ measured from the difference of correlation functions with the three contributions computed from fitting the eigenvalue density to the expression in Eq. (6.4) and with the result $\Delta^{\rm ms}_{\pi,\delta}$ obtained from the mode sum given in Eq. (6.29), for the $32^3 \times 8$ ensembles. All results are renormalized in the $\overline{\rm MS}(\mu = 2$ GeV$)$ scheme.

$N_+ \backslash N_0$	0	1	2	3	4	5
$N_0 = 1$	40	29	-	-	-	-
$N_0 = 2$	11	20	12	-	-	-
$N_0 = 3$	3	11	6	2	-	-
$N_0 = 4$	0	1	2	1	0	-
$N_0 = 5$	0	2	0	0	0	0

Table 6.8: The number of configurations found in the 177 MeV (run # 26) ensemble with given values for the total number (N_0) of near-zero modes and total number (N_+) of those modes with positive chirality. We consider only modes with $\Lambda \leq 12.5$ MeV and a chirality whose magnitude exceeds 0.7. The distribution is clearly different from the bimodal distribution $N_+ = N_0$ or 0 expected if these near-zero modes were induced by non-zero global topology and the Atiyah-Singer theorem.

Chapter 7

Conclusion

We will now briefly summarize our results. This work is a natural extension of earlier studies on the finite temperature QCD using DWF with relatively heavy fixed bare quark masses [32, 33] now to a line of constant physics with physical or almost physical quark masses on a variety of lattices with $N_\tau = 8$.

For ensembles with $m_\pi \approx 200$ MeV, the disconnected chiral susceptibility $\chi_{\rm disc}$ shows a distinct peak as the temperature increases through the critical region on volume $24^3 \times 8$ and $32^3 \times 8$. This is the quantity of choice for locating the pseudo-critical temperature and showed a quite broad peak when studied on the $16^3 \times 8$ volume. The 24^3 and 32^3 results presented here show a significant volume dependence when compared with 16^3 results with the large shoulder just below $T_c \approx 164$ MeV decreasing by between 30 and 50% as the volume is increased and the peak itself moving to higher temperature and decreasing in height by approximately 15%. The 24^3 and 32^3 volumes give similar results. This behavior is predicted by finite size scaling in $O(4)$ models in the presence of an external symmetry breaking field [139] and could be anticipated from the first comparison made with QCD data [123] and the recent work of Braun *et al.* [122].

For ensembles with physical pions ($m_\pi \approx 135$ MeV), the peak of $\chi_{\rm disc}$ is even more dramatic and shifted slightly to a lower temperature as compared with $\chi_{\rm disc}$ curve from $m_\pi \approx 200$ MeV.

Results from both $32^3 \times 8$ and $64^3 \times 8$ show great consistency within errors, implying the absence of volume effects. And no evidence is present for a metastable behavior in the evolution of the chiral condensate near T_c. Both observations are strong evidence that we are seeing the cross-over behavior expected when the actual QCD phase transition is a second-order critical point at $\widetilde{m}_l = 0$. Although a complete finite volume $O(4)$ scaling analysis is not available at the moment, a qualitative examination as well as some empirical fits suggest a pseudo-critical temperature for the $2+1$ flavors of physical quarks to be $T_c = 154(1)(8)$ MeV. The first, statistical error from the fitting is overwhelmed by the second, discretization error.

We investigate $U(1)_A$ symmetry breaking above T_c by examining the two $U(1)_A$ symmetry breaking differences $\chi_\pi - \chi_\delta$ and $\chi_\sigma - \chi_\eta$. These vanish if $U(1)_A$ symmetry is realized and are clearly non-zero at $T = 177$ MeV, although they decrease quickly as T is increased above this value. These two quantities are related by $SU(2)_L \times SU(2)_R$ symmetry and are equal within errors for $T \geq 177$ MeV. We conclude that for temperatures at which $SU(2)_L \times SU(2)_R$ symmetry has been restored, $U(1)_A$ symmetry breaking is still present.

The Dirac eigenvalue spectra per unit space-time volume seen on the $16^3 \times 8$ and $32^3 \times 8$ volumes with $m_\pi \approx 200$ MeV are very similar. However, the larger volume results are more accurate in the region of small eigenvalues. We find that appropriately convergent combinations of spectral integrals agree well with the observed Green's functions to which they are related in continuum field theory. Of particular importance is the agreement between a spectral integral and $\chi_\pi - \chi_\delta$. For $T = 177$ MeV we find a small cluster of near-zero Dirac eigenvalues, such as are expected from the dilute instanton gas approximation (DIGA) [104] and it is these eigenvalues which, when included in the spectral formula, reproduce the measured result for $\chi_\pi - \chi_\delta$. This relation continues to hold, although within larger errors, at $T = 186$ and 195 MeV. The number of these near-zero modes is found to be proportional to the volume and their chiralities show a mixture of positive and negative values per configuration, as is expected in the DIGA. We conclude that $U(1)_A$ symmetry is broken in the region

immediately above T_c and this breaking is explained by the DIGA. No additional mechanism is necessary.

For the completeness of this exploration, we still need to check our control of the finite lattice spacing errors. To this end, we are now carrying out simulations on a lattice of $64^3 \times 12$ with $\beta = 1.943$ and physical quarks, aiming at $T \approx 154$ MeV, which is in the vicinity of the phase transition (conditions similar to run $\#\,31$). We may also extend our Dirac eigenvalue spectrum calculation to the Möbius domain wall fermions. The definition of a Hermitian Dirac operator involves much more subtleties than the ordinary DWF Dirac operator. The most promising candidate is $\gamma_5 R_5 (D_-)^{-1} D$ (*c.f.* Chap. 2 and [57]), a non-local operator. However, the physical picture of spontaneous vacuum chiral symmetry breaking and anomalous symmetry breaking arising from a gas of dilute instantons is already clean for $m_\pi \approx 200$ MeV with no indications that different phenomena will appear at smaller quark mass. Thus, it appears likely that th present study reveals quite completely the crossover nature of the QCD phase transition at physical quark mass and the present of anomalous symmetry breaking above T_c, well described by the DIGA.

Bibliography

[1] T. Blum, P.A. Boyle, N.H. Christ, N. Garron, E. Goode, et al. The $K \to (\pi\pi)_{I=2}$ Decay Amplitude from Lattice QCD. *Phys.Rev.Lett.*, 108:141601, 2012.

[2] Christopher Kelly. Continuum Results for Light Hadronic Quantities using Domain Wall Fermions with the Iwasaki and DSDR Gauge Actions. *PoS*, LATTICE2011:285, 2011.

[3] Michael Cheng. *The QCD Equation of State with charm quarks from Lattice QCD*. PhD thesis, Columbia University, 2008.

[4] Frithjof Karsch. Thermodynamics of strong interaction matter from lattice QCD and the hadron resonance gas model. 2013.

[5] A. Bazavov, T. Bhattacharya, M. Cheng, C. DeTar, H.T. Ding, et al. The chiral and deconfinement aspects of the QCD transition. *Phys.Rev.*, D85:054503, 2012.

[6] J. Beringer et al. Review of Particle Physics (RPP). *Phys.Rev.*, D86:010001, 2012.

[7] G. Arnison et al. Experimental Observation of Isolated Large Transverse Energy Electrons with Associated Missing Energy at s**(1/2) = 540-GeV. *Phys.Lett.*, B122:103–116, 1983.

[8] M. Banner et al. Observation of Single Isolated Electrons of High Transverse Momentum in Events with Missing Transverse Energy at the CERN anti-p p Collider. *Phys.Lett.*, B122:476–485, 1983.

[9] F. Abe et al. Observation of top quark production in $\bar{p}p$ collisions. *Phys.Rev.Lett.*, 74:2626–2631, 1995.

[10] S. Abachi et al. Search for high mass top quark production in $p\bar{p}$ collisions at $\sqrt{s}$ = 1.8 TeV. *Phys.Rev.Lett.*, 74:2422–2426, 1995.

[11] Georges Aad et al. Observation of a new particle in the search for the Standard Model Higgs boson with the ATLAS detector at the LHC. *Phys.Lett.*, B716:1–29, 2012.

[12] Serguei Chatrchyan et al. Observation of a new boson at a mass of 125 GeV with the CMS experiment at the LHC. *Phys.Lett.*, B716:30–61, 2012.

[13] A. Pais. Some Remarks on the V-Particles. *Phys.Rev.*, 86:663–672, 1952.

[14] S. L. Glashow. Partial Symmetries of Weak Interactions. *Nucl. Phys.*, 22:579–588, 1961.

[15] Abdus Salam and John Clive Ward. Electromagnetic and weak interactions. *Phys. Lett.*, 13:168–171, 1964.

[16] Steven Weinberg. A Model of Leptons. *Phys. Rev. Lett.*, 19:1264–1266, 1967.

[17] Murray Gell-Mann. The eightfold way: A theory of strong interaction symmetry. CTSL-20.

[18] Yuval Ne'eman. Derivation of strong interactions from a gauge invariance. *Nucl. Phys.*, 26:222–229, 1961.

[19] Murray Gell-Mann. A schematic model of baryons and mesons. *Phys. Lett.*, 8:214–215, 1964.

[20] G. Zweig. An su(3) model for strong interaction symmetry and its breaking. 2. CERN-TH-412.

[21] V. E. Barnes et al. Confirmation of the existence of the ω^- hyperon. *Phys. Lett.*, 12:134–136, 1964.

[22] H. David Politzer. RELIABLE PERTURBATIVE RESULTS FOR STRONG INTERACTIONS? *Phys. Rev. Lett.*, 30:1346–1349, 1973.

[23] D. J. Gross and Frank Wilczek. ULTRAVIOLET BEHAVIOR OF NON-ABELIAN GAUGE THEORIES. *Phys. Rev. Lett.*, 30:1343–1346, 1973.

[24] J.D. Bjorken. Asymptotic Sum Rules at Infinite Momentum. *Phys.Rev.*, 179:1547–1553, 1969.

[25] Robert D. Pisarski and Frank Wilczek. Remarks on the Chiral Phase Transition in Chromodynamics. *Phys.Rev.*, D29:338–341, 1984.

[26] Kenneth G. Wilson. Confinement of Quarks. *Phys.Rev.*, D10:2445–2459, 1974.

[27] Michael Creutz. Confinement and the Critical Dimensionality of Space-Time. *Phys.Rev.Lett.*, 43:553–556, 1979.

[28] M. Creutz. Monte Carlo Study of Quantized SU(2) Gauge Theory. *Phys. Rev.*, D21:2308–2315, 1980.

[29] John B. Kogut and Leonard Susskind. Hamiltonian Formulation of Wilson's Lattice Gauge Theories. *Phys. Rev.*, D11:395, 1975.

[30] Leonard Susskind. Lattice Fermions. *Phys. Rev.*, D16:3031–3039, 1977.

[31] Szabolcs Borsanyi et al. Is there still any Tc mystery in lattice QCD? Results with physical masses in the continuum limit III. *JHEP*, 1009:073, 2010.

[32] P. Chen et al. The finite temperature qcd phase transition with domain wall fermions. *Phys. Rev.*, D64:014503, 2001.

[33] Michael Cheng, Norman H. Christ, Min Li, Robert D. Mawhinney, Dwight Renfrew, et al. The finite temperature QCD using 2 + 1 flavors of domain wall fermions at N (t) = 8. *Phys.Rev.*, D81:054510, 2010.

[34] S. Borsanyi, Y. Delgado, S. Durr, Z. Fodor, S.D. Katz, et al. QCD thermodynamics with dynamical overlap fermions. 2012.

[35] A. Bazavov et al. The chiral transition and $U(1)_A$ symmetry restoration from lattice QCD using Domain Wall Fermions. *Phys.Rev.*, D86:094503, 2012.

[36] Guido Cossu, Sinya Aoki, Hidenori Fukaya, Shoji Hashimoto, Takashi Kaneko, et al. Finite temperature study of the axial U(1) symmetry on the lattice with overlap fermion formulation. 2013.

[37] David B. Kaplan. A Method for simulating chiral fermions on the lattice. *Phys.Lett.*, B288:342–347, 1992.

[38] Vadim Furman and Yigal Shamir. Axial symmetries in lattice QCD with Kaplan fermions. *Nucl.Phys.*, B439:54–78, 1995.

[39] Richard C. Brower, Hartmut Neff, and Kostas Orginos. Mobius fermions: Improved domain wall chiral fermions. *Nucl.Phys.Proc.Suppl.*, 140:686–688, 2005.

[40] R.C. Brower, H. Neff, and K. Orginos. Mobius fermions. *Nucl.Phys.Proc.Suppl.*, 153:191–198, 2006.

[41] Pavlos M. Vranas. Domain wall fermions in vector theories. pages 11–26, 1999.

[42] Pavlos M. Vranas. Gap Domain Wall Fermions. *Phys.Rev.*, D74:034512, 2006.

[43] Hidenori Fukaya et al. Lattice gauge action suppressing near-zero modes of H(W). *Phys.Rev.*, D74:094505, 2006.

[44] Dwight Renfrew, Thomas Blum, Norman Christ, Robert Mawhinney, and Pavlos Vranas. Controlling Residual Chiral Symmetry Breaking in Domain Wall Fermion Simulations. *PoS*, LATTICE2008:048, 2008.

[45] Michael I. Buchoff, Michael Cheng, Norman H. Christ, H. T. Ding, Chulwoo Jung, et al. The QCD chiral transition, $U(1)_A$ symmetry and the Dirac spectrum using domain wall fermions. 2013.

[46] Michael I. Buchoff, Michael Cheng, Norman H. Christ, H. T. Ding, Chulwoo Jung, et al. The QCD phase transition with physical-mass, chiral quarks. in preparation.

[47] H. Rothe. Lattice Gauge Theories - An Introduction. 2005.

[48] Frithjof Karsch. Lattice QCD at high temperature and density. *Lect.Notes Phys.*, 583:209–249, 2002.

[49] F. Karsch and E. Laermann. Thermodynamics and in medium hadron properties from lattice QCD. 2003.

[50] Y. Iwasaki. Renormalization Group Analysis of Lattice Theories and Improved Lattice Action: Two-Dimensional Nonlinear O(N) Sigma Model. *Nucl.Phys.*, B258:141–156, 1985.

[51] Tetsuya Takaishi. Heavy quark potential and effective actions on blocked configurations. *Phys.Rev.*, D54:1050–1053, 1996.

[52] David J. Antonio et al. Localization and chiral symmetry in three flavor domain wall QCD. *Phys.Rev.*, D77:014509, 2008.

[53] Holger Bech Nielsen and M. Ninomiya. Absence of Neutrinos on a Lattice. 1. Proof by Homotopy Theory. *Nucl.Phys.*, B185:20, 1981.

[54] Kenneth G. Wilson. Quarks and Strings on a Lattice. 1975.

[55] Pavlos M. Vranas. Chiral symmetry restoration in the Schwinger model with domain wall fermions. *Phys.Rev.*, D57:1415–1432, 1998.

[56] Ting-Wai Chiu. Optimal domain wall fermions. *Phys.Rev.Lett.*, 90:071601, 2003.

[57] Hantao Yin. *Precision Lattice Calculation of Kaon Decays with Mobius Domain Wall Fermions*. PhD thesis, Columbia University, 2013.

[58] Paul H. Ginsparg and Kenneth G. Wilson. A Remnant of Chiral Symmetry on the Lattice. *Phys.Rev.*, D25:2649, 1982.

[59] Herbert Neuberger. Exactly massless quarks on the lattice. *Phys.Lett.*, B417:141–144, 1998.

[60] Herbert Neuberger. More about exactly massless quarks on the lattice. *Phys.Lett.*, B427:353–355, 1998.

[61] Maarten Golterman and Yigal Shamir. Localization in lattice QCD. *Phys.Rev.*, D68:074501, 2003.

[62] Maarten Golterman, Yigal Shamir, and Benjamin Svetitsky. Mobility edge in lattice QCD. *Phys.Rev.*, D71:071502, 2005.

[63] Maarten Golterman, Yigal Shamir, and Benjamin Svetitsky. Localization properties of lattice fermions with plaquette and improved gauge actions. *Phys.Rev.*, D72:034501, 2005.

[64] Edward V. Shuryak. Quantum Chromodynamics and the Theory of Superdense Matter. *Phys.Rept.*, 61:71–158, 1980.

[65] N. Itoh. Hydrostatic Equilibrium of Hypothetical Quark Stars. *Prog.Theor.Phys.*, 44:291, 1970.

[66] Johann Rafelski and Berndt Muller. Strangeness Production in the Quark - Gluon Plasma. *Phys.Rev.Lett.*, 48:1066, 1982.

[67] C. Blume and C. Markert. Strange hadron production in heavy ion collisions from SPS to RHIC. *Prog.Part.Nucl.Phys.*, 66:834–879, 2011.

[68] G. Agakishiev et al. Strangeness Enhancement in Cu+Cu and Au+Au Collisions at $\sqrt{s_{NN}}$ = 200 GeV. *Phys.Rev.Lett.*, 108:072301, 2012.

[69] B.I. Abelev et al. Charged and strange hadron elliptic flow in Cu+Cu collisions at $\sqrt{s_{NN}}$ = 62.4 and 200 GeV. *Phys.Rev.*, C81:044902, 2010.

[70] Maria Nicassio. Multi-strange baryon production in Pb-Pb collisions at s(NN)**(1/2) = 2.76-TeV with the ALICE experiment at the LHC. *Acta Phys.Polon.Supp.*, 5:237–242, 2012.

[71] T. Matsui and H. Satz. J/ψ Suppression by Quark-Gluon Plasma Formation. *Phys.Lett.*, B178:416, 1986.

[72] N.S. Topilskaya et al. Transverse momentum distribution of J/psi produced in Pb Pb and p A interactions at the CERN SPS. *Nucl.Phys.*, A715:675–678, 2003.

[73] B. Alessandro et al. A New measurement of J/psi suppression in Pb-Pb collisions at 158-GeV per nucleon. *Eur.Phys.J.*, C39:335–345, 2005.

[74] Robert L. Thews, Martin Schroedter, and Johann Rafelski. Enhanced J/ψ production in deconfined quark matter. *Phys.Rev.*, C63:054905, 2001.

[75] J.D. Bjorken. Energy Loss of Energetic Partons in Quark - Gluon Plasma: Possible Extinction of High p(t) Jets in Hadron - Hadron Collisions. 1982.

[76] K. Adcox et al. Suppression of hadrons with large transverse momentum in central Au+Au collisions at $\sqrt{s_{NN}}$ = 130-GeV. *Phys.Rev.Lett.*, 88:022301, 2002.

[77] C. Adler et al. Disappearance of back-to-back high p_T hadron correlations in central Au+Au collisions at $\sqrt{s_{NN}}$ = 200-GeV. *Phys.Rev.Lett.*, 90:082302, 2003.

[78] Georges Aad et al. Observation of a Centrality-Dependent Dijet Asymmetry in Lead-Lead Collisions at $\sqrt{s_{NN}}$ = 2.77 TeV with the ATLAS Detector at the LHC. *Phys.Rev.Lett.*, 105:252303, 2010.

[79] Deepali Sharma. phi- meson Production at RHIC energies using the PHENIX Detector. *J.Phys.*, G36:064023, 2009.

[80] Barbara V. Jacak and Berndt Muller. The exploration of hot nuclear matter. *Science*, 337:310–314, 2012.

[81] Barbara Jacak and Peter Steinberg. Creating the perfect liquid in heavy-ion collisions. *Phys.Today*, 63N5:39–43, 2010.

[82] Berndt Muller, Jurgen Schukraft, and Boleslaw Wyslouch. First Results from Pb+Pb collisions at the LHC. *Ann.Rev.Nucl.Part.Sci.*, 62:361–386, 2012.

[83] Axel Maas. Describing gauge bosons at zero and finite temperature. *Phys.Rept.*, 524:203–300, 2013.

[84] Lorenz von Smekal. Universal Aspects of QCD-like Theories. *Nucl.Phys.Proc.Suppl.*, 228:179–220, 2012.

[85] Tina K. Herbst, Jan M. Pawlowski, and Bernd-Jochen Schaefer. On the phase structure and thermodynamics of QCD. *Phys.Rev.*, D88:014007, 2013.

[86] Enrico Meggiolaro and Alessandro Morda. Remarks on the U(1) axial symmetry and the chiral transition in QCD at finite temperature. *Phys. Rev. D*, 88:096010, 2013.

[87] G. Boyd, J. Engels, F. Karsch, E. Laermann, C. Legeland, et al. Thermodynamics of SU(3) lattice gauge theory. *Nucl.Phys.*, B469:419–444, 1996.

[88] Y. Iwasaki, K. Kanaya, T. Kaneko, and T. Yoshie. Scaling in SU(3) pure gauge theory with a renormalization group improved action. *Phys.Rev.*, D56:151–160, 1997.

[89] Benjamin Svetitsky and Laurence G. Yaffe. Critical Behavior at Finite Temperature Confinement Transitions. *Nucl.Phys.*, B210:423, 1982.

[90] A. Bazavov et al. Update on the 2+1+1 flavor QCD equation of state with HISQ. *PoS*, LATTICE2013:154, 2013.

[91] Szabolcs Borsanyi, Zoltan Fodor, Christian Hoelbling, Sandor D. Katz, Stefan Krieg, et al. Continuum EoS for QCD with Nf=2+1 flavors. *PoS*, LATTICE2013:155, 2013.

[92] Z. Fodor and S.D. Katz. Critical point of QCD at finite T and mu, lattice results for physical quark masses. *JHEP*, 0404:050, 2004.

[93] Shinji Ejiri, Chris R. Allton, Simon J. Hands, Olaf Kaczmarek, Frithjof Karsch, et al. Study of QCD thermodynamics at finite density by Taylor expansion. *Prog.Theor.Phys.Suppl.*, 153:118–126, 2004.

[94] Massimo D'Elia and Maria-Paola Lombardo. Finite density QCD via imaginary chemical potential. *Phys.Rev.*, D67:014505, 2003.

[95] Anyi Li, Andrei Alexandru, and Keh-Fei Liu. Critical point of $N_f = 3$ QCD from lattice simulations in the canonical ensemble. *Phys.Rev.*, D84:071503, 2011.

[96] Keitaro Nagata and Atsushi Nakamura. Wilson Fermion Determinant in Lattice QCD. *Phys.Rev.*, D82:094027, 2010.

[97] H. Saito et al. Phase structure of finite temperature QCD in the heavy quark region. *Phys.Rev.*, D84:054502, 2011.

[98] Gert Aarts, Erhard Seiler, and Ion-Olimpiu Stamatescu. The Complex Langevin method: When can it be trusted? *Phys.Rev.*, D81:054508, 2010.

[99] Terukazu Ichihara, Akira Ohnishi, and Takashi Z. Nakano. Auxiliary field Monte-Carlo simulation of strong coupling lattice QCD for QCD phase diagram. 2014.

[100] Stephen L. Adler. Axial vector vertex in spinor electrodynamics. *Phys.Rev.*, 177:2426–2438, 1969.

[101] J.S. Bell and R. Jackiw. A PCAC puzzle: pi0 → gamma gamma in the sigma model. *Nuovo Cim.*, A60:47–61, 1969.

[102] Gerard 't Hooft. Symmetry Breaking Through Bell-Jackiw Anomalies. *Phys.Rev.Lett.*, 37:8–11, 1976.

[103] Jr. Callan, Curtis G., R.F. Dashen, and David J. Gross. The Structure of the Gauge Theory Vacuum. *Phys.Lett.*, B63:334–340, 1976.

[104] David J. Gross, Robert D. Pisarski, and Laurence G. Yaffe. QCD and Instantons at Finite Temperature. *Rev.Mod.Phys.*, 53:43, 1981.

[105] Agostino Butti, Andrea Pelissetto, and Ettore Vicari. On the nature of the finite temperature transition in QCD. *JHEP*, 0308:029, 2003.

[106] Andrea Pelissetto and Ettore Vicari. Relevance of the axial anomaly at the finite-temperature chiral transition in QCD. *Phys.Rev.*, D88:105018, 2013.

[107] R. Rapp and J. Wambach. Chiral symmetry restoration and dileptons in relativistic heavy ion collisions. *Adv.Nucl.Phys.*, 25:1, 2000.

[108] Edward V. Shuryak. Which chiral symmetry is restored in hot QCD? *Comments Nucl.Part.Phys.*, 21:235–248, 1994.

[109] Zheng Huang and Xin-Nian Wang. Partial U(1)A restoration and eta enhancement in high-energy heavy ion collisions. *Phys.Rev.*, D53:5034–5041, 1996.

[110] Joseph I. Kapusta, D. Kharzeev, and Larry D. McLerran. The Return of the prodigal Goldstone boson. *Phys.Rev.*, D53:5028–5033, 1996.

[111] T. Csorgo, R. Vertesi, and J. Sziklai. Indirect observation of an in-medium η ' mass reduction in $\sqrt{s_{NN}}$ = 200 GeV Au+Au collisions. *Phys.Rev.Lett.*, 105:182301, 2010.

[112] Y. Aoki et al. Continuum Limit Physics from 2+1 Flavor Domain Wall QCD. *Phys.Rev.*, D83:074508, 2011.

[113] Murray Gell-Mann, R.J. Oakes, and B. Renner. Behavior of current divergences under SU(3) x SU(3). *Phys.Rev.*, 175:2195–2199, 1968.

[114] D.J. Antonio et al. First results from 2+1 Flavor Domain Wall QCD: Mass Spectrum, Topology Change and Chiral Symmetry with L(s) = 8. *Phys.Rev.*, D75:114501, 2007.

[115] Sinya Aoki, Taku Izubuchi, Yoshinobu Kuramashi, and Yusuke Taniguchi. Domain wall fermions in quenched lattice QCD. *Phys.Rev.*, D62:094502, 2000.

[116] T. Blum, P. Chen, Norman H. Christ, C. Cristian, C. Dawson, et al. Quenched lattice QCD with domain wall fermions and the chiral limit. *Phys.Rev.*, D69:074502, 2004.

[117] Meifeng Lin. *Hadron Physics with 2+1 Flavors of Domain Wall Fermions on the Lattice*. PhD thesis, Columbia University, 2007.

[118] M. Cheng, N.H. Christ, S. Datta, J. van der Heide, C. Jung, et al. The QCD equation of state with almost physical quark masses. *Phys.Rev.*, D77:014511, 2008.

[119] Lowell S. Brown, Robert D. Carlitz, and Choon-kyu Lee. Massless Excitations in Instanton Fields. *Phys.Rev.*, D16:417–422, 1977.

[120] N.H. Christ and L.L. Wu. The QCD phase transition with domain wall fermions. *Nucl.Phys.Proc.Suppl.*, 106:438–440, 2002.

[121] J. Braun, B. Klein, and H.-J. Pirner. Volume dependence of the pion mass in the quark-meson-model. *Phys.Rev.*, D71:014032, 2005.

[122] Jens Braun, Bertram Klein, and Piotr Piasecki. On the scaling behavior of the chiral phase transition in QCD in finite and infinite volume. *Eur.Phys.J.*, C71:1576, 2011.

[123] J. Engels, S. Holtmann, T. Mendes, and T. Schulze. Finite size scaling functions for 3-d O(4) and O(2) spin models and QCD. *Phys.Lett.*, B514:299–308, 2001.

[124] S. Ejiri, F. Karsch, E. Laermann, C. Miao, S. Mukherjee, et al. On the magnetic equation of state in (2+1)-flavor QCD. *Phys.Rev.*, D80:094505, 2009.

[125] J. Engels and F. Karsch. The scaling functions of the free energy density and its derivatives for the 3d O(4) model. *Phys.Rev.*, D85:094506, 2012.

[126] A. Ali Khan et al. Light hadron spectroscopy with two flavors of dynamical quarks on the lattice. *Phys.Rev.*, D65:054505, 2002.

[127] Tom Banks and A. Casher. Chiral Symmetry Breaking in Confining Theories. *Nucl.Phys.*, B169:103, 1980.

[128] Leonardo Giusti and Martin Luscher. Chiral symmetry breaking and the Banks-Casher relation in lattice QCD with Wilson quarks. *JHEP*, 0903:013, 2009.

[129] Shailesh Chandrasekharan and Norman H. Christ. Dirac spectrum, axial anomaly and the QCD chiral phase transition. *Nucl.Phys.Proc.Suppl.*, 47:527–534, 1996.

[130] G. Martinelli, C. Pittori, Christopher T. Sachrajda, M. Testa, and A. Vladikas. A General method for nonperturbative renormalization of lattice operators. *Nucl.Phys.*, B445:81–108, 1995.

[131] Y. Aoki et al. Non-perturbative renormalization of quark bilinear operators and B_K using domain wall fermions. *Phys. Rev.*, D78:054510, 2008.

[132] M. Gockeler, R. Horsley, H. Oelrich, H. Perlt, D. Petters, et al. Nonperturbative renormalization of composite operators in lattice QCD. *Nucl.Phys.*, B544:699–733, 1999.

[133] Thomas Kalkreuter and Hubert Simma. An Accelerated conjugate gradient algorithm to compute low lying eigenvalues: A Study for the Dirac operator in SU(2) lattice QCD. *Comput.Phys.Commun.*, 93:33–47, 1996.

[134] D. C. Sorensen. Implicit application of polynomial filters in a k-step arnoldi method. *SIAM J. Matrix Anal. Appl.*, 13(1):357–385, January 1992.

[135] D. Calvetti, L. Reichel, and D. C. Sorensen. An implicitly restarted lanczos method for large symmetric eigenvalue problems. *ETNA*, 2:1–21, 1994.

[136] Rudy Arthur. *Non-Perturbative Renormalization and Low Mode Averaging with Domain Wall Fermions*. PhD thesis, University of Edinburgh, 2012.

[137] Peter A. Boyle. The BAGEL assembler generation library. *Comput.Phys.Commun.*, 180:2739–2748, 2009.

[138] W. E. Arnoldi. The principle of minimized iterations in the solution of the matrix eigenvalue problem. *Q. Appl. Math*, 9(17):17–29, 1951.

[139] Juergen Engels and Frithjof Karsch. 2013. In preparation.

Appendix A

List of Lattice Ensembles

In the appendix, we list the details of the ensembles where multiples streams of evolutions are involved.

Tables A.1, A.2 and A.3 give the details of parameters for the $32^3 \times 8$ ensembles evolved using MDWF with $m_\pi \approx 135$ MeV. Among them, the first two tables A.1 and A.2 show the streams at 139 MeV $\leq T \leq$ 159 MeV and 164 MeV $\leq T \leq$ 195 MeV respectively. The last table A.3 shows the streams before the input quark masses were adjusted to be better aligned with the expected physical values.

The first column of the tables assigns a label to each individual evolution. The second to the fifth columns show the temperature, β, fifth dimension extent L_s and the Möbius coefficient c. The next three columns show the input light and strange quark masses as well as m_{res} which is measured from each individual stream.

The "Start" column indicates how this stream was begun, categorized as "ord" (a fresh start with an ordered gauge configuration), "dis" (a fresh start with a random gauge configuration), or a label of a stream with a trajectory number that specifies the trajectory where this stream began. The $N_{\text{traj}}^{\text{tot}}$ column gives the last trajectory number of the stream. Note that when a stream is split from another, the trajectory number will be carried on rather than reset to 0.

The "Cut" column indicates where the thermalization or the decorrelation cuts are imposed. We usually take the thermalization cut at trajectory 300 measured in units of molecular dynamic time separation. However, we, in some cases, accidentally enforced a maximum conjugate gradient step at 10000, which is too low for almost all these ensembles with physical pions. This results in an inaccuracy in Metropolis "Accept/Reject" step in the Hybrid Monte Carlo simulation causing errors at $\mathcal{O}(\delta\tau^2)$ level. We would allow 100 or more trajectories for thermalization for such instances. Moreover, as mentioned earlier, in many cases, there is also a small adjustment in the input quark masses. Again we allow 100 or more time units for the re-thermalization.

The last column, $N_{\text{traj}}^{\text{equil}} = N_{\text{traj}}^{\text{tot}} - \text{Cut}$ gives the number of equilibrated trajectories used from each stream. The sum of total numbers of $N_{\text{traj}}^{\text{equil}}$ at each temperature was already presented in Table 4.8.

Table A.4 gives the similar information for the $64^3 \times 8$ ensembles.

#	T (MeV)	β	L_s	c	m_l	m_s	$m_{\rm res}$	Start	$N_{\rm traj}^{\rm tot}$	Cut	$N_{\rm traj}^{\rm equil}$
43	139	1.633	24	1.5	0.00022	0.05960	0.00221(3)	ord	2172	400	1773
44	139	1.633	24	1.5	0.00022	0.05960	0.00218(2)	43: 468	2081	550	1531
45	139	1.633	24	1.5	0.00022	0.05960	0.00214(2)	dis	1848	300	1548
46	139	1.633	24	1.5	0.00022	0.05960	0.00224(2)	45: 788	1648	900	749
47	149	1.671	16	1.5	0.00034	0.05538	0.00174(2)	70: 692	3393	800	2593
48	149	1.671	16	1.5	0.00034	0.05538	0.00176(1)	47: 724	3142	800	2342
49	149	1.671	16	1.5	0.00034	0.05538	0.00176(2)	dis	2267	300	1967
50	149	1.671	16	1.5	0.00034	0.05538	0.00176(2)	49:1657	2267	1750	517
51	154	1.689	16	1.5	0.00075	0.05376	0.00119(2)	dis	1787	300	1487
52	154	1.689	16	1.5	0.00075	0.05376	0.00120(2)	dis	1746	300	1446
53	154	1.689	16	1.5	0.00075	0.05376	0.00118(2)	ord	1842	300	1542
54	154	1.689	16	1.5	0.00075	0.05376	0.00121(2)	ord	1768	300	1468
55	159	1.707	16	1.5	0.00112	0.05230	0.00092(1)	71: 494	4036	700	3336
56	159	1.707	16	1.5	0.00112	0.05230	0.00089(1)	55:1000	3784	1100	2684
57	159	1.707	16	1.5	0.00112	0.05230	0.00089(2)	dis	2809	300	2509

Table A.1: Summary of input parameters and trajectory information for each ensemble with $m_\pi \approx 135$ MeV at $32^3 \times 8$ for 139 MeV $\leq T \leq$ 159 MeV. Details of each column are explained in the main text of this appendix.

#	T (MeV)	β	L_s	c	m_l	m_s	$m_{\rm res}$	Start	$N_{\rm traj}^{\rm tot}$	Cut	$N_{\rm traj}^{\rm equil}$
58	164	1.725	16	1.5	0.00120	0.05045	0.00066(1)	dis	2204	300	1904
59	164	1.725	16	1.5	0.00120	0.05045	0.00066(2)	dis	2060	300	1760
60	164	1.725	16	1.5	0.00120	0.05045	0.00066(2)	ord	2126	300	1826
61	164	1.725	16	1.5	0.00120	0.05045	0.00066(2)	ord	1959	300	1659
62	168	1.740	16	1.2	0.00126	0.04907	0.00058(1)	72: 604	4338	700	3638
63	168	1.740	16	1.2	0.00126	0.04907	0.00055(2)	dis	2502	300	2202
64	177	1.771	16	1.0	0.00132	0.04614	0.00044(2)	73: 708	5991	800	5191
65	177	1.771	16	1.0	0.00132	0.04614	0.00039(2)	dis	3712	300	3412
66	186	1.801	16	1.0	0.00133	0.04345	0.00024(1)	74: 781	7374	900	6474
67	186	1.801	16	1.0	0.00133	0.04345	0.00025(2)	dis	3968	300	3668
68	195	1.829	16	0.9	0.00131	0.04122	0.00018(1)	75: 780	7335	900	6435
69	195	1.829	16	0.9	0.00131	0.04122	0.00018(1)	dis	4005	300	3705

Table A.2: Summary of input parameters and trajectory information for each ensemble with $m_\pi \approx 135$ MeV at $32^3 \times 8$ for 164 MeV $\leq T \leq$ 195 MeV. Details of each column are explained in the main text of this appendix.

#	T (MeV)	β	L_s	c	m_l	m_s	$m_{\rm res}$	Start	$N_{\rm traj}^{\rm tot}$	Cut	$N_{\rm traj}^{\rm equil}$
70	149	1.671	16	1.5	0.00016	0.05520	0.00171(3)	ord	692	-	-
71	159	1.707	16	1.5	0.00092	0.05210	0.00085(2)	ord	494	-	-
72	168	1.740	16	1.2	0.00119	0.04900	0.00057(3)	ord	604	-	-
73	177	1.771	16	1.0	0.00158	0.04640	0.00038(2)	ord	708	-	-
74	186	1.801	16	1.0	0.00148	0.04360	0.00026(2)	ord	781	-	-
75	195	1.829	16	0.9	0.00139	0.04130	0.00018(2)	ord	780	-	-

Table A.3: Summary of input parameters and trajectory information for the intial trial ensembles with $m_\pi \approx 135$ MeV at $32^3 \times 8$. The input masses of these runs were later adjusted. Details of each column are explained in the main text of this appendix.

#	T (MeV)	β	L_s	c	m_l	m_s	$m_{\rm res}$	Start	$N_{\rm traj}^{\rm tot}$	Cut	$N_{\rm traj}^{\rm equil}$
76	139	1.633	24	1.5	0.00022	0.05960	-	657	ord	300	357
77	149	1.671	16	1.5	0.00034	0.05538	-	1504	ord	300	1204
78	149	1.671	16	1.5	0.00034	0.05538	-	1229	dis	300	929
79	149	1.671	16	1.5	0.00034	0.05538	-	1520	77: 700	800	720
80	159	1.707	16	1.5	0.00112	0.05230	-	2737	ord	300	2437
81	159	1.707	16	1.5	0.00112	0.05230	-	2541	80:1500	1600	941
82	168	1.740	16	1.2	0.00126	0.04907	-	1394	ord	300	1002

Table A.4: Summary of input parameters and trajectory information for the ensembles with $m_\pi \approx 135$ MeV at $64^3 \times 8$ for 139 MeV $\leq T \leq$ 168 MeV. Details of each column are explained in the main text of this appendix.